

January 2013

# Modeling and Design of Photocatalytic reactors for Air Purification

Yangyang Zhang

*University of South Florida, yangyang@mail.usf.edu*

Follow this and additional works at: <http://scholarcommons.usf.edu/etd>

 Part of the [Art Practice Commons](#), [Chemical Engineering Commons](#), and the [Environmental Engineering Commons](#)

---

## Scholar Commons Citation

Zhang, Yangyang, "Modeling and Design of Photocatalytic reactors for Air Purification" (2013). *Graduate Theses and Dissertations*. <http://scholarcommons.usf.edu/etd/4621>

This Dissertation is brought to you for free and open access by the Graduate School at Scholar Commons. It has been accepted for inclusion in Graduate Theses and Dissertations by an authorized administrator of Scholar Commons. For more information, please contact [scholarcommons@usf.edu](mailto:scholarcommons@usf.edu).

Modeling and Design of Photocatalytic Reactors for Air Purification

by

Yangyang Zhang

A dissertation submitted in partial fulfillment  
of the requirements for the degree of  
Doctor of Philosophy  
Department of Chemical and Biomedical Engineering  
College of Engineering  
University of South Florida

Co-Major Professor: D. Yogi Goswami, Ph.D.  
Co-Major Professor: Elias K. Stefanakos, Ph.D.  
Norma Alcantar, Ph.D.  
Babu Joseph, Ph.D.  
Manoj K. Ram, Ph.D.  
Vicki Luna, Ph.D.

Date of Approval:  
March 15, 2013

Keywords: Photocatalysis, roughness, turbulence, mass transfer, contaminant, ZnO

Copyright © 2013, Yangyang Zhang

## **DEDICATION**

To my wife, Chunyan, and daughter, Yuxin; my father, Jianzhong Zhang, and mother, Rongmei He.

## **ACKNOWLEDGMENTS**

This dissertation would not be possible without the encouragement and support of many people.

First and foremost I want to thank my advisors, Drs. D. Yogi Goswami and Elias K. Stefanakos, for supporting and encouraging me to be a researcher and engineer. They always provided me with worthy guidance and constructive criticism. They shared their knowledge with me and helped me finish this task.

I am also very grateful to my committee members: Drs. Manoj K. Ram, Norma Alcantar, Babu Joseph, and Vicki Luna for their helpful comments and insightful questions. Sincerely thanks are due to Dr. Venkat R. Bhethanabotla, Chair of Chemical & Biomedical Engineering, who helped me in the first year of my study. I am also indebted to all my colleagues, who offered their assistance whenever I needed it.

## TABLE OF CONTENTS

LIST OF TABLES .....	iv
LIST OF FIGURES .....	v
ABSTRACT .....	ix
CHAPTER 1: INTRODUCTION .....	1
1.1 Indoor Air Quality.....	1
1.2 Current Technologies.....	4
1.3 Problem Statement .....	5
1.4 Research Objectives.....	6
CHAPTER 2: RESEARCH BACKGROUND .....	7
2.1 Introduction.....	7
2.2 Principle of Photocatalysis.....	8
2.3 Photocatalytic Oxidation.....	11
2.4 Photocatalysts .....	12
2.4.1 TiO <sub>2</sub> Photocatalyst .....	15
2.4.2 ZnO Nanowires Photocatalyst .....	18
2.4.2.1 The Vapor Phase Synthesis.....	21
2.4.2.2 Solution Phase Synthesis .....	23
2.4.2.2.1 Effect of the ZnO Seeding Layer .....	25
2.4.2.2.2 Effect of an Alkaline Reagent.....	27
2.4.2.2.3 Effect of Precursor Concentration .....	28
2.4.2.2.4 Effect of Growth Duration Time.....	30
2.4.2.2.5 Effect of Initial Solution pH .....	31
2.4.2.2.6 Effect of the Growth Substrate .....	32
2.4.2.2.7 Effect of Growth Temperature.....	32
2.4.2.2.8 Effect of Additives.....	32
2.4.2.2.9 Other Factors.....	33
2.4.2.3 Modification of ZnO Nanowires.....	33
2.5 Photocatalytic Reactors.....	34
2.6 Parameters that Influence a Photocatalytic Reactor.....	40
2.6.1 Kinetic Reactions .....	40
2.6.1.1 Light Source and Intensity .....	42
2.6.1.2 Contaminant Concentration .....	43
2.6.1.3 Humidity .....	43
2.6.1.4 Temperature .....	44

2.6.1.5 Other Factors.....	46
2.6.2 Mass Transfer.....	47
<b>CHAPTER 3: THEORETICAL ANALYSIS OF PHOTOCATALYTIC REACTORS WITH SURFACE ROUGHNESS .....</b>	<b>52</b>
3.1 Introduction.....	52
3.2 Two Dimensional Analysis of Turbulence Intensity with Roughness Patterns .....	54
3.2.1 Details of the Two Dimensional Photoreactor Passage Geometry.....	55
3.2.2 Roughness Element Geometry and Range of Parameters.....	55
3.2.3 Mesh.....	57
3.2.4 CFD Analysis.....	57
3.2.5 Numerical Modeling .....	58
3.3 Two Dimensional Analysis Results and Discussion.....	59
3.3.1 Flow Pattern and Square Shape of Roughness .....	59
3.3.2 Effect of Height of Roughness.....	61
3.3.3 Effect of Pitch Ratio ( $p/e$ ) and Shape of the Roughness Elements .....	64
3.3.4 Effect of Triangle Shape of Roughness .....	67
3.3.5 Effect of Square Shape of Roughness.....	67
3.3.6 Effect of Chamfered Shape of Roughness .....	69
3.4 Three Dimensional Analysis of Turbulence Intensity with Roughness Patterns .....	72
3.4.1 Details of the 3D Photoreactor Passage Geometry .....	73
3.4.2 Roughness Arrangements and Range of Parameters .....	73
3.4.3 Mesh.....	75
3.4.4 CFD Analysis.....	75
3.4.5 Numerical Modeling .....	76
3.5 Three Dimensional Analysis Results and Discussions .....	76
3.5.1 Effect of Transverse Broken Rib .....	77
3.5.2 Effect of Inclined Continuous Rib .....	81
3.5.3 Effect of Inclined Broken Rib.....	81
3.5.4 Effect of V Shape Continuous Rib.....	83
3.5.5 Effect of V Shape Broken Rib .....	84
3.5.6 Effect of Mesh Rib.....	84
3.5.7 Comparison of Different Roughness Elements.....	85
<b>CHAPTER 4: EXPERIMENTAL STUDY OF A PHOTOCATALYTIC REACTOR WITH SURFACE ROUGHNESS .....</b>	<b>90</b>
4.1 Introduction.....	90
4.2 Experimental.....	92
4.2.1 Experimental Set-up.....	92
4.2.2 Reactor Design and Fabrication.....	94
4.2.3 Rough Plate Fabrication.....	95
4.2.4 Catalyst Coating.....	97

4.3 Results and Discussion .....	99
4.3.1 The Effect of Catalyst Loading.....	99
4.3.2 The Effect of Reynolds Number .....	100
4.3.3 The Effect of the Increased Surface Area in the Rough Plates.....	103
4.3.4 The Effect of Various Roughness Patterns .....	105
4.3.5 Empirical Correlation.....	107
 CHAPTER 5: ZINC OXIDE NANOWIRE PHOTOCATALYSTS .....	110
5.1 Introduction.....	110
5.2 Experimental Procedure.....	111
5.2.1 ZnO Nanowire Growth .....	111
5.2.2 The Amount of Grown Nanowires .....	113
5.2.3 TiO <sub>2</sub> Coated on the Dish .....	113
5.2.4 Surface/structure Characterization.....	113
5.2.5 Photocatalysis Study .....	113
5.3 Results and Discussion .....	115
5.3.1 The Growth Amount of Nanowires .....	115
5.3.2 UV-vis Absorbance Spectrum .....	115
5.3.3 Structural Studies .....	117
5.3.4 Photocatalysis Studies.....	120
 CHAPTER 6: SUMMARY, CONCLUSIONS AND RECOMMENDATIONS .....	125
6.1 Theoretical Analysis .....	125
6.2 Experimental Study.....	127
6.3 Photocatalyst Development .....	128
 REFERENCES .....	130
 APPENDICES .....	154
Appendix A: List of Symbols .....	155
A.1 Nomenclature .....	155
A.2 Greek Symbols.....	156
Appendix B: Permissions.....	157
B.1 Permission for Article “Enhanced Photocatalytic Activity of Iron Doped Zinc Oxide Nanowires for Water Decontamination” © 2012 Elsevier.....	157
B.2 Permission for Article “Effect of Photocatalytic Surface Roughness on Reactors Effectiveness for Indoor Air Cleaning” © 2013 Elsevier .....	162
B.3 Permission for Article “Synthesis, Characterization, and Applications of ZnO Nanowires” © 2012 Hindawi Publishing Corporation.....	167
 ABOUT THE AUTHOR .....	End Page

## LIST OF TABLES

Table 2.1	Standard reduction potentials of some oxidants .....	11
Table 2.2	Organic compounds treated by photocatalysis in gas phase .....	13
Table 2.3	Pathogenic microorganisms photodegraded by photocatalysis .....	14
Table 2.4	Comparison of different ZnO nanostructures used in photocatalytic applications .....	20
Table 2.5	The diameter, density and length of ZnO nanorods corresponding to the thickness of the seed layer .....	27
Table 2.6	Average diameter of ZnO nanowires change with growth time .....	30
Table 2.7	The impact of total reaction rate with increasing of the temperature .....	45
Table 3.1	The different ranges of parameters of the studied roughness element.....	56
Table 3.2	Summary of the optimal parameters for different shapes of roughness elements .....	71
Table 3.3	The parameters of transverse broken rib roughness .....	77
Table 3.4	Summary of the optimum parameters for different roughness arrangements .....	88
Table 4.1	Specifications and parameters used in the investigation.....	92
Table 4.2	The details of the GC specification.....	93
Table 4.3	The detail parameters of various studied rough catalyst plates .....	97
Table 4.4	Comparison of the 1ppm toluene cleaning time between smooth and transverse No.1 catalyst plate .....	102
Table 5.1	The growth amount of nanowires on the 9 cm diameter petri dish .....	115



## LIST OF FIGURES

Figure 1.1	Sources of indoor air pollutants .....	2
Figure 2.1	A schematic of the principle of photocatalysis .....	9
Figure 2.2	Band edge positions of common semiconductor photocatalysts .....	15
Figure 2.3	Useful and non-useful part of solar spectrum for TiO <sub>2</sub> photocatalyst .....	17
Figure 2.4	ZnO structure: a) the wurtzite structure model; b) the wurtzite unit cell.....	19
Figure 2.5	Average diameters, lengths and aspect ratios of ZnO nanorods prepared from various precursor concentrations with a Zn(NO <sub>3</sub> ) <sub>2</sub> /C <sub>6</sub> H <sub>12</sub> N <sub>4</sub> ratio of 5 .....	29
Figure 2.6	Average diameters, lengths and aspect ratios of ZnO nanorods prepared in a 0.04 M precursor solution with various Zn(NO <sub>3</sub> ) <sub>2</sub> /C <sub>6</sub> H <sub>12</sub> N <sub>4</sub> ratios .....	29
Figure 2.7	Schematic diagrams of various photocatalytic reactors for air purification.....	35
Figure 2.8	Schematic of the photocatalytic indoor air treatment device.....	40
Figure 2.9	A laminar sublayer is formed when air flow on a smooth catalyst surface .....	47
Figure 2.10	A honeycomb photocatalytic reactor with non-uniform roughness elements on the catalyst surface.....	50
Figure 3.1	Sketch of roughness .....	53
Figure 3.2	Photoreactor channel with surface roughness elements on the bottom wall of the test section.....	55
Figure 3.3	Five different shapes of the roughness element studied in this work .....	57
Figure 3.4	Air flow over a smooth surface.....	60

Figure 3.5	Flow patterns of square roughness elements with different pitch ratios.....	60
Figure 3.6	Effect of square roughness pitch ratio ( $p/e$ ) on turbulence intensity for $Re$ from 2900 to 8700.....	61
Figure 3.7	Effect of height of roughness.....	62
Figure 3.8	Plot of the magnitude of the average turbulence intensity in the Y-axis direction with different height of roughness .....	63
Figure 3.9	Isosceles triangle and chamfer shape of roughness .....	64
Figure 3.10	Comparison of the effect of different shapes of roughness in the channel.....	65
Figure 3.11	Effect of base angle of isosceles triangle shape roughness.....	66
Figure 3.12	Effect of relative width ( $w/e$ ) on rectangle roughness .....	68
Figure 3.13	Effect of flow angle of attack of chamfer shape roughness.....	70
Figure 3.14	Photoreactor passage with transverse broken rib roughness elements on the bottom wall of the test section .....	73
Figure 3.15	The representative shape of rib roughness.....	74
Figure 3.16	Different surface roughness elements arrangements .....	74
Figure 3.17	Transverse broken rib roughnesses.....	77
Figure 3.18	Effect of transverse broken rib with the relative gap ( $g/e$ ) kept as 1 .....	78
Figure 3.19	Effect of transverse broken rib with the relative length of roughness ( $l/e$ ) kept as 10.....	78
Figure 3.20	Studies of inclined continuous rib roughness sheet.....	80
Figure 3.21	Effect of inclined continuous rib roughness .....	80
Figure 3.22	Studied of inclined broken rib roughness sheet.....	82
Figure 3.23	Effect of inclined broken rib .....	82
Figure 3.24	Effect of V shape continuous rib .....	83
Figure 3.25	V shape broken rib roughness sheet.....	85

Figure 3.26	Effect of flow angle of attack on turbulence intensity for V shape broken ribs .....	85
Figure 3.27	Mesh rib roughness sheet.....	86
Figure 3.28	Effect of flow angle of attack on the turbulence intensity for a mesh rib plate .....	86
Figure 3.29	Comparison of the effect of flow angle of attack on the turbulence intensity for inclined, V shape and mesh of rib roughness .....	87
Figure 4.1	Flow pattern of the air flow over a rough surface.....	91
Figure 4.2	Schematic of the experimental set-up .....	93
Figure 4.3	The sketch of the photocatalytic reactor .....	94
Figure 4.4	The fabricated photocatalytic reactor.....	95
Figure 4.5	Sketch of the roughness elements .....	96
Figure 4.6	Various rough plates .....	97
Figure 4.7	TiO <sub>2</sub> photocatalyst was sprayed on the transverse No.1 rough plate.....	98
Figure 4.8	Effect of catalyst loading on a smooth plate on the photocatalytic oxidation 1ppm toluene at Reynolds number of 2900 .....	99
Figure 4.9	Comparison of results for different Reynolds numbers for a smooth catalyst plate and 1ppm toluene degradation in the chamber .....	101
Figure 4.10	Comparison of transverse No.1 rough catalyst plates with different Reynolds numbers for 1ppm toluene degradation .....	102
Figure 4.11	Comparison of cleaning times of 1ppm toluene in the chamber for the reactors with a smooth catalyst plate and a transverse rough catalyst plate.....	103
Figure 4.12	Schematic of TiO <sub>2</sub> coated on various plates .....	104
Figure 4.13	Comparison of toluene photocatalytic oxidation of the reactor with the transverse No.1, transverse No.3 and smooth catalyst plates at Reynolds number 2900 .....	104

Figure 4.14	Comparison of the photocatalytic reactor performance results for the reactor with smooth and various rough catalyst surfaces for cleaning the contaminated air in the chamber .....	106
Figure 4.15	Comparison of toluene photocatalytic oxidation results for the reactor with various rough catalyst plates at a Reynolds number of 2900 in terms of $-\ln(C/C_0)$ .....	107
Figure 4.16	Plot of the overall reaction rate constant (k) versus turbulence intensity for the Reynolds numbers of 2900, 4300, and 5800 .....	108
Figure 4.17	Comparison of experimental values and empirical correlation at Reynolds numbers from 2900 to 5800.....	109
Figure 5.1	A flow schematic of the ZnO nanowire growth procedure.....	112
Figure 5.2	Experimental setup of the photocatalytic study.....	114
Figure 5.3	UV-vis.....	116
Figure 5.4	SEM images .....	118
Figure 5.5	XRD spectrum .....	119
Figure 5.6	Raman spectrum.....	119
Figure 5.7	Photodegradation of DCB.....	122
Figure 5.8	Photodegradation of MO.....	123

## ABSTRACT

Photocatalysis is a promising technique for the remediation of indoor air pollution. Photocatalysis utilizes semiconductor photocatalysts (such as  $\text{TiO}_2$  or  $\text{ZnO}$ ) and appropriate light to produce strong oxidizing agents ( $\text{OH}\cdot$ ) that are able to break down organic compounds and inactivate bacteria and viruses. The overall goal of the research is to develop an efficient photocatalytic reactor based on mass transfer for indoor air purification. This study has focused on the enhancement of the effectiveness of the photocatalytic process by the introduction of artificial roughness on the reactor catalyst surface. The major effect of artificial roughness elements on the catalytic surface is to create local wall turbulence and enhance the convective mass transfer of the contaminants to the catalyst surface and thus lead to an increase in the effectiveness of photocatalysis.

Air flow properties in a model photoreactor channel with various roughness patterns on the interior wall surface were theoretically investigated. The optimum shapes, sizes, and arrangements of roughness were determined for the maximum enhancement of turbulence intensity in the channel. The possible order of photocatalytic reactor performance for various roughness patterns was also determined. In order to verify the theoretical analysis results, experimental studies were carried out. A plate type photocatalytic reactor was designed and fabricated on the basis of the theoretical results. It was determined that the photocatalytic reactor performance is greatly improved with various rough catalyst surfaces. The experimental results verified the theoretical results.

The relationship between the overall reaction rate constant ( $k$ ) of the reactor and the magnitude of the turbulence intensity was found out. An empirical correlation expression was also proposed. This is the first study of the effect mass transfer in a rough catalytic surface for photocatalytic reactor.

Photocatalyst development has also been studied. Zinc oxide (ZnO) and iron doped zinc oxide (ZnO/Fe) nanowires were synthesized on glass substrates through a conventional hydrothermal method. The photocatalytic activities under ultraviolet (UV) light and white light irradiation were separately investigated. The ZnO/Fe nanowires exhibited an enhanced photocatalytic activity as compared to ZnO nanowires regardless of the type of contaminants and light sources.

## **CHAPTER 1: INTRODUCTION**

### **1.1 Indoor Air Quality**

In recent years, indoor air quality (IAQ) has become of greater concern due to the increased amount of time people spend in indoor environments. It has been reported that most people spend more than 90% of their time in indoor environments such as a home, office, car or shopping center [1-3]. The level of contaminants in an indoor environment is typically much higher than that of an outdoor environment [1, 2]. More and more products containing volatile organic compounds (VOCs) like synthetic building materials, furnishings and consumer products are being used. Further, buildings have been sealed more tightly in the past decades to reduce the energy consumption associated with indoor air conditioning [4, 5]. Although such development was successful in certain respects (e.g., reducing costs), it also created other problems such as poorer air quality [5].

Air quality is often considered the major cause of environmental health issues. Poor indoor air quality represents a potential risk for the development of respiratory symptoms, infections, and allergies, especially in children [6-8]. Millions of people die and billions of dollars are lost in the world every year due to poor indoor air quality [9, 10]. Indoor air pollution has been classified as one of the most serious threats to human health [11]. The effects on human health by air pollution may show up almost immediately after exposure. The symptoms of these immediate effects may include difficulty in breathing, wheezing, coughing and aggravation of existing respiratory and

cardiac conditions. Other health effects may show up years after exposure or after long periods of exposure. The long term effects by air pollution, which include respiratory infections, heart disease and lung cancer, can be severely debilitating or fatal.

The effect of indoor air quality includes gas contaminants, microbial contaminants, and particulate matters.

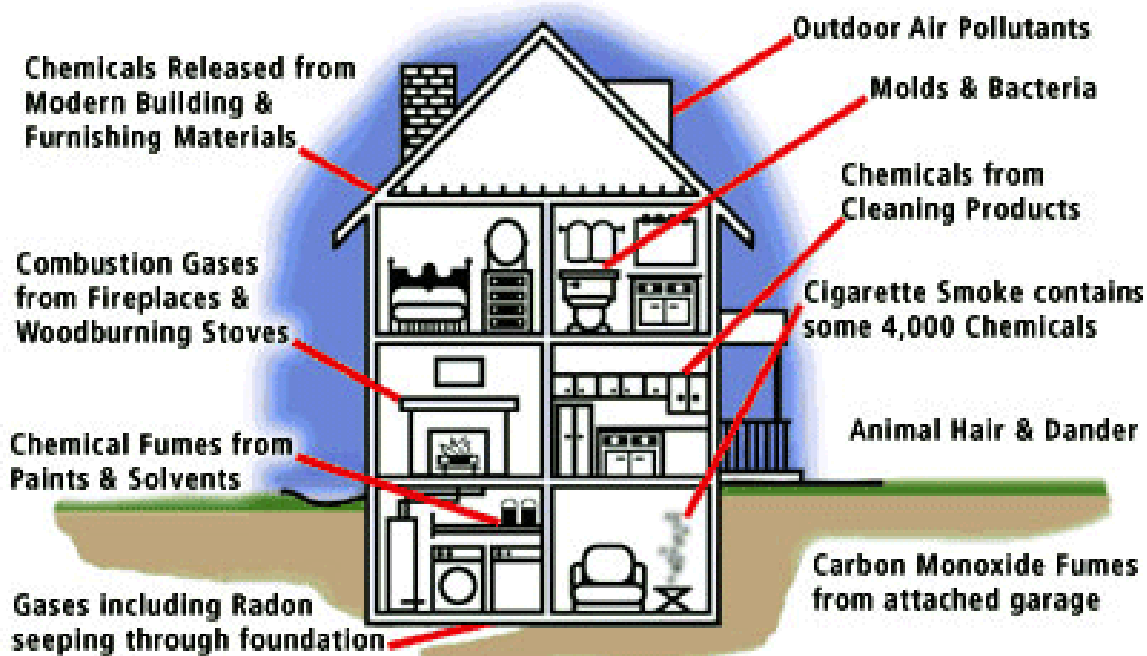


Figure 1.1 Sources of indoor air pollutants [12]

The gas contaminants mainly include volatile organic compounds (VOCs), carbon oxides (CO and CO<sub>2</sub>), nitrogen dioxide (NO<sub>2</sub>), Ozone (O<sub>3</sub>), radon (Rn), etc. As the most important part of gas contaminants VOCs, which are emitted from certain solids or liquids, include a variety of chemicals such as formaldehyde, toluene, benzene, xylene and many others. VOCs are emitted by a large number of products such as paints, cleaning supplies, pesticides, building materials, furnishings, and office equipment. Many VOCs are known to be toxic and considered to be carcinogenic, mutagenic, or teratogenic



[13]. Carbon oxides and nitrogen dioxide are mainly emitted by human metabolic activity and burning. Higher levels of carbon oxide or nitrogen dioxide indoors may cause drowsiness, headaches, or functioning at lower activity levels. The main sources of indoor O<sub>3</sub> are from outdoor O<sub>3</sub> as well as air purifiers such as ozone generators, which are used to reduce odors and destroy microbes. However, O<sub>3</sub> can damage the lungs, causing chest pain and worse chronic respiratory diseases such as asthma. Radon is an inert radioactive gas produced by the radioactive decay of radium which is found in a number of common minerals. Many houses and buildings have been constructed with radon emitting rock. The radioactive particles from Radon decay can get trapped in human lungs by breathing. As they further decay, the process releases small bursts of energy which can damage lung tissue and lead to lung cancer [14].

Microbial contaminants include molds, bacteria, and viruses. Most of the microbial contamination problems are associated with moisture because they usually grow in moist environments. They are usually transported as attached to other particles, such as skin flakes, soil and dust. Microbial contaminants indoors can cause adverse health effects by many different biological mechanisms, including infectious diseases, allergies, irritant reactions and inflammatory reactions [15].

Sources of particulate matter include tobacco smoke, cooking, consumer products, building materials and house dust. Particulate matter could deposit in the respiratory system and increase respiratory symptoms [3]. Further, organic pollutants and microbial contaminants can also be adsorbed on the surface of particulate matter and cause adverse human health effects.

## 1.2 Current Technologies

The current technologies available to clean indoor air include ultraviolet germicidal irradiation (UVGI) [16], high efficiency particulate air (HEPA) filtration [17], carbon adsorption [18], chemical oxidation by ozone [19], ionizer purifier [20], and photocatalytic oxidation [21]. However, most of these technologies are not completely effective in degrading both biological contaminants and VOCs.

Ultraviolet germicidal irradiation (UVGI) with UVC lamps can be used for disinfection. However, high intensity short wavelength UVC is just as dangerous to humans as it is to microorganisms. Dangerous gas ozone is also formed during the process. Moreover, UVGI is not very effective in the degradation of organic contaminants.

High efficiency particulate air (HEPA) filters physically remove most of the particles with a diameter larger than 0.3 micrometers, but these filters cannot remove smaller sized particles like VOC molecules and viruses. Another drawback of HEPA filters is that they operate with relatively high pressure drops, meaning higher energy consumption.

Activated carbon adsorption is another physical method to remove air contaminants. But these just transfer the air contaminants to carbon and do not destroy the contaminants. They have a limited long term operation and the saturated absorbent therefore must be periodically exchanged or regenerated. Moreover, the efficiency of activated carbon adsorption is significantly decreased at higher temperature and the adsorption of the second species into the carbon bed may lead to the reemittance of the first species.

The chemical oxidation technique, by using ozone, could be applied for disinfection or removal of odors. However, this technique is only for unoccupied rooms because it is not safe for humans to breathe ozone gas.

Ionizer purifiers can remove particulate matters but produce ozone and other oxidants as by-products which can lead to serious health issues.

Photocatalytic oxidation (PCO) is an emerging technology in air purification. Recent researches show that photocatalysis is a promising technology for environmental protection [22, 23]. It is able to completely oxidize low concentrations of organic contaminants, which include VOCs and microorganisms, into benign products but not limited by ambient temperatures and pressures [24-30]. It may be integrated into new and existing heating, ventilation, and air conditioning systems (HVAC). It is also able to utilize sunlight directly and play a significant role in reducing building energy consumption [31].

### **1.3 Problem Statement**

Due to the many advantages of this technology, the development of efficient photocatalytic oxidation (PCO) reactors is becoming more and more important. Air contaminant removal by photocatalyst is a surface reaction process consisting of two important steps: first, the air contaminants have to transfer to the reaction surface; and second, the air contaminants are decomposed by the photocatalyst. Thus, mass transfer and kinetic reaction rates are two of the most important performance parameters of a photocatalytic reactor [32]. Kinetic reaction studies of photocatalytic reactions at various operational conditions have been successfully conducted by many research groups [33-

35]. However, mass transfer still has not received great attention in the photocatalytic field. Very few research groups have studied how to increase the mass transfer in a photocatalytic reactor. The conventional method for increasing the mass transfer on the catalyst surface is by increasing the air flow rate in the reactor [36]. But in practice, increasing the flow rate would lead to a reduction in the air purification performance of a reactor due to a reduction in the residence time. Therefore, a study of the probability of contact between the contaminants and the catalyst is of great significance for determining the optimum performance of photocatalytic reactors.

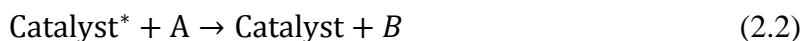
#### **1.4 Research Objectives**

The objectives of the research are: (1) to increase the performance of photocatalytic reactors for indoor air application by increasing the probability of contact between the contaminants and the catalyst; (2) to develop new photocatalyst for increasing the photoactivity of the photocatalyst especially under visible light conditions. The overall goal is to develop an efficient photocatalytic reactor for indoor air application.

## CHAPTER 2: RESEARCH BACKGROUND<sup>1</sup>

### 2.1 Introduction

Most people have observed colors fading over long exposure to sunlight, or some materials deteriorating in the sunlight. Thus, it is not hard to understand that light causing reactions could be used to break down toxic chemicals. For the last several decades, research has not only confirmed the capability of certain energy light to detoxify and disinfect, but also accelerate this process by the use of catalysts. When light is used to cause a chemical reaction by direct absorption, the process is called photolysis. If the objective is achieved by the use of catalysts, it is known as photocatalysis [37]. According to IUPAC, the definition of photocatalysis is “Change in the rate of a chemical reaction or its initiation under the action of ultraviolet, visible, or infrared radiation in the presence of a substance—the *photocatalyst*—that absorbs light and is involved in the chemical transformation of the reaction partners” [38].



---

<sup>1</sup> Portions of these results have been previously published (Yangyang Zhang, Manoj K. Ram, Elias K. Stefanakos, and D. Yogi Goswami. Synthesis, characterization, and applications of ZnO nanowires. 2012, 2012 and Yangyang Zhang, Elias K. Stefanakos, D. Yogi Goswami. Effect of photocatalytic surface roughness on reactors effectiveness for indoor air cleaning. Building and Environment, 61, 188-196, 2013) or under review (Yangyang Zhang, Elias K. Stefanakos, D. Yogi Goswami. Optimum photocatalytic reactor performance with surface roughness arrangement for indoor air cleaning. Building and Environment, 2013) and are utilized with permission of the publisher.

Photocatalysis was first applied to waste water treatment [39-41]. However, much research on photocatalysis has been conducted in a variety of novel applications. These include self-cleaning surface, antifogging, antireflective, hydrophobic, conversion of water to hydrogen gas, conversion of carbon dioxide into hydrocarbons and air purification [42-45]. Recent researches show that photocatalysis is a promising technology for air purification [22, 26]. This technology can play a significant role in reducing building energy consumption and in reducing indoor air contaminant level [31]. Moreover, it is able to completely oxidize low concentrations of organic contaminants which include VOCs and microorganisms into benign products [21, 23-25, 27-30, 46-50]. Compared to photocatalytic reactions in aqueous solutions, gas phase processes have more advantages such as relatively low levels of UV light, negligible amount of photons adsorbed by air, and sufficient electron scavengers ( $O_2$ ). Thus, the use of photocatalysis for air purification has received lot of interest.

## 2.2 Principle of Photocatalysis

For air purification, photocatalysis utilizes semiconductor photocatalysts such as  $TiO_2$  or  $ZnO$  to carry out a photo-induced oxidation process to break down organic contaminants and inactivate bacteria and viruses [22, 51, 52]. The overall photocatalytic reaction could be [53]:



The band gap energy of semiconductor photocatalysts plays a significant role in the photocatalytic process. The band gap energy is the energy difference between the

conduction band and the valence band in semiconductors. Figure 2.1 illustrates the process of photocatalysis.

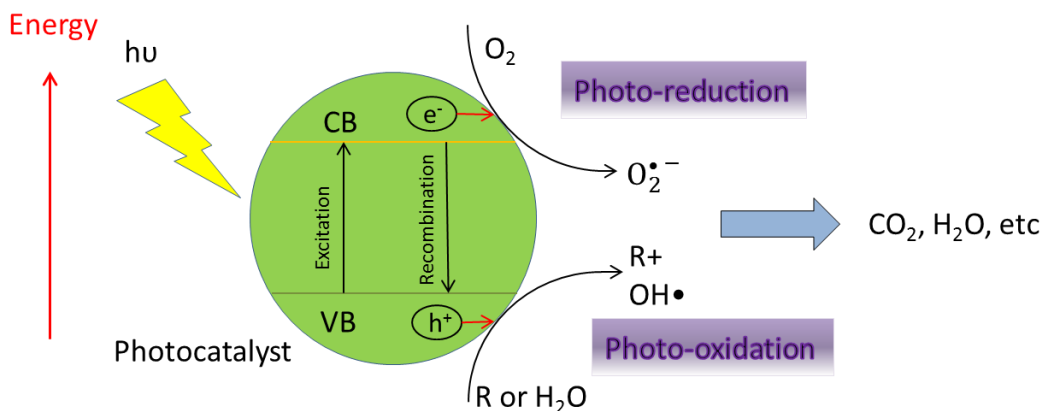
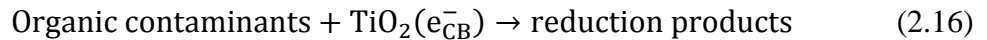
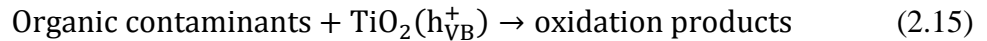
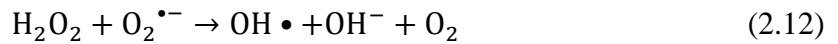
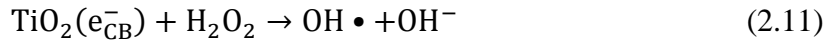
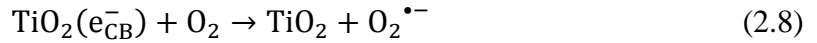
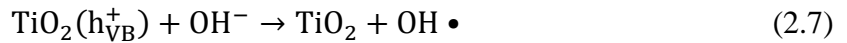
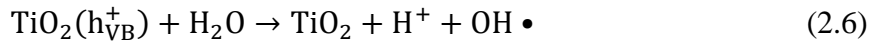
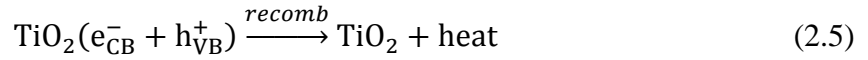
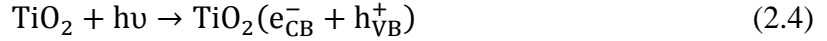


Figure 2.1 A schematic of the principle of photocatalysis

When photons with energies greater than the band-gap energy of the photocatalyst are absorbed (3.2eV for TiO<sub>2</sub>), the valence band (VB) electrons are excited to the conduction band (CB) to facilitate a number of possible photo-reactions. The photocatalytic surface with sufficient photo energy leads to the formation of a positive hole (h<sup>+</sup>) in the valence band and an electron (e<sup>-</sup>) in the conduction band (CB). The positive hole could oxidize either organic contaminants directly or produce very reactive hydroxyl radicals (OH•). The hydroxyl radicals (OH•) act as the primary oxidants in the photocatalytic system [54], which are able to oxidize the organics. The electron in the conduction band (CB) may recombine with holes in the valence band (VB) and produce heat or reduce the oxygen that is adsorbed on the photocatalyst and produce superoxide radicals (O<sub>2</sub><sup>•-</sup>). The superoxide radical (O<sub>2</sub><sup>•-</sup>) can be further protonated to form the hydroperoxyl radical (HO<sub>2</sub>•) and contribute to the oxidation of organics.

The organic contaminants are first degraded to their corresponding intermediates and further mineralized to CO<sub>2</sub> and H<sub>2</sub>O. The primary reactions in a photocatalytic oxidation by TiO<sub>2</sub> are summarized below [53, 55]:



Although the above photocatalytic reactions have been explained on the basis of TiO<sub>2</sub>, other semiconductor photocatalytic reactions follow similar mechanisms. Because photocatalysis is a surface reaction process, it could be divided into five independent steps [53, 55, 56]:

1. Mass transfer of organic contaminants to the catalyst surface.
2. Adsorption of the organic contaminants on photon activated catalyst surface.
3. Photocatalysis reaction.



4. Desorption of the degradation products from the catalyst surface.
5. Mass transfer of the degradation products from the interface region to the bulk fluid.

The overall reaction rate of photocatalysis is equal to the slowest step. Thus, each step has same importance in the photocatalytic process.

Table 2.1 Standard reduction potentials of some oxidants [57]

<b>Oxidant</b>	<b>Standard reduction potential (V vs. NHE)</b>
Fluorine (F <sub>2</sub> )	3.03
Hydroxyl radical (HO•)	2.80
Atomic oxygen	2.42
Ozone (O <sub>3</sub> )	2.07
Hydrogen peroxide (H <sub>2</sub> O <sub>2</sub> )	1.77
Potassium permanganate (KMnO <sub>4</sub> )	1.67
Hypobromous acid (HBrO)	1.59
Chlorine dioxide (ClO <sub>2</sub> )	1.50
Hypochlorous acid (HClO)	1.49
Chlorine (Cl <sub>2</sub> )	1.36
Bromine (Br <sub>2</sub> )	1.09

### 2.3 Photocatalytic Oxidation

Because the primary oxidant hydroxyl radical (OH•) has a very high oxidation potential, photocatalytic oxidation is a non-selective oxidation. It could decompose a

large variety of organic contaminants and microorganisms to  $\text{CO}_2$ ,  $\text{H}_2\text{O}$ , and harmless inorganic byproducts. The oxidizing potential of the hydroxyl radical ( $\text{OH}\cdot$ ) is only being exceeded by fluorine (Table 2.1).

There are a number of organic contaminants and pathogenic microorganisms that have been treated by photocatalysis. A brief list is given in Table 2.2 for organic compound degradation by photocatalysis.

Most of the  $\text{TiO}_2$  photocatalytic disinfection studies focus on bacteria, but cancer cells, yeasts, viruses, and other types of cells have also been studied. A brief list is given in Table 2.3 for pathogenic microorganism disinfection by photocatalytic oxidation.

## **2.4 Photocatalysts**

For a semiconductor to be a photocatalyst, the valence band hole must be positive enough to generate  $\text{OH}\cdot$  radicals, which can further oxidize the organic contaminants. The redox potential of the conduction band electron must be negative enough to be able to reduce adsorbed  $\text{O}_2$  [59]. The band gap energy of the semiconductor photocatalyst is also very important in the photocatalytic process because only photons with energies greater than the band gap energy of the photocatalyst could excite the electrons from the valence band (VB) to the conduction band (CB) and facilitate a number of possible photo-reactions. Common photocatalysts are primarily metal oxides ( $\text{TiO}_2$ ,  $\text{ZnO}$ ,  $\text{WO}_3$ ,  $\text{Fe}_2\text{O}_3$  etc.) and metal sulphides ( $\text{ZnS}$ ,  $\text{CdS}$ , etc.). Figure 2.2 shows the band gap energies and the band edge positions of vary common semiconductor photocatalysts [60-63]. The energy level at the conduction band is the reduction potential of photoelectrons ( $e^-$ ) and the energy level at the valence band determines the oxidizations ability of holes ( $h^+$ ).

Table 2.2 Organic compounds treated by photocatalysis in gas phase [58]

<b>Class</b>	<b>Compounds</b>
Hydrocarbons	Methane, Ethane, Propane, <i>n</i> -Butane, Hexane, Heptane, Cyclohexane, Ethylene, Propene, Methylacetylene, Cyclohexene, Benzene, Toluene,
Halogenated	DCH (dichloromethane), Trichloromethane, TCE, PCE, Vinyl chloride, TCE+PCE, 1,3-dichlorobenzene
Nitrogen-containing	Diethylamine, Propylamine, Pyridine
Hydroxylated	Methanol, Ethanol, 2-Propanol, Butanol, <i>tert</i> -Butyl-alcohol
Ether	Diethylether, Methyl-butyl-ether
Sulfur-containing	Diethyl sulfide, 2-Chloroethyl ethyl sulfide
Silicon-containing	1,3,5,7-Tetramethylcyclotetrasiloxane, Octamethyltrisiloxane
Aldehydes, ketones	Formaldehyde, Acetaldehyde, Propionaldehyde, Acetone, Methyl-ethyl ketone, Methyl-isobutyl ketone
Inorganic	NO <sub>x</sub> , O <sub>3</sub>
Organic–inorganic	NO+BTEX, NO+BTEX+SO <sub>2</sub>

Table 2.3 Pathogenic microorganisms photodegraded by photocatalysis [58]

<b>Class</b>	<b>Pathogenic organisms</b>
Gram-negative bacteria	Escherichia coli, Enterobacter cloacae, Salmonella typhimurium, Salmonella choleraesuis, Serratia marcescens, Hyphomonas polymorpha, Vibrio parahaemolyticus, Pseudomonas aeruginosa, Klebsiella pneumonia
Gram-positive bacteria	Streptococcus sobrinus Streptococcus mutans, AHT, Bacillus subtilis, Lactobacillus helveticus, Enterococcus faecalis, Micrococcus luteus, Listeria monocytogenes
Enzyme	Horseradish peroxidase
Protozoan	Giardia lamblia
Fungus	Aspergillus niger
Algae	Chlorella vulgaris
Viruses	Lactobacillus casei phage PL-1, Bacterioides fragilis bacteriophage, Phage MS 2, Poliovirus 1
Cancer cells	HeLa, T 24, U 937

Ideally, a semiconductor photocatalyst should be chemically and biologically inert, photo catalytically stable, easy to produce and to use, efficiently activated by sunlight, able to efficiently catalyze reactions, cheap, and without risks for the environment or humans [58].

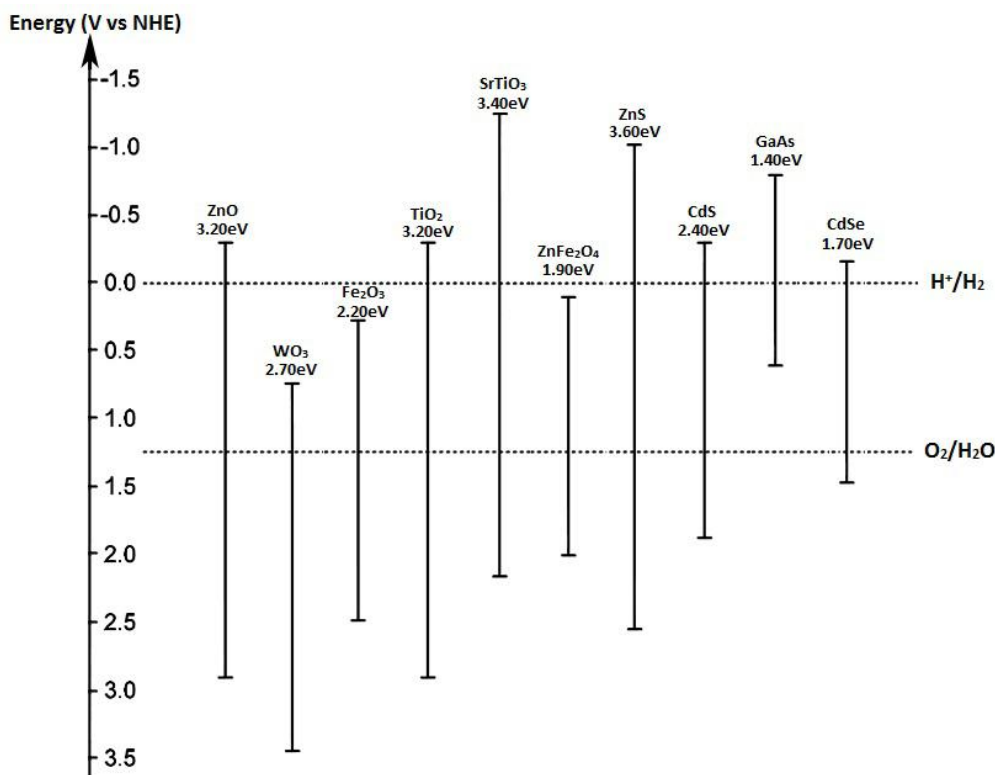


Figure 2.2 Band edge positions of common semiconductor photocatalysts (data from [61-63])

#### 2.4.1 TiO<sub>2</sub> Photocatalyst

Among a variety of common photocatalysts, TiO<sub>2</sub> is the most popular in the last several decades due to it is relatively inexpensive, harmless, chemically stable material, and highly activity [64, 65]. TiO<sub>2</sub> has three main crystal forms: anatase, rutile, and brookite. Anatase and rutile are the two crystalline forms which show photocatalytic activity. The direct band gap energies of anatase and rutile are 3.2 and 3.0eV,

respectively. For photocatalytic applications, anatase has been considered to be more active than rutile because the conduction band location for anatase is more favorable for driving conjugate reactions involving electrons. Very stable surface peroxide groups can be formed at the anatase during a photo-oxidation reaction but not on the rutile surface [66, 67]. Other researchers suggest that this increased photoactivity is because anatase has a slightly higher Fermi level, lower capacity to adsorb oxygen, and higher degree of hydroxylation [68-70].

Some authors have reported that a synergistic effect of anatase and rutile mixed phases could enhance the photocatalytic activity [71-73]. In mixed-phase  $\text{TiO}_2$ , charges produced on rutile are stabilized through electron transfer to the lower energy anatase lattice trapping sites and the transition points between these two phases allow for rapid electron transfer from rutile to anatase [73]. Although there are many different sources of  $\text{TiO}_2$ , Degussa P25  $\text{TiO}_2$  has been widely used because it has substantially higher photocatalytic activity than most other commercial  $\text{TiO}_2$  [74]. Degussa P25 contains 75% anatase and 25% rutile with average individual particle size of 20~30 nm and surface area of  $50 \text{ m}^2\text{g}^{-1}$  [75]. It is synthesized by the hydrogen flame process in aerosol [76]. Degussa P25 has been used by some researchers as a standard reference for comparison with their modified/synthesis  $\text{TiO}_2$  [77].

Because  $\text{TiO}_2$  has band gap energy of 3.2eV and the corresponding wavelength of a photon with energy equal to the band gap of  $\text{TiO}_2$  is 388nm, only a photon of light with a wavelength of 388nm or less will excite an electron from the valence band (VB) to the conduction band (CB). Thus, the application of the  $\text{TiO}_2$  photocatalyst has been primarily

limited to ultraviolet (UV) environments which correspond to approximately 4% of the solar radiation (Figure 2.3).

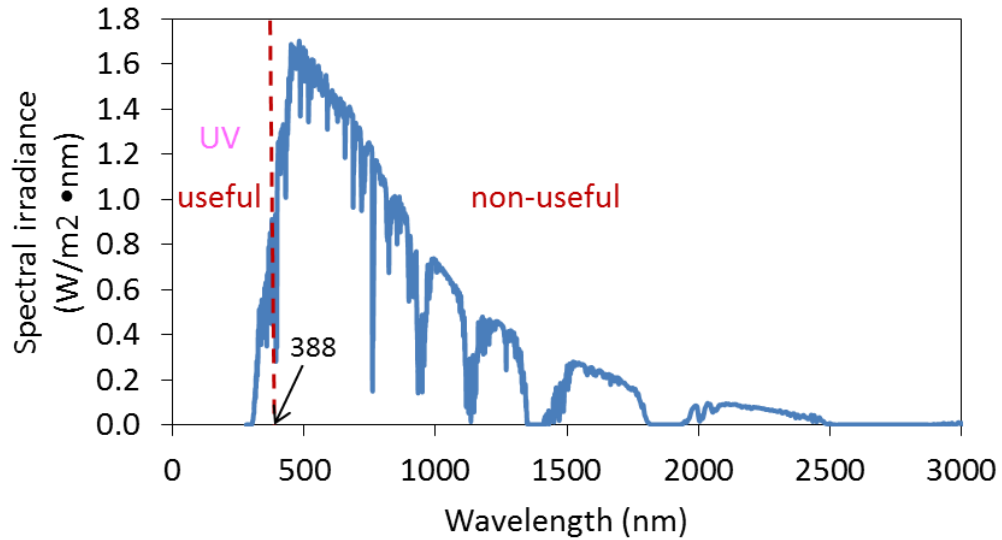


Figure 2.3 Useful and non-useful part of solar spectrum for TiO<sub>2</sub> photocatalyst

In order to extend the photo response into the visible spectrum and improve the photocatalytic activity of TiO<sub>2</sub>, lots of attempts have been carried out by many research groups. Surface modification, ion doping, and coupled photocatalysts are the three main methods to improve the photocatalytic performance. It has been reported that a noble metal (such as Ag, Pt, Ni, Cu, and Pd) with a Fermi level lower than the TiO<sub>2</sub> catalyst, which is deposited on the TiO<sub>2</sub> surface, is a very effective for the enhancement of the photocatalytic performance [78-80]. The photo excited electrons can be transferred from the conduction band (CB) to metal particles deposited on the surface of TiO<sub>2</sub> thus reducing the possibility of the electron/hole recombination. However, too much metal particle deposition might reduce photon absorption by TiO<sub>2</sub> and become electron/hole recombination centers which reduce the photocatalytic performance. Therefore, optimal metal loading should be considered. Doping metal ions or anions into the TiO<sub>2</sub> lattice is

another way to improve the photocatalytic performance by reducing the TiO<sub>2</sub> band gap and extending the light absorption into the visible region [46, 81-84]. However, the doped ions may act as recombination centers if the charge transfer rate is low. Thus, ions should be doped near the surface of TiO<sub>2</sub> for a better charge transfer. Some research groups also have reported that the red-shift of the absorption edge is due to the formation of color centers and the band gap narrowing is not based on semiconductor physics [85]. The coupling of different photocatalysts to increase the photocatalytic performance has also been reported [86]. When a semiconductor photocatalyst with a large band gap is coupled to a semiconductor photocatalyst with a smaller band gap, conduction band electrons can be injected from the small band gap to the larger band gap semiconductor photocatalyst. Thus, a further electron/hole separation is obtained to increase the life time of the electron/hole pair.

#### 2.4.2 ZnO Nanowires Photocatalyst

ZnO is a semiconductor material with a direct wide band gap energy (3.37 eV) and a large exciton binding energy (60 meV) at room temperature [87]. ZnO is also biocompatible, biodegradable and biosafe for medical and environmental applications [88]. ZnO crystallizes include two main forms, hexagonal wurtzite and cubic zinc blende. Under general conditions, ZnO exhibits a hexagonal wurtzite structure.

The structure of ZnO could be described as a number of alternating planes composed of tetrahedrally coordinated O<sup>2-</sup> and Zn<sup>2+</sup> stacked alternately along the c-axis (Figure 2.4a). The O<sup>2-</sup> and Zn<sup>2+</sup> form a tetrahedral unit and the entire structure lacks central symmetry (Figure 2.4b). Due to their remarkable performance in electronics, optics and photonics, ZnO nanowires are attractive candidates for many applications such



as UV lasers [89], light emitting diodes [90], solar cells [91], nanogenerators [92], gas sensors [93], photodetectors [94] and photocatalysts [95].

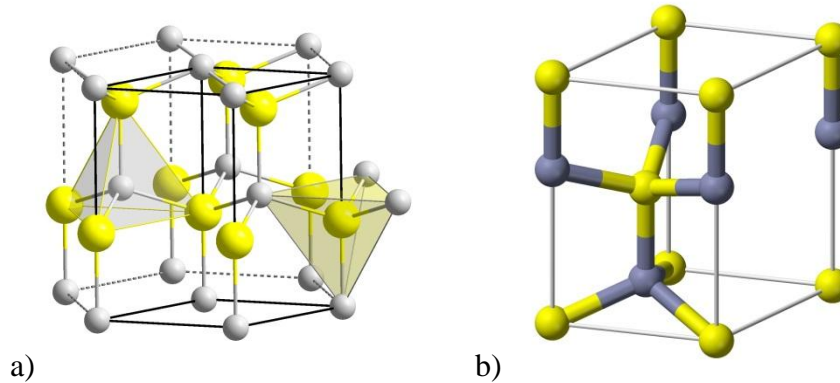


Figure 2.4 ZnO structure: a) the wurtzite structure model; b) the wurtzite unit cell (from Wikipedia.org)

Although  $\text{TiO}_2$  is the most widely investigated photocatalyst, ZnO has also been considered as a suitable alternative to  $\text{TiO}_2$  because of its comparable with  $\text{TiO}_2$  band gap energy and its relatively lower cost of production [96-98]. Recently, ZnO has been reported to be more photoactive than  $\text{TiO}_2$  [99-102] due to its higher efficiency of generation and separation of photoinduced electrons and holes [96, 103, 104]. Due to the number of contaminant molecules that need to be adsorbed on the photocatalytic surface for a degradation process, the surface area of the catalyst plays a significant role in the photocatalytic activity. Although nanoparticles offer a large surface area, they have mostly been used in water suspensions, which limit their practical use due to difficulties in their separation and recovery. Photocatalysts supported on a steady substrate can eliminate this problem. One dimensional nanostructures, such as nanowires grown on a substrate offer enhanced photocatalytic efficiency due to their extremely large surface to volume ratio as compared to a catalyst deposited on a flat surface [51, 105].

Table 2.4 Comparison of different ZnO nanostructures used in photocatalytic applications

<b>Nanoparticles</b>		<b>Nanowires</b>		<b>Nano thin film</b>	
<b>Advantages</b>	<b>Disadvantages</b>	<b>Advantages</b>	<b>Disadvantages</b>	<b>Advantages</b>	<b>Disadvantages</b>
<p>Could be suspended in a solution</p> <p>High performance because of larger surface areas</p>	<p>Particle aggregation in a solution lead to a reduced surface area</p> <p>Post treatment for catalyst removal is required</p> <p>Difficult to recover all the catalyst</p>	<p>Growth could be well-aligned on most substrates</p> <p>Offer larger surface area compare to nano thin film</p> <p>Post treatment for catalyst removal is not required</p> <p>Lower crystallinity and more defects</p>	<p>Growth conditions are more restricted</p> <p>Lower surface area compare to nanoparticles</p>	<p>Coated on certain substrates</p> <p>Post treatment for catalyst removal is not required</p>	<p>Lower performance because of small surface area</p>

Table 2.4 compares different ZnO nanostructures for photocatalytic applications. There are many advantages in nanowire structures which could be used as photocatalysts. ZnO nanowires can be either grown independently or grown on certain substrates. However, a vertically aligned growth on a substrate has more advantages in photocatalytic applications. The synthesis methods of ZnO nanowires could mainly be classified as vapor phase and solution phase synthesis.

#### 2.4.2.1 The Vapor Phase Synthesis

Vapor phase synthesis is probably the most extensively explored approach in the formation of 1D nanostructures [106]. A typical vapor phase synthesis method takes place in a closed chamber with a gaseous environment. Vapor species are first produced by evaporation, chemical reduction and gaseous reaction. After that, the species are transferred and condensed onto the surface of a solid substrate. Generally, the vapor phase synthesis process is carried out at higher temperatures from 500 °C to 1500 °C and produces high-quality nanowires. The typical vapor phase synthesis method includes vapor liquid solid (VLS) growth [107], chemical vapor deposition (CVD) [108], metal organic chemical vapor deposition (MOCVD) [109], physical vapor deposition (PVD) [110], molecular beam epitaxy (MBE) [111], pulsed laser deposition (PLD) [112] and metal organic vapor phase epitaxy (MOVPE) [113]. Among the vapor phase synthesis methods, VLS, MOCVD, and PVD are the three most common methods for the ZnO nanowires synthesis.

Compared to other vapor phase techniques, the VLS method is a simpler and cheaper process, and is advantageous for growing ZnO on large wafers [114]. The VLS process has been widely used for the growth of 1D nanowires and nanorods. A typical

VLS process is used with nanosized liquid metal droplets as catalysts. The gaseous reactants interact with the nanosized liquid facilitating nucleation and growth of single crystalline rods and wires under the metal catalyst. Typical metal catalysts in the VLS process are Au, Cu, Ni, Sn, etc. ZnO nanowires have been successfully grown on sapphire, GaN, AlGaN and ALN substrates through the VLS process [115]. The quality and growth behavior of the ZnO nanowires are strongly affected by the chamber pressure, oxygen partial pressure and thickness of the catalyst layer [116, 117]. Chu et al. [118] synthesized well-aligned ZnO nanowires using the VLS method on Si substrate at chamber temperatures varying from 600 to 950 °C and pressures from 0.75 to 3 torr. They showed that ZnO nanowires with high aspect ratio grew vertically on the substrate at 700 to 750 °C, with the density of the nanowires decreasing when the temperature was higher than 800 °C, and the growth rate and nanowire length of nanowires decreasing with an increase in the total chamber pressure.

Catalyst-free metal-organic chemical vapor deposition (MOCVD) is another important synthesis method for ZnO nanowires [109, 119]. The catalyst-free method eliminates the possible incorporation of the catalytic impurities and produces high purity ZnO nanowires. Moreover, the growth temperature of catalyst-free MOCVD is lower than a typical VLS growth temperature [120]. The ability to grow high purity ZnO nanowires at low temperatures is expected to greatly increase the versatility and power of these building blocks for nanoscale photonic and electronic device applications [106]. Zeng et al. [121] reported that well-aligned ZnO nanowires were prepared by MOCVD on Si substrates without catalysts. In their grown process, High-purity diethyl zinc (99.999%) and N<sub>2</sub>O (99.999%) were used as zinc and oxygen sources, respectively, and

N<sub>2</sub> as the carrier gas. The base pressure of the reactor chamber and the working pressure were 10<sup>-5</sup> and 50 torr, respectively. At the start of the process, a thin nucleation layer of ZnO was grown at the low substrate temperature of 400°C. After annealing the nucleation layer, ZnO nanowires were grown on the nucleation layer at the substrate temperature of 650°C.

Physical vapor deposition (PVD) technique has also been used to fabricate ZnO nanowires. The advantages of PVD technique are: (1) the composition of the products can be controlled; (2) there is no pollution such as drain water, discharge gas, and waste slag; and (3) simple process for making samples [122]. The process of PVD usually is the direct thermal evaporation and oxidation of Zn powder at a high temperature and then deposition on the substrate to form the final product [110]. Zhang et al. [122] demonstrated the fabrication of ZnO nanowire arrays on Si substrates by the PVD method at the relatively low temperature of about 500°C. In their synthesis process, high-purity Zn powder was used as the source material and placed in a ceramic boat located at the center of a horizontal tube furnace. The Si substrates were placed on top of the boat to collect the products. The system was quickly heated to 500°C under 50 cm<sup>3</sup>/min N<sub>2</sub> flowing at a pressure of about 10<sup>-3</sup> torr for 1 h and then cooled to room temperature. The optical investigation showed that the ZnO nanowires were of high crystal quality and had attractive optical properties.

#### 2.4.2.2 Solution Phase Synthesis

Solution phase synthesis has many advantages when compared to vapor phase synthesis such as low cost, low temperature, scalability and ease of handling. Generally, solution phase reactions occur at relatively low temperatures (<200°C) compared to

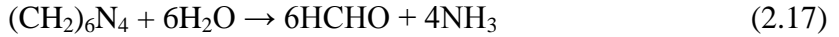
vapor phase synthesis methods. Thus, solution synthesis methods allow for a greater choice of substrates including inorganic and organic substrates. Due to the many advantages, solution phase synthesis methods have attracted increasing interest. Generally, solution phase synthesis is carried out in an aqueous solution and the process is then referred to as the hydrothermal growth method [123, 124].

Hydrothermal methods have received a lot of attention and have been widely used for the synthesis of 1D nanomaterials. In addition, hydrothermally grown ZnO nanowires have more crystalline defects than others primarily due to oxygen vacancies [51]. Nanowires with inherent defects are capable of exhibiting visible light photocatalysis even without doping with transition metals [125]. The general process for vertically-aligned ZnO nanowires grown on a substrate by the hydrothermal method is:

1. A thin layer of ZnO nanoparticles is seeded on a substrate. The seeding layer promotes nucleation for the growth of nanowires due to the lowering of the thermodynamic barrier [126].
2. An alkaline reagent (such as NaOH or hexamethylenetetramine) and Zn<sup>2+</sup> salt (Zn(NO<sub>3</sub>)<sub>2</sub>, ZnCl<sub>2</sub> etc.) mixture aqueous solution is used as a precursor (or growth solution).
3. The ZnO seeded substrate is kept in the growth solution at a certain temperature and a certain period of time.
4. The resultant substrate and growth layer is washed by and dried.

When hexamethylenetetramine ((CH<sub>2</sub>)<sub>6</sub>N<sub>4</sub>, or HTMA) and Zn(NO<sub>3</sub>)<sub>2</sub> are chosen as precursor, the chemical reactions can be summarized in the following equations [97]:

Decomposition reaction:



Hydroxyl supply reaction:



Supersaturation reaction:



ZnO nanowire growth reaction:



One of the key parameters for the growth of ZnO nanowires is controlling the supersaturation of the reactants. It is believed that high supersaturation levels favor nucleation and low supersaturation levels favor crystal growth [127]. If a lot of  $\text{OH}^-$  are produced in a short period, the  $\text{Zn}^{2+}$  ions in the solution will precipitate out quickly due to the high pH environment, therefore,  $\text{Zn}^{2+}$  would contribute little to the ZnO nanowire growth, eventually result in the fast consumption of the nutrient and prohibit further growth of the ZnO nanowires [128]. Thus, the concentration of  $\text{OH}^-$  should be controlled in the solution to maintain low supersaturation levels during the whole nanowire growth process.

#### 2.4.2.2.1 Effect of the ZnO Seeding Layer

Typical pre-seeding methods include thermal decomposition of zinc acetate, spin coating of ZnO nanoparticles, sputter deposition, and physical vapor deposition. In order to seed ZnO particles on the substrate, ZnO seeds must be annealed at certain temperature to improve ZnO particle adhesion to the substrate and nanowire vertical growth alignment. Greene et al. [129] studied the minimum temperature required to form

textured seeds from zinc acetate on a silicon substrate from 100 to 350°C. The results suggest that temperatures between 150 and 200°C are needed for seed alignment, whereas higher temperatures promote seed crystallinity and growth. Baruah et al. [130] have reported that a very uniform thin layer of ZnO nanoparticles could be observed when ZnO seeds are annealed at a temperature of 350°C. However, when the annealing temperature was further increased to 450°C, ZnO crystallized into nanoparticles as well as nanorod like structures. The authors hinted that ZnO seeds annealing at a temperature of about 350 °C would produce the best results for the ZnO nanowire growth.

The texture, thickness and crystal size of the ZnO seed layers also affect the quality of the ZnO nanowire growth [131-134]. Ghayour et al. [131] reported the effect of seed layer thickness on the alignment and morphology of ZnO nanorods. The results showed that the diameter increased, the density decreased, and the length of the nanorods slightly decreased when the thickness of the seed layer increased (Table 2.5). Wu et al. [132] studied the effects of seed layer characteristics on the synthesis of ZnO nanowires. The SEM images showed that the density of nanowires decreased from 35 to 12  $\mu\text{m}^{-2}$  when the thickness increased from 106 to 191 nm and the diameter of the nanowires was found to increase with the seed layer (002) grain size. Ji et al. [134] found that the average diameter of nanowires was increased from 50 to 130 nm and the density was decreased from 110 to 60  $\mu\text{m}^{-2}$  when the seed layer thickness was changed from 20 to 1000 nm. Baruah et al. [130] reported that the nanorods grown on seeds crystallized from a zinc acetate solution have a higher aspect ratio (of the order of 3) than those grown using nanoparticle-seeded substrates.



Without a ZnO seeding layer, ZnO nanowires could be grown on an Au/substrate by introducing a suitable content of ammonium hydroxide into the precursor solution [135]. Au is used as an ‘intermediate layer’ to assist the growth of ZnO nanowires [135].

Table 2.5 The diameter, density and length of ZnO nanorods corresponding to the thickness of the seed layer [131]

Thickness of the seed layer (nm)	Diameter of ZnO nanorods (nm)	Density of ZnO nanorods ( $\mu\text{m}^{-2}$ )	Length of ZnO nanorods (nm)
20	30	213	1052
40	36	209	1007
160	51	184	998
320	72	169	967

#### 2.4.2.2.2 Effect of an Alkaline Reagent

There are some alkaline reagents that have been used to supply  $\text{OH}^-$  during the reaction process such as NaOH, hexamethylenetetramine (HMTA),  $\text{Na}_2\text{CO}_3$ , ammonia, ethylenediamine. When NaOH, KOH, or  $\text{Na}_2\text{CO}_3$  is chosen, the synthesis process usually is carried out at elevated temperatures ( $>100^\circ\text{C}$ ) and pressures in a Teflon-sealed stainless autoclave [136-139]. When HMTA, ammonia or ethylenediamine is chosen, the synthesis process can be carried out at lower temperatures ( $< 100^\circ\text{C}$ ) and an atmospheric pressure. However, HMTA is the most often used due to its advantage in producing high quality ZnO nanowires [140]. HMTA plays different significant roles during the synthesis process. First, HMTA supplies the  $\text{OH}^-$  ions to drive the precipitation reaction by thermal degradation [141]. Second, HMTA acts as a pH buffer by slowly releasing  $\text{OH}^-$  ions through thermal decomposition [140]. The hydrolysis rate of HMTA is

decreased with an increase in pH and vice versa. Third, HMTA attaches to the non-polar facets of the ZnO nanowires and prevents access of the  $\text{Zn}^{2+}$  ions to them thus leaving only the polar (001) face for epitaxial growth [126].

#### 2.4.2.2.3 Effect of Precursor Concentration

To ascertain the relationship between the precursor concentration and the ZnO nanowire growth, Wang et al. [142] carried out a series of experiments by varying the precursor concentration and different ratios of  $[\text{Zn}(\text{NO}_3)_2]/[\text{C}_6\text{H}_{12}\text{N}_4]$ . The effect of the concentration of the precursor on the growth of ZnO nanorods is to increase the average diameter of ZnO nanorods almost linearly from 43 to 70 nm and the average length from 65 to 320 nm, as the precursor concentration increases from 0.008 to 0.04 M (Figure 2.5). The corresponding aspect ratio of the ZnO nanorods increases from 1.8 to 5.8 and then slightly decreases to 4.6 (Figure 2.5 insert). Changes in the  $[\text{Zn}(\text{NO}_3)_2]/[\text{C}_6\text{H}_{12}\text{N}_4]$  ratio did not have a significant effect on the diameters of the ZnO nanorods (Figure 2.6). The aspect ratio of the ZnO nanorod arrays reached a maximum value of 7.25 when the  $[\text{Zn}(\text{NO}_3)_2]/[\text{C}_6\text{H}_{12}\text{N}_4]$  ratio was set to unity (Figure 2.6 insert). Xu et al. [128] studied the nanowire density by varying the precursor concentration with equal molar concentrations of the zinc salt and HMTA. The experimental results showed that the density of the nanowires was closely related to the precursor concentration. From 0.1 to 5 mM, the ZnO nanowire density was increased from 55/100  $\mu\text{m}^2$  to 108/100  $\mu\text{m}^2$ . When the precursor concentration was further increased, the density of ZnO nanowires remained approximately steady with a slight decreasing tendency. The authors explained that the zinc chemical potential inside the body of the solution increases with zinc concentration. To balance the increased zinc chemical potential in the solution, more nucleation sites on

the substrate surface will be generated, and therefore, the density of the ZnO nanowires will increase. However, a continuous increase in the solution concentration may not increase the density of the nanowires when its density is larger than the saturation density.

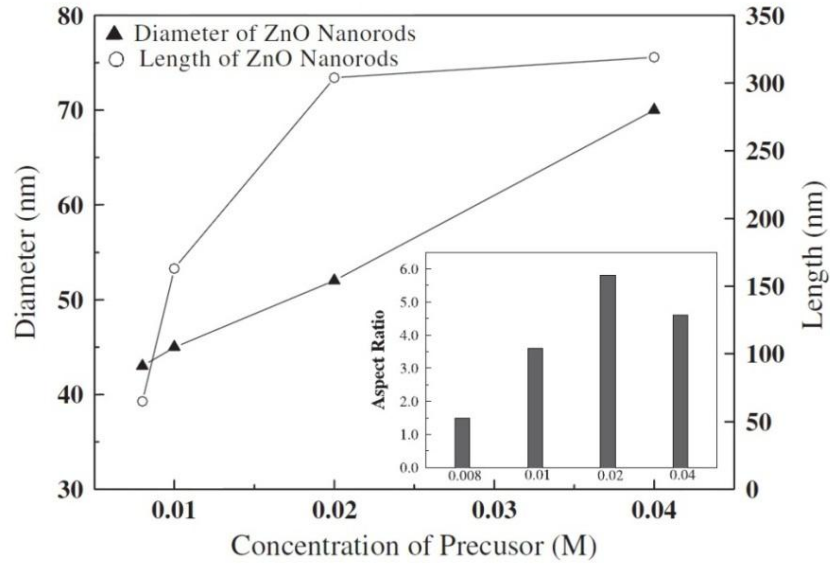


Figure 2.5 Average diameters, lengths and aspect ratios of ZnO nanorods prepared from various precursor concentrations with a Zn(NO<sub>3</sub>)<sub>2</sub>/C<sub>6</sub>H<sub>12</sub>N<sub>4</sub> ratio of 5 [142]

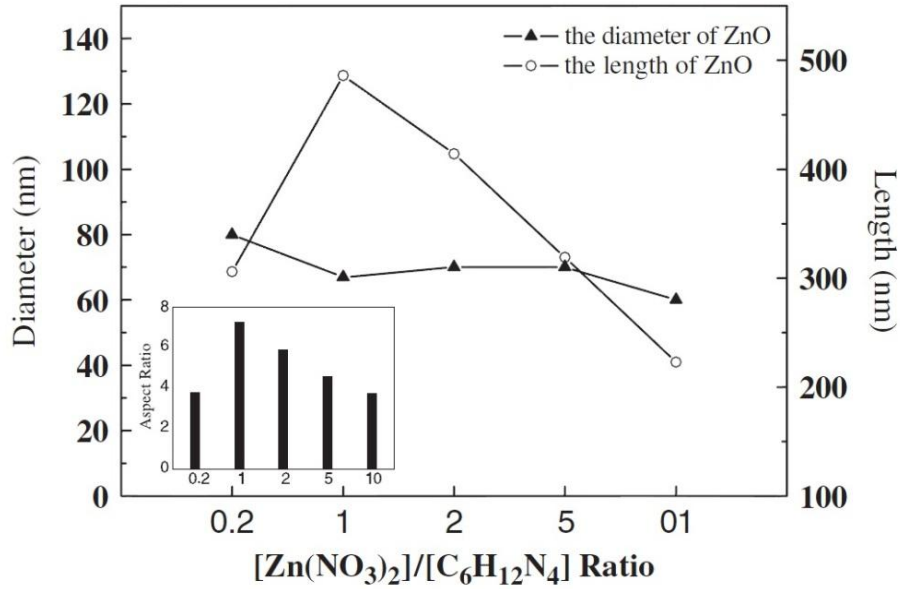


Figure 2.6 Average diameters, lengths and aspect ratios of ZnO nanorods prepared in a 0.04 M precursor solution with various Zn(NO<sub>3</sub>)<sub>2</sub>/C<sub>6</sub>H<sub>12</sub>N<sub>4</sub> ratios [142]

Kim et al. [143] reported that the density and diameter of ZnO nanorods are especially sensitive to the concentration of the reactants. Furthermore, the structural transition was shown by increasing the concentration. At the lowest concentration of  $Zn^{2+}$ , the ZnO nanorods grow as single crystals with a low density and variable orientations. On the other hand, at the highest concentration, the nanorods grow as polycrystals due to the supersaturated  $Zn^{2+}$  source.

#### 2.4.2.2.4 Effect of Growth Duration Time

Yuan et al. [144] synthesized ZnO nanowires by using equimolar (50 mM) zinc nitrate and HMTA at 93°C. The authors reported that the average diameter of ZnO nanowires was increased with growth duration time when the growth time was less than 2.5 h (Table 2.6). However, the average diameter is almost unchanged after that. The authors explained that the growth rate was slowed down after this period due to depletion of the precursor.

Table 2.6 Average diameter of ZnO nanowires change with growth time [144]

Growth time (hr)	Average diameter (nm)
0.5	35
1.0	37
1.5	55
2.0	90
2.5	100
3	100

Baruah et al. [130] carried out ZnO nanowire experiments on zinc acetate seeded substrates for different growth durations from 5-15h. The SEM images showed that both length and diameter of the nanowires was increased with increasing growth duration time but the aspect ratio was reduced. Although nanowire growth slowed down after a certain period, the precursor supply for the ZnO nanowire growth can be replenished by repeatedly introducing fresh solution into the baths to keep up the growth rate [96, 145]. However, the diameter of the nanowires will also continue to increase and eventually connect together to form a ZnO film.

#### 2.4.2.2.5 Effect of Initial Solution pH

Baruah et al. [146] studied the effect of pH variation on the dimension and morphology of ZnO nanorods grown by the hydrothermal synthesis method. ZnO nanorods were grown on pre-seeded glass substrates using the same concentration of zinc nitrate and HTMA as the precursors. The pH of the reaction bath was found to change gradually from 6.4 to 7.3 in 5 h during the growth process. When the growth process was initiated in basic condition (pH 8–12), flower petal like ZnO nanostructures were obtained. Akhavan et al. [147] studied the effect of pH change from 7.5 to 11.44 on the growth of ZnO nanorods by using zinc nitrate and NaOH as precursors. They reported that the diameters of the nanowires were increased with increased pH until they formed a ZnO film when the pH reached a value of 11.44. For a precursor pH value of 11.33, fast growth of ZnO nanorods was observed on the seed layer. The fast growth of ZnO nanorods resulted in a reduction of the optical band-gap energy due to the creation of a greater number of defects in the nanorods during this fast growth.

#### 2.4.2.2.6 Effect of the Growth Substrate

One major advantage of the hydrothermal synthesis method is that almost any substrate can be used for the growth of vertical ZnO nanowires by using a ZnO seeding layer. In this way, ZnO nanowires can grow on a flat surface regardless of the substrate (polymer, glass, semiconductor, metal, and more) by only controlling the growth conditions. ZnO nanowires can also be grown on organic substrates. ZnO nanowires have been successfully grown on polydimethylsiloxane (PDMS) [148], polystyrene (PS) [149], polyethylene terephthalate (PET) [150], polyethylene fibers [151], microfibers [152], polyurethane [153], polyimide [154], paper [155] and other organic substrates like lotus leaf [156].

#### 2.4.2.2.7 Effect of Growth Temperature

Sugunan et al. [126] carried out growth of ZnO nanowires at different temperatures by using equimolar zinc nitrate and HMTA from 60 to 95°C. They reported that hydrothermal growth carried out with 1 mM solution of the precursors at 95°C produced similar nanowire lengths as those grown at 65°C in the same growth period. Thus, the authors suggested that there is no significant difference in the nanowire growth process for different chemical bath temperatures.

#### 2.4.2.2.8 Effect of Additives

The aspect ratio of ZnO nanowires could be affected by the addition of additives. Zhou et al. [157] reported the effect of the addition of polyethyleneimine (PEI) on ZnO nanorods and showed that the average diameter of the nanorods was reduced drastically from 300 nm to 40 nm as with the PEI amount increased from 0 to 12% (v/v) in solution. The authors explained that the PEI molecules were adsorbed on the lateral facets of the

ZnO nanorods due to the electrostatic affinity. Thus, the lateral growth of the nanorods could be largely limited. Chen et al. [158] studied the influence of PEI and  $\text{NH}_3$  on the growth of ZnO nanowires. The SEM image showed that the diameter and length of ZnO nanowires decreased with the addition of PEI. With the addition of  $\text{NH}_3$ , the diameter of the ZnO nanowires was reduced even further.

#### 2.4.2.2.9 Other Factors

Other factors effecting ZnO growth include the heating source, the  $\text{Zn}^{2+}$  source, the external electric field, mechanical stirring, etc. The use of microwave heating instead of conventional heating has recently received great interest [51, 159, 160]. The hydrolyzed method creates defective crystallites under microwave irradiation and leads to a faster growth process as compared to the conventional process [51, 161]. Zinc salts including acetates, nitrates, perchlorates, and chlorides. The counter-ion of zinc often affects the crystallite morphology by acting as promoter or inhibitor in the nucleation and growth processes [139]. An external electric field could also affect the growth rate, and depends on the electric field direction and the applied voltage. Mechanical stirring could increase the growth rate.

#### 2.4.2.3 Modification of ZnO Nanowires

The solar energy utilization efficiency could be improved by modifying the photocatalyst semiconductors by doping with transition metals [162]. ZnO doping with transition metals (nickel (Ni) [103], cobalt (Co) [163], and silver (Ag) [164], etc.) shows enhancement in the absorption of light due to the creation of dopant energy levels below the conduction band. Besides, the transition metals also trap free electrons, thus lowering the electron-hole pair recombination rate leading to an increase in the photocatalytic

efficiency in ZnO nanowires [51, 165]. Wu et al. [166] reported that Cr doped ZnO nanowires have better photoactivity for decoloration of methyl orange as compared to pure ZnO and P25 under visible light irradiation. Lu et al. [167] reported that the Co doped ZnO samples have an extended light absorption range and increased photocatalytic activity of alizarin red dye decomposition under visible light irradiation as compared with pure ZnO nanorods. Jia et al. [168] showed an increase in the photocatalytic activity of La-doped ZnO nanowires in the degradation of Rhodamine B (RhB) with the optimal doping content being about 2% in terms of the photocatalytic activity efficiency. Wu et al. [169] reported that the photocatalytic activity of 3% Sb doped ZnO nanowires was superior to undoped ZnO nanowires both under UV and visible-light testing. Li et al. [164] investigated the structural, electronic, and optical properties of Ag-doped ZnO nanowires using first-principle calculations based on DFT. The results provided theoretical evidence that Ag-doped ZnO nanowires could also have potential applications in photocatalysis due to the increase in visible-photocatalytic activity. Other dopings of ZnO nanowires, such as Sn [170] and Na [171], have also been reported and have shown an enhancement of photocatalytic activity for the degradation of organic compounds in water. In addition to doping, Jung et al. [172] reported the fabrication of CuO–ZnO nanowires on a stainless steel mesh for highly efficient photocatalytic applications.

## **2.5 Photocatalytic Reactors**

In general, the photocatalytic performance for air purification greatly depends on the design of an efficient photocatalytic reactor. Air contaminant removal by photocatalytic reactors is a surface reaction process consisting of three important steps:



first, the pollutants have to transfer to the catalyst surface; second, adsorption/desorption phenomena occur; and third, the pollutants are decomposed by the photocatalyst. Thus, the main performance parameters of a photocatalytic reactor are the mass transfer rate, the kinetic reaction rate, and the reaction surface area [32]. Normally, a photocatalytic reactor should contain two parts: the reactor structure and a light source. The reactor structure supports not only supports photocatalyst but also the airflow channels. An ideal photocatalytic reactor structure for indoor air purification should have: a) high specific surface area for a large reaction area; b) appropriate light directly irradiating on the reaction surface; and c) high mass transfer, residential time and low pressure drop.

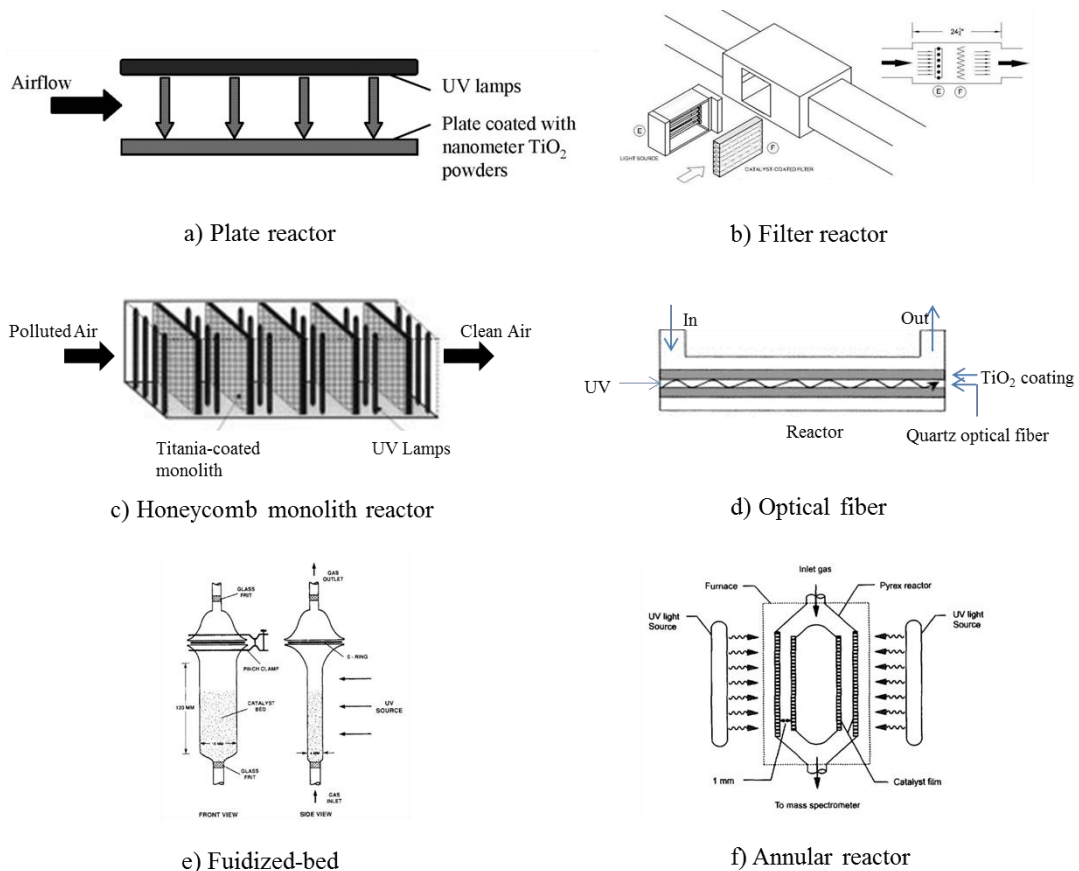


Figure 2.7 Schematic diagrams of various photocatalytic reactors for air purification. (a) Plate [173]; (b) Filter [21, 22, 26]; (c) Honeycomb monolith [174]; (d) Optical fiber [175]; (e) Fluidized-bed [176]; (f) Annular [177]

There are various photocatalytic reactors that have been reported for air purification purposes in the literature [22, 174, 176-179]. However, most of the studies are only based on laboratory scale tests instead of real applications. Most of these reactors employ immobilized photocatalysts on solid substrates. They also have been categorized based on their configurations [32, 66]. Figure 2.7 shows the schematic of various representative photocatalytic reactors for air purification. Most other photocatalytic reactors for air purification are developed based on these configurations.

The plate type reactor has the simplest configuration compared to other reactors (Figure 2.7a). The catalyst is coated on a certain flat substrate and the appropriate light is applied on it. The air contaminants contact with the catalyst when air passes through the reactor channel carrying out the photocatalysis process. Due to its configuration and the light's direct irradiation on the reaction surface, advantages of this type of reactor include simplicity, small pressure drop, and the possibility of obtaining large reaction rates. The drawback of this type of reactor is the smaller reaction area compared to some others. The plate type reactors have been used by many research groups [180-186]. Puddu et al. [184] studied the influence of crystallinity, crystal phase, and UV radiation intensity on trichloroethylene (TCE) degradation by using a flat plate photocatalytic reactor. Yang et al. [36] used the plate type reactor to decompose formaldehyde by measuring the reaction coefficients and showed that formaldehyde is degraded. Salvado-Estivill et al. [187] reported the photocatalytic oxidation of trichloroethylene (TCE) by a plate reactor in the study of two dimensional modeling of a flat plate photocatalytic reactor. Mo et al. [188] studied the by-products resulting from the photocatalytic oxidation of toluene by a plate reactor.

The filter type reactor was first proposed and developed by Goswami et al. [22] for the disinfection of indoor air (Figure 2.7b). In general, the catalyst is coated on a pleated fiber filter and the light is applied on the filter. The pleated filter is used to reduce the pressure drop and also provide additional surface area for photocatalysis. The contaminants contained in the air flow through the filter come in contact with the catalyst and photocatalysis occurs. Small portable in-room photocatalytic devices have a similar reactor design in a compact setup. Goswami et al. [22] developed a recirculating duct facility with a catalyst coated filter for the disinfection of indoor air and demonstrated 100% destruction of *S. marcescens* bacteria. Vohra et al. [21] studied the performance of the Ag doped TiO<sub>2</sub> coated filter and showed complete inactivation of a range of microorganisms. Lin et al. [189] investigated the inactivation of microorganisms by a commercial TiO<sub>2</sub> coated filter in air and concluded that the process was effective against airborne microorganisms.

A honeycomb monolithic reactor has a honeycomb structure which contains certain number of channels. The catalyst is supported on the honeycomb structure (Figure 2.7c). This type reactor provides a large catalyst surface area and a low pressure drop. The design has been used for the automobile exhaust emission control [190, 191]. However, the reaction rate could be limited because the UV light is parallel to the reaction area resulting in insufficient light irradiation. Sauer et al. [192] reported acetone oxidation in a photocatalytic monolith reactor and indicated that the honeycomb monolith configuration could remove all major classes of air contaminants. Hossain et al. [174] developed a mathematical model to describe the performance of the honeycomb monolith photocatalytic reactor. Model predictions matched the experimental formaldehyde

conversion measurements for a range of inlet concentrations, air humidity levels, monolith lengths. Zhong et al. [193] also developed a model for predicting the performance of a honeycomb monolith reactor used in building mechanical ventilation systems for indoor environment applications. The model was validated with experimental data.

Optical fiber reactors utilize single or a bundle of optical fibers as the light source with the  $\text{TiO}_2$  directly coated on the optical fibers (Figure 2.7d). Optical fibers usually are made from UV-transparent material like quartz. Optical fiber reactors could obtain higher quantum yields due to the relatively uniform distribution of light radiation. However, the heat may build up inside the optical fiber. The reactor building cost usually is higher than others. Sun et al. [194] studied the  $\text{TiO}_2$  coated on 18000 pieces of optical fibers and used as a photocatalytic filter for the decomposition of gaseous organic compounds. They reported that both higher efficiency of light utility and larger processing capacity were obtained. Choi et al. [175] employed quartz fiber as a light transmitting support of  $\text{TiO}_2$  to investigate the gas phase photocatalytic oxidation of acetone and reported a steady state conversion up to 80% in a continuous flow reactor at ambient temperature and pressure. Wang et al. [195] employed a batch type photoreactor containing a bundle of  $\text{TiO}_2$  coated quartz fibers to study the photocatalytic degradation of gaseous benzene in air streams with 80% benzene being decomposed after 4 hours.

For fluidized-bed reactors, the air streams vertically pass through a transparent container filled with the catalyst bed (Figure 2.7e). A light source is placed on the side of the reactor. A typical catalyst bed is comprised by  $\text{TiO}_2$ -silica gels with the  $\text{TiO}_2$  supported on silica gel particles of 0.25-0.45mm diameter [176, 196]. The fluidized-bed

reactors are designed to achieve good contact between reactants and catalyst. However, the penetration of UV light is restricted by the catalyst and also with larger a pressure drop [64]. Zhang et al. [197] using a fluidized bed reactor to study the photocatalytic degradation of mixed gaseous carbonyl compounds and reported that the photocatalyst had a high adsorption performance and a good photocatalytic activity for four carbonyl compound mixtures. Lim et al. [198] developed an annulus fluidized bed reactor and showed it was an effective tool for trichloroethylene (TCE) degradation with efficient utilization of photon energy.

The annular reactors are comprised of two concentric cylinders forming an annular region with a certain gap (Figure 2.7f). The catalyst is coated on the interior wall of the annular. The light source could be located around the reactor or in the center. The thickness of the catalyst film is thin enough to allow the entire catalyst to be illuminated by UV light. Similar to the plate type reactor, the annular type reactors also have a smaller reaction area. The annular reactors have been used by some research groups in their study [199-203]. Larson et al. [177] used annular reactors in his transient studies of 2-propanol photocatalytic oxidation on titanium dioxide showing that the 2-propanol was photocatalytically oxidized. Jacoby et al. [199] have reported heterogeneous photocatalysis for the control of volatile organic compounds in indoor air with an annular reactor and showed that the representative contaminant benzene was oxidized. Assadi et al. [204] studied the influence of the mass transfer and the relative humidity on the photocatalytic oxidation of trimethylamine and isovaleraldehyde in an annular reactor.

In order to improve the overall effectiveness, other air cleaning technologies such as HEPA, activated carbon and ionizer generator have been integrated with photocatalytic

reactors to form a combined type system [205]. The systems usually contain a blower or fan, a particulate filter, a light source and a photocatalyst (Figure 2.8). It was common that the photocatalyst was fixed on a substrate such as a honeycomb type construction to reduce the pressure drop.

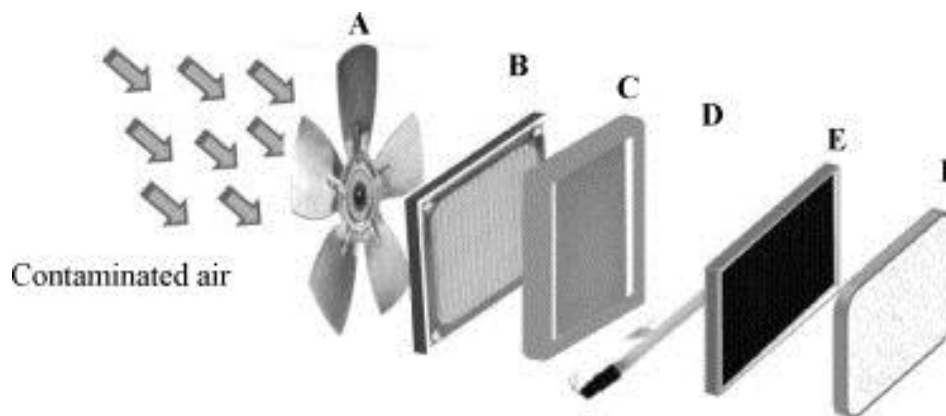


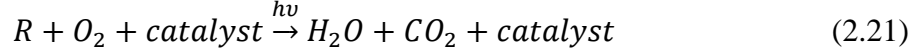
Figure 2.8 Schematic of the photocatalytic indoor air treatment device. (A) fan, (B) particulates (HEPA) filter, (C) photocatalyst, (D) light source, (E) activated carbon filter (optional) and (F) ionizer generator (optional). [205]

## 2.6 Parameters that Influence a Photocatalytic Reactor

The kinetic reaction and mass transfer rate are two of the main performance parameters of a photocatalytic reactor.

### 2.6.1 Kinetic Reactions

Kinetic studies of photocatalytic reactions at various operational conditions have been successfully performed by many research groups [31, 33-35, 206-213]. Some of them have modeled the radiation field for different reactor configurations [33-35, 207, 209, 211]. The photocatalytic reaction rate determines the performance of the photocatalytic reaction for the removal of air pollutants. The Langmuir-Hinshelwood (L-H) model has been widely used to formulate the rate equations for photocatalytic reactions [31, 66, 208]. For the surface reaction:



the reaction rate  $r$  is in proportion to the coverage of the reactants:

$$r = -\frac{d[R]}{dt} = k\theta_R\theta_{O_2} \quad (2.22)$$

where  $k$  is the reaction constant,  $\theta_R$  is the fractional coverage of  $R$  adsorbed on the catalyst surface, and  $\theta_{O_2}$  is the fraction of oxygen adsorbed on the surface.

According to the Langmuir model for monolayer adsorption the reaction is [56],

$$\theta_R = \frac{q}{q_t} = \frac{K_{ads}C_{R,surf}}{1+K_{ads}C_{R,surf}} \quad (2.23)$$

where  $q$  is the number of adsorbed sites,  $q_t$  is the total number of adsorption sites,  $K_{ads}$  is the adsorption equilibrium coefficient, and  $C_{R,surf}$  is the concentration of the reactant  $R$  adjacent to the reaction surface.

Because of the abundant  $O_2$  present in the atmosphere,  $\theta_{O_2}$  is normally close to 1.

Thus, equation (2.18) could be rewritten as unimolecular type L-H model:

$$r = k\theta_R = k\frac{K_{ads}C_{R,surf}}{1+K_{ads}C_{R,surf}} \quad (2.24)$$

In many study cases, the stream concentration of contaminants ( $C_R$ ) is usually used instead of  $C_{R,surf}$  because  $C_{R,surf}$  is difficult to obtain. For low concentration of air contaminants, ( $C_R$ ) is almost equal to zero, which makes the denominator in the L-H expression equal to one. Thus, equation (2.20) could be reduced to a pseudo-first-order expression:

$$r = -\frac{d[R]}{dt} = kC_R \quad (2.25)$$

Equation (2.21) has been widely used in practical studies for a single compound. Indoor air pollutant levels are typically on the order of ppm [214, 215], which is low

enough for the reaction rate to follow the pseudo-first-order expression. Kinetic experiments usually are required to study the various influencing factors of the photocatalytic reaction rate. The influencing factors of the kinetic reaction rate include light source and intensity, pollutant concentration, humidity, temperature, and others.

#### 2.6.1.1 Light Source and Intensity

The light source is the energy provider in the photocatalytic process. For the most common photocatalysts (TiO<sub>2</sub>, ZnO, etc.), only ultraviolet (UV) light and specifically near ultraviolet (UV) light could activate the photocatalyst due to the wide band gap energy. UV light is the electromagnetic radiation in the 10-400 nm wavelength range. UV light can be subdivided as UVA, UVB, UVC and VUV. UVA covers from 315 to 400 nm wavelength range, UVB is from 280 to 315 nm and UVC is from 200 to 280 nm. Radiation in the 10 to 200 nm is considered as vacuum ultraviolet (VUV) because it is absorbed strongly by air.

For TiO<sub>2</sub> photocatalysis, both artificial light and solar light could be used as the light source. With artificial light, low energy UVA light (black light) is the most widely used light source for TiO<sub>2</sub> photocatalysis, which is safe for human exposure and does not produce ozone [23]. Typical UVA lamps emit light in a wavelength band between 300 and 400 nm with an approximately Gaussian spectral distribution ( $\lambda_{\text{max}}=350$  nm). Visible light could be used with a modified TiO<sub>2</sub> photocatalyst such as nitrogen doped TiO<sub>2</sub> and other visible responsive photocatalysts [61, 78, 216-219].

The light intensity has a crucial role on the reaction rate. Under certain conditions, the reaction rate increases with increasing light intensity. Obee et al. [178] studied TiO<sub>2</sub> photocatalysis for VOC oxidation. They summarized that for a UV intensity ( $I$ ) above



one sun (about 4-5mW/cm<sup>2</sup> for wavelengths below 400nm), the oxidation rate increases with the square root of the intensity ( $r = k\sqrt{I}$ ), and for UV intensity below one sun, the oxidation rate increases linearly with the intensity ( $r = kI$ ). Salvado-Estivill et al. [33] developed a kinetic reaction model by modeling the radiation field. They used the linear source spherical emission model (LSSE), which has been proposed for tubular lamps in the literature [220], to predict the incident intensity of radiation on the surface of the catalyst for different lamp arrangements and positions. Then they correlated the light intensity to the kinetic reaction (Eq.2.10) and got the Trichloroethylene (TCE) concentration on the photocatalytic plate. Queffeuilou et al. [34] also modeled the radiation field by simulating with light simulation software (SPEOS, OPTIS). The software can provide irradiance maps. Then they integrated the radiation model with CFD and experimental data to simulate the concentration of acetaldehyde in the room.

#### 2.6.1.2 Contaminant Concentration

The Langmuir-Hinshelwood model is widely used to describe the effect of pollutant concentration [33, 34, 206]. In equation (eq.2.10), when  $C_{R,surf}$  is very high, which gives  $K_{ads}C_{R,surf} \gg 1$ , the equation will become zero order. Therefore, the rate of the kinetic reaction becomes the reaction-limiting step. On the other hand, when  $C_{R,surf}$  is very low, which gives  $K_{ads}C_{R,surf} \ll 1$ , the equation (Eq. 2.10) will become first order. Therefore, mass transfer becomes the reaction-limiting step.

#### 2.6.1.3 Humidity

Water vapor is necessary in the photocatalysis process. It reacts with the hole and generates the primary oxidant hydroxyl radical (OH•). During the photocatalysis process, the continuous consumption of hydroxyl radicals (OH•) requires supplement to maintain

the catalyst activity. The photocatalytic oxidation of organic compounds will be seriously retarded if water vapor is absent, but excessive water vapor can also decrease the photoactivity because water molecules compete for the active sites with the pollutants. The optimum water vapor content is exists and is a suitable equilibrium between consumption and adsorption.

Goswami et al. [22] studied the humidity effect on disinfection of indoor air and reported for the first time that the impact parameter is relative humidity rather than absolute humidity. They reported that there was complete inactivation of the organisms at a relative humidity of 50%, but 10% of the organisms were still viable at a relative humidity of 85% [22]. Assadi et al. [204] studied the effect of relative humidity on the photocatalytic oxidation of trimethylamine (TMA) and isovaleraldehyde (ISOV). They reported that the optimum relative humidity values were equal to 40% for isovaleraldehyde (ISOV) and 25% for trimethylamine (TMA). Pichat [43] explained the humidity effects in air photocatalytic treatment. The water vapor concentration of indoor air usually is several orders higher compared to pollutant concentration (at 298K and 1 atm, a 1% change in relative humidity corresponds to about 300 ppmv H<sub>2</sub>O). The presence of water vapor layers could hinder the approach of the pollutants to the catalyst surface and hence the dissociation of pollutants by mere adsorption becomes unlikely [43].

#### 2.6.1.4 Temperature

In the catalytic reaction process, the temperature affects pollutant adsorption, kinetic reaction and product desorption on the surface of the catalyst. The kinetic reaction coefficient usually follows the Arrhenius equation:  $k = A \exp\left(\frac{-E_a}{RT}\right)$ . Thus, the higher

temperature corresponds to larger kinetic reaction coefficients. However, the affected kinetic reaction coefficient change with temperature is generally small. This is because the photodegradation of organic compound is governed by hydroxyl radical (OH•) reactions and the activation energy is close to the hydroxyl radical (OH•) formation. Generally, increasing the temperature enhances the recombination of charge carriers and the desorption process of adsorbed reactants, resulting in a decrease of the total reaction rate [221]. On the other hand, desorption of reaction products could become the rate-limiting step of the process at lower temperatures. The total reaction rate should be the combined process of kinetic reaction, adsorption of reactants, desorption of products, and recombination rate of charge carriers. Table 2.7 summarizes the impact factor of the total reaction rate with increased temperature. The optimum temperature may be found to be different for each organic compound.

Table 2.7 The impact of total reaction rate with increasing of the temperature

<b>Impact factors</b>	<b>Appearance of impact factors</b>	<b>Reaction rate (r)</b>
kinetic reaction coefficient (k)	Increased	Increased
Absorption of reactants	Decreased	Decreased
Desorption of products	Increased	Increased
Recombination rate	Increased	Decreased

Yu et al. [222] found the optimal temperature as 25°C for formaldehyde, but Sano et al. [223] found that the acetaldehyde degradation rate increases with the temperature from 40 to 140°C. This means the optimal temperature for acetaldehyde may be more

than 140°C. Chang et al. [224] reported the conversion and mineralization of acetone decreased at temperatures higher than 138°C. Although the optimum temperatures are different for different organic compounds, normally, the photocatalytic reaction for indoor air applications could be carried out at room temperature and does not need an additional heating or cooling system.

#### 2.6.1.5 Other Factors

Other influencing factors of the kinetic reaction include O<sub>2</sub>, NO, SO<sub>2</sub>, catalyst activity, catalyst loading, etc. The oxygen is essential and usually acts as an oxidant in the photocatalysis process. Generally, the decomposition rate increases with an increase in the oxygen content [224]. The presence of NO has a positive impact on the photocatalysis process. This is because hydroxyl radicals (OH•) are generated from the photodegradation of NO [225]. The presence of SO<sub>2</sub> inhibits the photocatalytic process because sulfate ions compete with the pollutants for adsorption sites [225]. In the gas phase, photocatalytic activity has been observed to decrease with time. This may be due to the loss of active catalyst sites on the reaction surface by reaction residues or by photopolymerization of some species. They could be adsorbed onto the catalyst and block the active sites and thus reduce the photocatalytic activity. For catalyst immobilized systems, there is an optimum thickness of the catalyst film. Thick films favor catalytic oxidation and the resultant degradation rate is increased. On the other hand, the internal mass transfer resistance for photogenerated electrons/holes would increase with increasing thickness and the degradation performance would be reduced [226].

## 2.6.2 Mass Transfer

In photocatalysis, mass transfer is the process that transfers the contaminants from the mainstream to the reaction surface and the reaction products from the reaction surface to the flow mainstream [227]. This is particularly significant in heterogeneous photocatalysis when the photocatalyst is immobilized on the support [228]. In order for photocatalysis to be effective, it is necessary for the contaminants to come in close contact with the catalyst. However, the mass transfer ability of the photocatalytic reactor is the bottleneck factor in many cases.

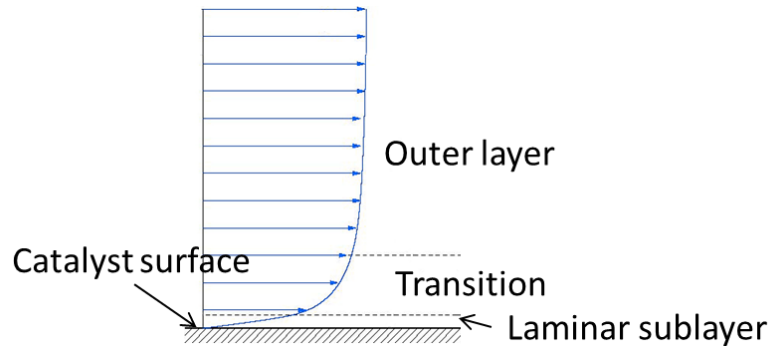


Figure 2.9 A laminar sublayer is formed when air flow on a smooth catalyst surface

For many types of reactor configurations (plate, honeycomb, annular, etc.), the flow direction of air is parallel to the catalyst surface (Figure 2.7). When the air flows parallel to a smooth catalytic surface, a laminar sublayer is formed over the surface that impedes the mass transfer of reactants to the catalyst and the reaction products to the main flow, thus, adversely affecting the photocatalytic reaction rate. Moreover, indoor air pollutant levels are typically lower (ppm level) [214, 215], which requires more mass transfer for an effective heterogeneous photocatalysis. Figure 2.9 presents air flow on a smooth channel (the channel could be a model of plate, honeycomb, or annular type

reactor channel). The walls could represent the reaction surface where the catalyst is coated on it.

Although mass transfer plays a significant role in photocatalysis, it still has not received great attraction in the photocatalytic field. There are only a few research groups that have considered the effect of the mass transfer in their photocatalytic studies.

Mo et al. [229] developed a model to analyze the removal of VOCs by taking into consideration the photocatalytic reaction and the mass transfer coefficients. The key parameter of the photocatalytic reactor is the number of mass transfer units (NTUm), which represents a simple linear product of three dimensionless parameters: the area ratio of the reaction area to the cross-sectional area ( $A^*$ ), the Stanton coefficient of mass transfer ( $St_m$ ), and the reaction effectiveness ( $\eta$ ).  $A^*$  represents the geometric and structural parameters of a photocatalytic reactor. The  $St_m$  shows the impact of the degree of alignment between the fluid and mass flow fields, and reflects the mass transfer rate of the reactor.  $\eta$  describes the relationship between the photocatalytic reaction rate and the mass transfer rate. By using this relationship and the parameters, the bottleneck of the photocatalytic reactor performance can be determined and excellent photocatalytic reactors could be designed. Bouzaza et al. [230] studied the contribution of mass transfer and chemical reaction steps in the photodegradation process. The limitation step of the VOCs photodegradation is evaluated. A design equation, which is based on both the Langmuir-Hinshelwood (L-H) and the mass transfer model, is proposed. Krishnan et al. [231] modified the Langmuir-Hinshelwood (L-H) kinetic model based on experimental observations and yielded a design equation. The equation can be used as the basis for the photoreactor scale-up as well as to find the mass transfer and reaction resistances in the

photoreactor. Passalia et al. [232] have studied the photocatalytic degradation of formaldehyde and presented a non-linear expression based on the mass balance and rate expression to estimate the kinetic parameters. Bimie et al. [233] investigated the influence of species mass transfer on the overall reaction rate of a flat plate photoreactor. They developed a kinetic model by incorporating the mass transfer theory.

Although some researchers have started to pay attention to the mass transfer in the kinetic model study, very few have studied how to increase the mass transfer in a photocatalytic reactor. The conventional method for increasing the mass transfer on the catalyst surface is by increasing the air flow rate in the reactor [33, 36, 206]. However, increasing airflow rate reduces the residence time of the pollutants and leads to incompletely contaminants destruction and more intermediates. An ideal reactor design would be one which enhances the mass transfer rate of the contaminants to the catalyst surface and also increases the residence time.

Vohra [12] described a commercially available honeycomb reactor in his dissertation that the catalyst is coated on a non-uniform rough surface as the basis for his study of the effect of roughness on the turbulence of air flow on the surface (Figure 2.10). He further concluded that the catalytic coating on a rough surface was highly effective in the destruction of contaminants when compared to a similar reactor configuration without surface roughness elements. Based on Vohra's study, a rough catalyst surface could create local wall turbulence and enhance the convective mass transfer of the contaminants to the catalyst surface and thus lead to an increase in the effectiveness of photocatalysis. However, the study did not determine the optimum surface roughness shape and geometry to maximize the effectiveness of photocatalytic air cleaning.

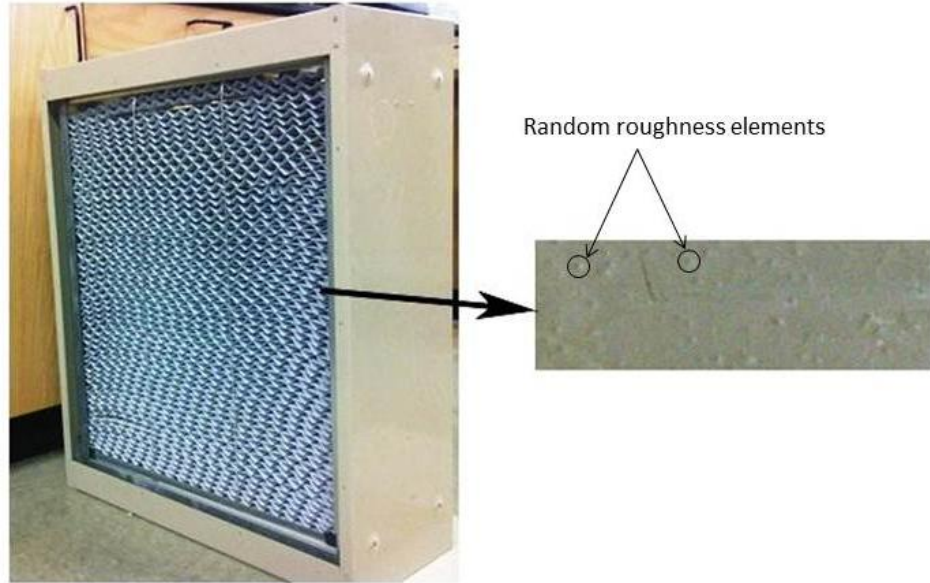


Figure 2.10 A honeycomb photocatalytic reactor with non-uniform roughness elements on the catalyst surface

Chen et al. [234] developed a convective mass transfer field synergy equation with a specific boundary condition for photocatalytic oxidation reactors. The concept of convective mass transfer field synergy came from convective heat transfer. They explained that increasing the field synergy between the velocity and contaminant concentration gradient fields could enhance the convective mass transfer and increase the contaminant removal effectiveness of photocatalysis. First, they used the field synergy equation to analyze and determine the best field synergy for a given viscous dissipation in a plate reactor. Then, the optimal velocity pattern in the reactor channel is obtained for the enhancement of the mass transfer. Based on the optimal flow pattern, they introduced discrete inclined ribs on the surface of the reactor channel to produce a vortex flow pattern. Their experimental study showed that the contaminant removal effectiveness for the discrete inclined ribs on catalyst surface reactor is increased compared to a smooth



plate reactor. However, they did not try to optimize the size, shape, arrangement of rib to match the flow pattern in the reactor channel.

## **CHAPTER 3: THEORETICAL ANALYSIS OF PHOTOCATALYTIC REACTORS WITH SURFACE ROUGHNESS<sup>1</sup>**

### **3.1 Introduction**

Surface roughness elements have a great effect on the turbulent flow structure [235-238]. An early study on the effect of surface rib roughness on turbulent flow, performed by Perry et al. [235], compared different pitch ratios of square roughness elements. They proposed two primary types of square roughness elements that were classified as either d-type or k-type based on the pitch ratio ( $p/e$ ), where  $p$  is the pitch and  $e$  is the height of roughness (Figure 3.1). The d-type roughness, in which the pitch ratio ( $p/e$ ) is less than four, was characterized by a fully separated flow over the inter-rib vortex and thus did not affect the main flow. On the other hand, the k-type roughness, in which the pitch ratio ( $p/e$ ) is greater than four, was characterized by a separated flow over the initial rib that became partially reattached before encountering the upstream face of the next rib and led to vortices and mixing eddies.

More recently, numerical investigations of turbulent flow over rough surfaces have been carried out to provide a better understanding of the turbulence characteristics [238-240]. A computational study by Cui et al. [238] further explored the effect of rib

---

<sup>1</sup> Portions of these results have been previously published (Yangyang Zhang, Elias K. Stefanakos, D. Yogi Goswami. Effect of photocatalytic surface roughness on reactors effectiveness for indoor air cleaning. *Building and Environment*, 61, 188-196, 2013) or under review (Yangyang Zhang, Elias K. Stefanakos, D. Yogi Goswami. Optimum photocatalytic reactor performance with surface roughness arrangement for indoor air cleaning. *Building and Environment*, 2013) and are utilized with permission of the publisher.

spacing for turbulent channel flow exhibiting either d-type or k-type roughness. In d-type roughness, the separation eddies were confined to the gaps between the ribs. For k-type roughness, flow separation and reattachment occurs between two adjoining ribs. Subsequently, much larger and more frequent eddies are thrown into the outer flow, resulting in a strong interaction between the roughness layer and the outer flow. The experimental studies by Wang et al. [241] supported the results of Cui et al. [238].

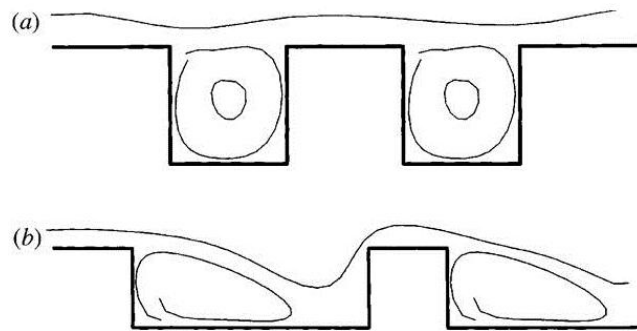


Figure 3.1 Sketch of roughness. (a) d-type, and (b) k-type. Flow is from left to right [242]

The impact of surface roughness on the characteristics of fluid flow has been widely studied. A number of reports have shown that the effect of roughness elements leads to an enhanced mass/heat transport [243-246]. The use of artificial roughness has been successfully developed for the enhancement of heat transfer in nuclear reactors, turbine blades, and solar air heaters [247-249]. As in the case of heat transfer and mass transfer, artificial roughness has also been studied to enhance mass transfer. Zeng et al. [250] studied the effect of surface roughness on mass transfer in a flat-plate microchannel bioreactor and showed that the mass transfer in the rough channel was enhanced. Mobarak et al. [251] measured the mass transfer at the inner surface of smooth and rough annular ducts under developing flow conditions. They reported that the rate of mass transfer was increased 200% under certain conditions for rough duct.

The major effect of roughness elements is to enhance the turbulent mixing thus leading to an enhanced mass/heat transport [238]. An experimental study, conducted by Simonich et al. [245], reported a 5% increase in the heat transfer for every 1% increase in the turbulence intensity. Sanitjai et al. [252] reported that mass transfer (Sherwood number) increases about 60% as the free stream turbulence intensity increases at by 23% in their experimental study of the effect of free stream turbulence on the local mass transfer from a circular cylinder. Moravejin et al. [253] also reported that mass transfer increased greatly with increased turbulence in their experimental investigation. Turbulence intensity often refers to the turbulence level. Although the effect of surface roughness elements in enhancing heat/mass transfer has been known for a long time, its effect on photocatalytic reactor has not been previously investigated.

The primary purpose of the present study is to enhance the effectiveness of the photocatalytic process by increasing the turbulence intensity in the reactor channel with a rough catalyst surface. Different shapes, sizes and arrangements of the surface roughness have been numerically studied to determine the maximum enhancement of turbulence intensity in the reactor duct. Our hypothesis is that increased local turbulence intensity enhances that effectiveness of photocatalysis by bringing pollutant molecules close to the catalytic surface.

### **3.2 Two Dimensional Analysis of Turbulence Intensity with Roughness Patterns**

The effect of different shapes, sizes, and pitch ratio (p/e) roughness elements could be investigated either in two dimensional (2D) or in three dimensional (3D)

photoreactor passages. In order to minimize the need of computer memory and computational time, a 2D photoreactor passage with transverse ribs was considered.

### 3.2.1 Details of the Two Dimensional Photoreactor Passage Geometry

The photoreactor passage was assumed to be a rectangular duct with a cross-section of  $2.54 \times 12.7$  cm ( $1 \times 5$  in,  $H \times W$ ), and length ( $L$ ) of 63.5cm (25in). The passage was divided into three parts: inlet section, test section, and outlet section (Figure 3.2). The inlet and outlet sections were smooth ducts to reduce the end effects of the test section. The lengths of the inlet, test, and outlet sections were 25.4, 25.4, and 12.7cm (10, 10, and 5in), respectively. The height of the passage was 2.54cm (1in). The roughness elements were introduced on the bottom surface of the test section.

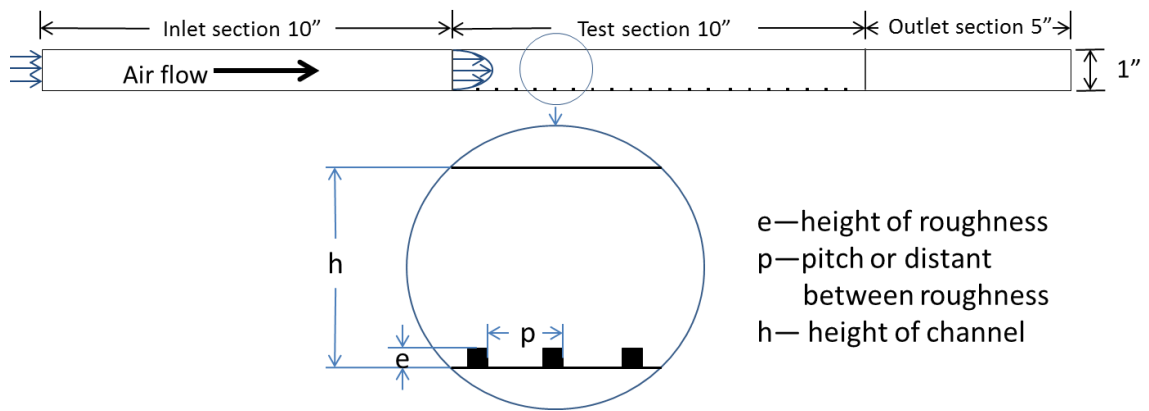


Figure 3.2 Photoreactor channel with surface roughness elements on the bottom wall of the test section

### 3.2.2 Roughness Element Geometry and Range of Parameters

Five different shapes of the roughness element were studied to ascertain the optimum size, shape, and arrangement (Figure 3.3). The roughness elements were placed on the bottom wall of the reactor channel where the catalyst was coated (Figure 3.2). The different ranges of roughness parameters were summarized in Table 3.1.

Table 3.1 The different ranges of parameters of the studied roughness element






Study items	Shapes	e/h	p/e	w/h	w/e	$\alpha$	$\Phi$
pitch ratio		0.05	2~20	0.02 for chamfered	0.4 for chamfered	75° for triangle	45° for chamfered
height		0~0.2	10	0.01	----	----	----
triangle		0.05	10	----	----	15°~89°	----
chamfered		0.05	10	0.02	0.4	----	-60°~60°
rectangle		0.05	10	0.001~0.2	0.2~4	----	----



Figure 3.3 Five different shapes of the roughness element studied in this work

### 3.2.3 Mesh

For a 2D study, meshing was applied by using the commercially available software Gambit 2.3.16. Because of larger velocity gradients, the mesh is more condensed near wall regions. To ensure that the results are grid-independent and well-resolved, the simulations are repeated with different fine levels of meshing. It was determined that there are no noticeable differences in the solutions when the number of cells in each set of geometries is around 250,000 or greater.

### 3.2.4 CFD Analysis

A 2D analysis of air flow through the rectangular duct with transverse rib roughness was carried out using the commercially available CFD software ANSYS Fluent 13.0. The following assumptions were made in the mathematical model: a) the flow is steady, fully developed, and turbulent; and b) the working fluid, air, is incompressible under the operating conditions.

The Velocity-inlet has been considered as the inlet boundary condition and pressure-outlet as the outlet boundary condition in the ANSYS Fluent. The range of Reynolds number (Re) was considered from 2900 to 8700. Thus, the average air flow rate varies from 1 to 3 m/s, corresponding to the Reynolds number. The boundary condition of the outlet pressure was equal to the atmospheric pressure, and no slip wall boundary conditions were used for the analysis. The second order upwind numerical scheme and

SIMPLE algorithm were used to discretize the governing equations. A residual value equal to  $10^{-6}$  was applied for the resulting calculation convergence. The magnitude of the turbulence intensity in the duct was studied to understand how the different shapes, sizes and arrangements of the roughness affect the air flow.

### 3.2.5 Numerical Modeling

The “realizable k-epsilon (k- $\epsilon$ )” model with Enhanced Wall Treatment was used for the solution of the turbulent momentum equations. The k-epsilon (k- $\epsilon$ ) model was chosen because its simplicity, reasonable accuracy, and wide applicability in different flow situations [254-257]. The enhanced wall treatment increases the validity of the near-wall modeling beyond the viscous sublayer. According to the ANSYS FLUENT manual, the modeled transport equations for the turbulent kinetic energy (k) and the rate of dissipation ( $\epsilon$ ) in the realizable k-epsilon (k- $\epsilon$ ) model can be expressed as:

$$\frac{\partial}{\partial t}(\rho k) + \frac{\partial}{\partial x_j}(\rho k u_j) = \frac{\partial}{\partial x_j} \left[ \left( \mu + \frac{\mu_t}{\sigma_k} \right) \frac{\partial k}{\partial x_j} \right] + G_k + G_b - \rho \epsilon - Y_M + S_k$$

and

$$\frac{\partial}{\partial t}(\rho \epsilon) + \frac{\partial}{\partial x_j}(\rho \epsilon u_j) = \frac{\partial}{\partial x_j} \left[ \left( \mu + \frac{\mu_t}{\sigma_\epsilon} \right) \frac{\partial \epsilon}{\partial x_j} \right] + \rho C_1 S \epsilon - \rho C_2 \frac{\epsilon^2}{k + \sqrt{\nu \epsilon}} + C_{1\epsilon} \frac{\epsilon}{k} C_{3\epsilon} G_b + S_\epsilon$$

where

$$C_1 = \max \left[ 0.43, \frac{\eta}{\eta + 5} \right], \quad \eta = S \frac{k}{\epsilon}, \quad S = \sqrt{2 S_{ij} S_{ij}}$$

In these equations,  $G_k$  is the generation of turbulent kinetic energy due to the mean velocity gradients,  $G_b$  is the generation of turbulent kinetic energy due to buoyancy,  $Y_M$  is the contribution of the fluctuating dilatation to the overall dissipation rate due to the compressibility of the fluid,  $C_2$ ,  $C_{1\epsilon}$  and  $C_{3\epsilon}$  are constants,  $\sigma_k$  and  $\sigma_\epsilon$  are the turbulent



Prandtl numbers for  $k$  and  $\epsilon$ , and  $S_k$  and  $S_\epsilon$  are user-defined source terms. The default values for the various model constants were used. The solver also used default settings.

### 3.3 Two Dimensional Analysis Results and Discussion

As mentioned before, the effects of five different shapes of roughness elements are investigated at different Reynolds numbers. The magnitude of the turbulence intensity is numerically determined for various relative height ( $e/h$ ) and pitch ratios ( $p/e$ ) for the five different shapes of roughness elements. The aim is to find out the optimum relative height ( $e/h$ ), pitch ratio ( $p/e$ ) and shape of the roughness elements, which would lead to a maximum enhancement of the turbulence intensity in the reactor channel and also an optimum localization of the turbulence intensity close to the catalyst surface. A similar channel with no roughness elements on the walls is also simulated for comparison. For the smooth channel, the magnitude of the turbulence intensity is equal to 8.30% and 15.74% for the Reynolds numbers 2900 and 5800, respectively.

#### 3.3.1 Flow Pattern and Square Shape of Roughness

Figure 3.4 shows the air flow on a smooth surface. Most of the air cannot come in contact with the surface. Figure 3.5 shows the flow pattern of the square roughness elements with the pitch ratios from 2 to 12. When the pitch ratio is less than 4 (d-type roughness), the outer flow is observed “riding” over the roughness elements with a separated recirculating region contained between each rib pair. On the other hand, when the pitch ratio is greater than four (k-type roughness), reattachment occurs between subsequent ribs. The results agree with those of references [235, 238].

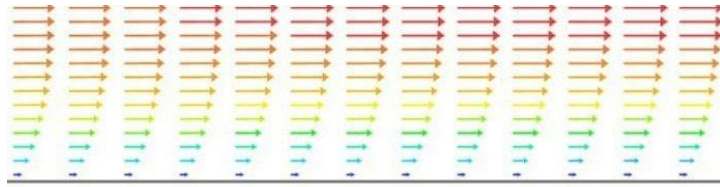


Figure 3.4 Air flow over a smooth surface

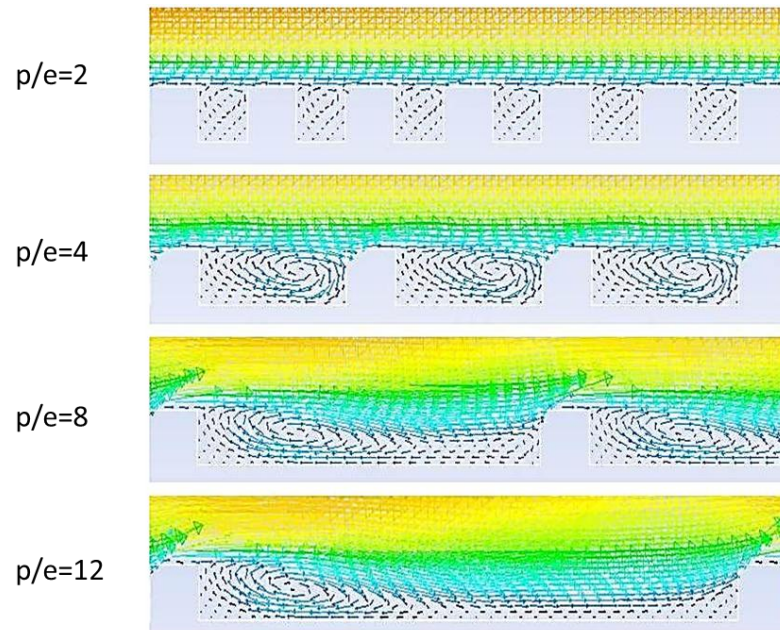


Figure 3.5 Flow patterns of square roughness elements with different pitch ratios

Different pitch ratios with different Reynolds numbers from 2900 to 8700 (average air flow rates from 1 to 3 m/s) are applied in the simulation of the channel with square roughness elements on the wall. The results are summarized in Figure 3.6. When the pitch ratio is equal to 10, the magnitude of the turbulence intensity reaches a maximum for all Reynolds numbers. Thus, the optimum pitch ratio would be 10 for any Reynolds number. In this study, Reynolds number of 2900 and 5800 (corresponding to average air flow rates of 1 and 2 m/s) are chosen for the photoreactor channel geometry optimization.

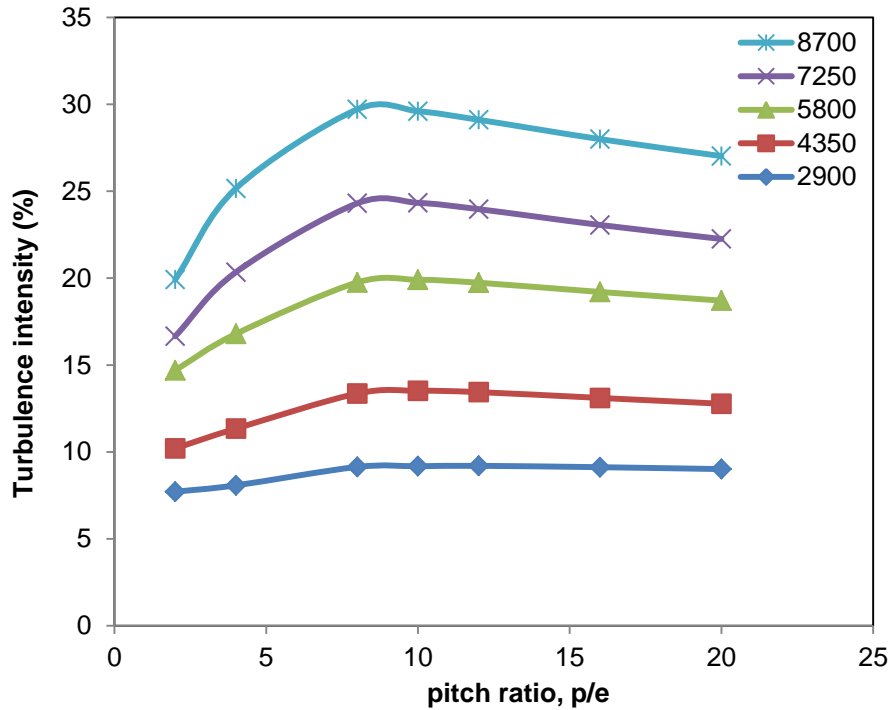


Figure 3.6 Effect of square roughness pitch ratio ( $p/e$ ) on turbulence intensity for  $Re$  from 2900 to 8700

### 3.3.2 Effect of Height of Roughness

In order to study the effect of the height of the roughness elements on the turbulence intensity in the channel, a rectangle is chosen as the representative shape of roughness. The ratio of roughness width to channel height ( $w/h$ ) is kept at 0.01 and the pitch ratio ( $p/e$ ) was kept at 10. The number of roughness elements is reduced with an increase in the height of roughness since the pitch ratio ( $p/e$ ) is kept at 10. Different heights of roughness ( $e/h$ ) from 0 to 0.2 were investigated. The height of roughness ( $e/h$ ) of 0 is corresponding to a smooth channel. The results are summarized in Figure 3.7.

Figure 3.7 shows that the turbulence intensity is almost constant for relative heights ( $e/h$ ) less than 0.01 and 0.02 for the Reynolds numbers of 5800 and 2900, respectively. This is due to the heights of the roughness elements being less than the flow

boundary sub-layer and do not affect the flow [258]. On the other hand, when the relative height ( $e/h$ ) is larger than 0.02, the magnitude of the turbulence intensity increases greatly with an increase in the height of the roughness. The flow boundary sub-layer has been calculated and equal to 0.022 and 0.037in for the Reynolds numbers of 5800 and 2900, respectively. However, for a photocatalytic reactor channel, an optimal height of the roughness would be one which led to the maximum enhancement in the turbulence intensity near the catalyst surface where the reaction occurs. Thus, it is important to not only enhance the turbulence intensity in the overall channel but also near the catalyst surface.

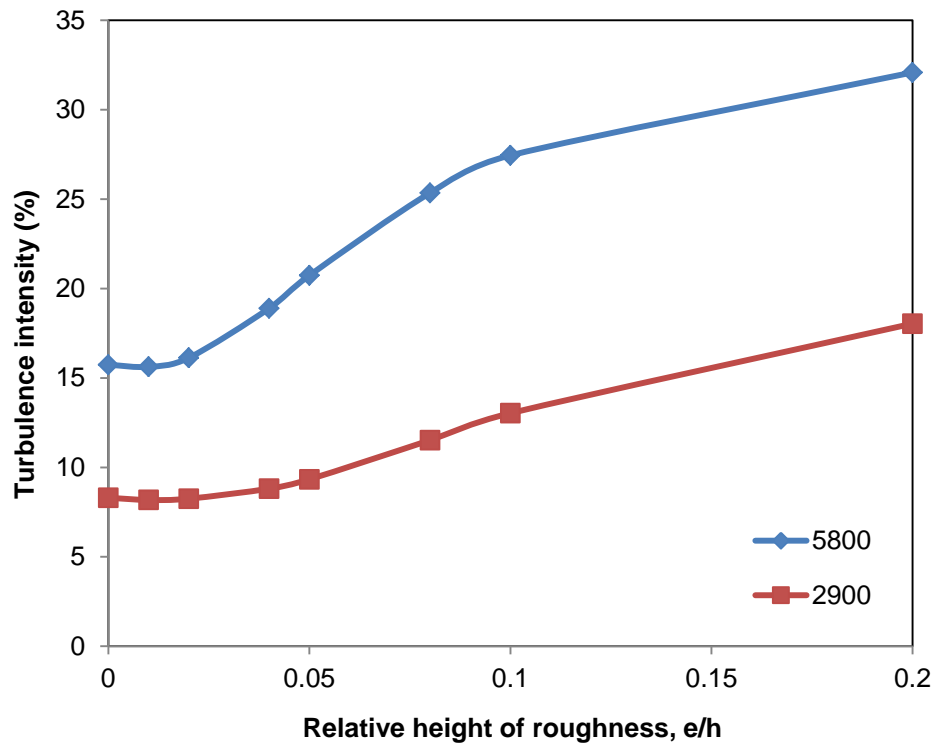


Figure 3.7 Effect of height of roughness (Re=2900, 5800)

Figure 3.8 plots the variation of the turbulence intensity with the distance from the surface for different roughness heights for a Reynolds number of 5800. It is clear that

even though an increase in the roughness element height leads to a great increase in the turbulence intensity in the channel, the turbulence intensity close to the catalyst surface ( $y/h < 0.1$ ) is reduced (Figure 3.8). This occurs because at higher values of relative roughness height, the reattachment of the free shear layer might not occur [259]. In photocatalysis, it is important to enhance the turbulence close to the catalyst surface, where the reaction is taking place. Assuming that  $y/h < 0.1$  is the space where there is significant impact to the mass transfer of the reactants to catalyst surface, from Figure 3.8, a relative height ( $e/h$ ) of 0.05 gives the highest turbulence intensity. Therefore, in this study, the optimum relative height of roughness ( $e/h$ ) is considered to be 0.05.

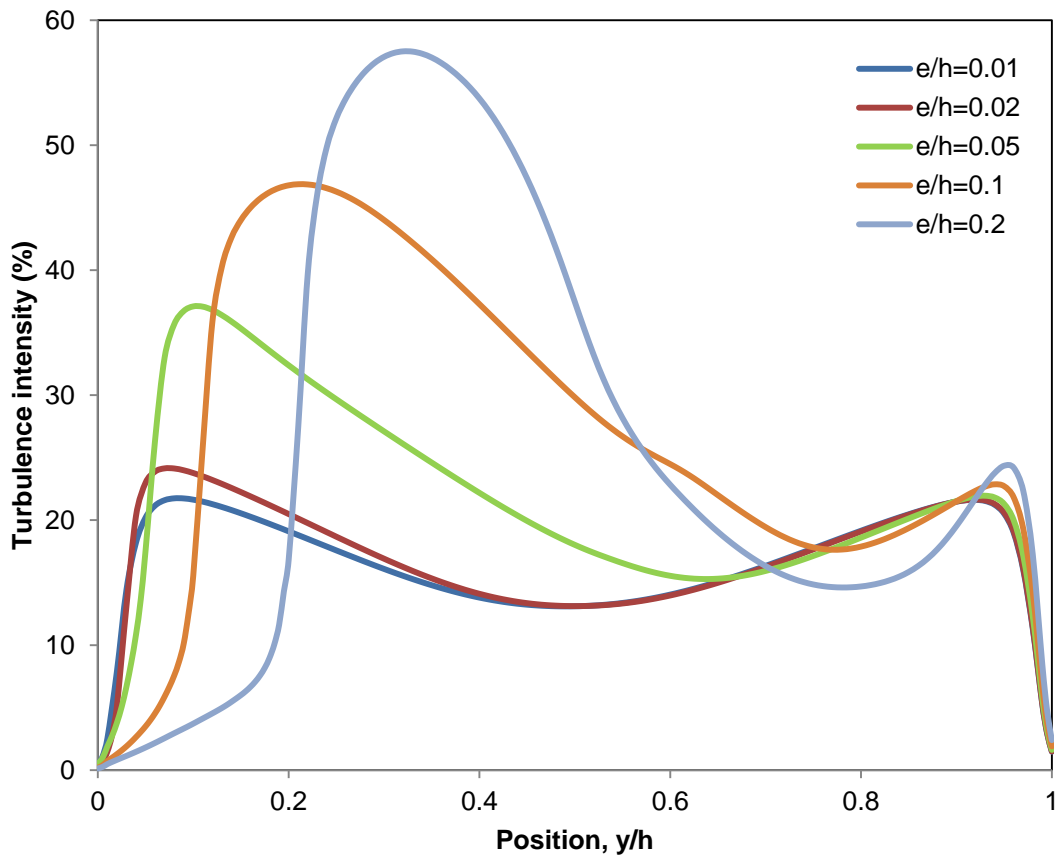


Figure 3.8 Plot of the magnitude of the average turbulence intensity in the Y-axis direction with different height of roughness (Re=5800)

### 3.3.3 Effect of Pitch Ratio ( $p/e$ ) and Shape of the Roughness Elements

Roughness pitch ratios ( $p/e$ ) from 2 to 20 are investigated to study the effect of pitch ratio along the flow direction on turbulence intensity. Also, different roughness shapes (square, isosceles triangle, semi-round, round, and chamfered shape) were introduced in the reactor channel (Figure 3.2) to find the best shape. The relative roughness height ( $e/h$ ) is kept at 0.05 for all shapes. For the isosceles triangle shape, the base angle (equal to the flow angle of attack)  $\alpha$  is kept as  $75^\circ$ . For the chamfered shape, the chamfer angle ( $\Phi$ ) is kept as  $45^\circ$  (Figure 3.9). The results are summarized in Figure 3.10 (a and b) for Reynolds numbers of 2900 and 5800, respectively.



Figure 3.9 Isosceles triangle and chamfer shape of roughness

It is evident that the turbulence intensity reaches a maximum for all shapes of roughness when the pitch ratio is equal to 10. Thus, the optimum pitch ratio would be 10 for all shapes of roughness. Among these shapes of roughness, the isosceles triangle shape produces the greatest turbulence intensity in the reactor channel, followed by the chamfered, square, round and semi-round shapes, respectively. Since the magnitude of the turbulence intensities is almost the same for the triangle and chamfered shapes of roughness elements, the optimum shape of roughness could be either triangle or chamfered. However, the isosceles triangle might be better since it produces less shade

than the chamfered shape when the light source is applied from the top of roughness elements.

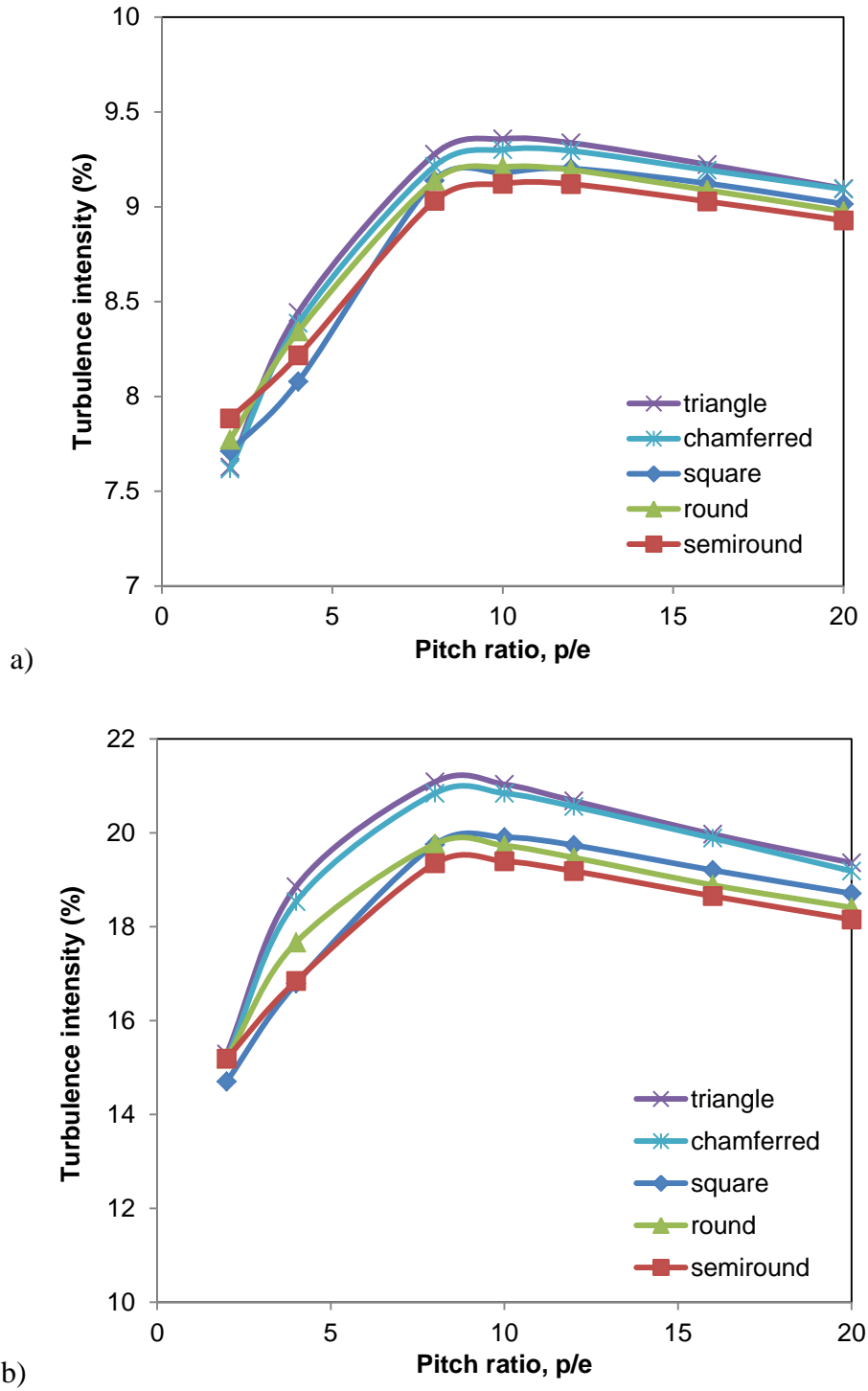
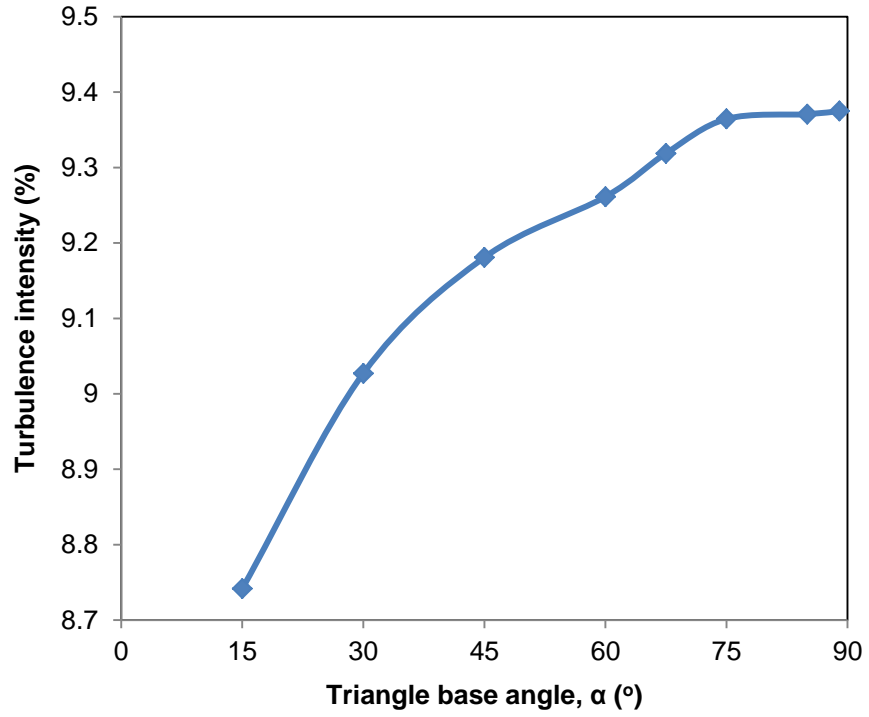
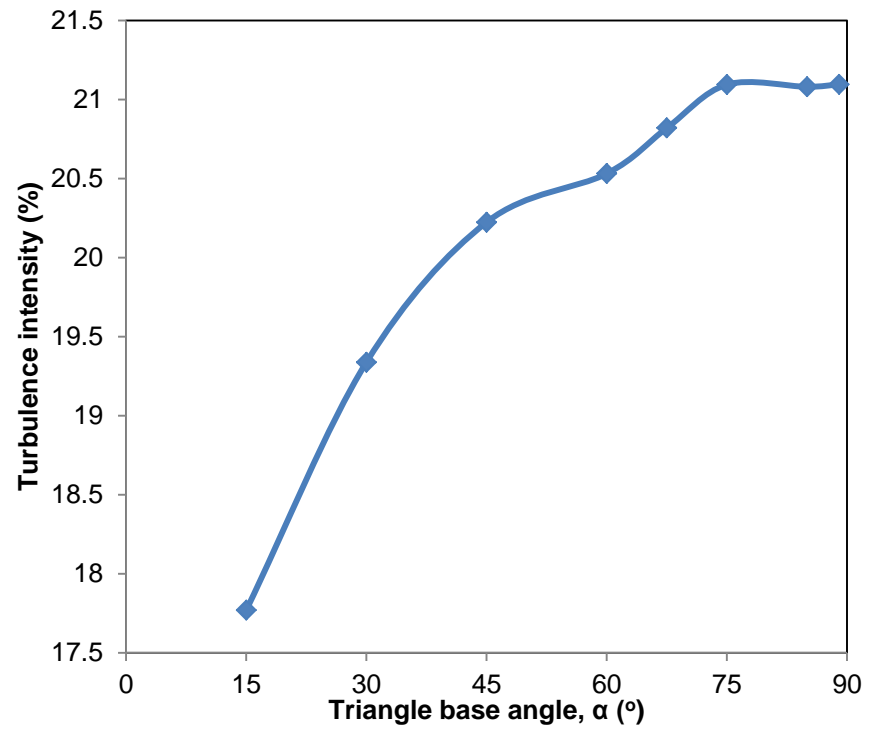


Figure 3.10 Comparison of the effect of different shapes of roughness in the channel. a)  $Re=2900$ ; b)  $Re=5800$



a)



b)

Figure 3.11 Effect of base angle of isosceles triangle shape roughness. a) Re=2900; b) Re=5800



The triangle and chamfered shapes of roughness, which are studied in Figure 3.10, are specific types in that the triangle base angle  $\alpha$  is equal to  $75^\circ$  and the chamfer angle  $\Phi$  is equal to  $45^\circ$ . The square roughness element in Figure 3.10 is also a specific type of rectangle. The above triangle, chamfered, and rectangle might not be the best shapes and further optimization studies may be required.

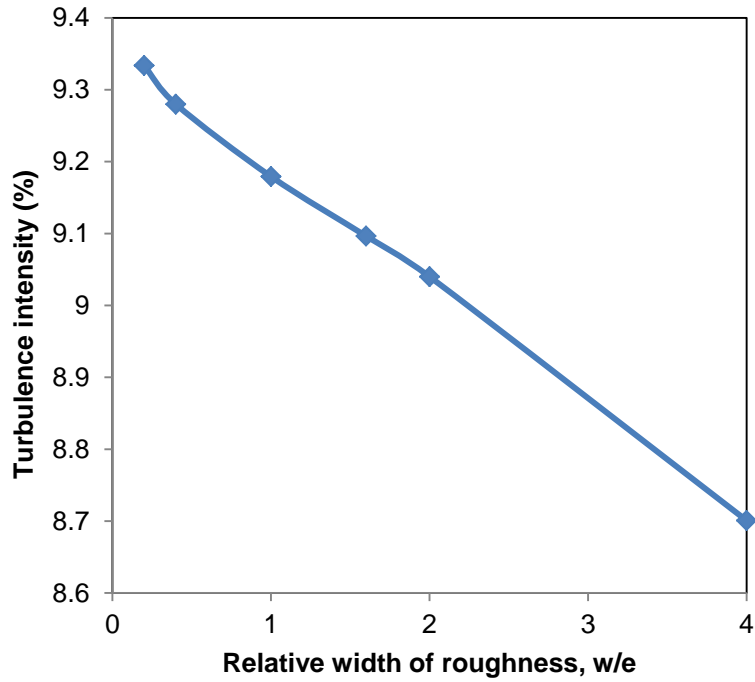
#### 3.3.4 Effect of Triangle Shape of Roughness

To optimize the triangle shape of roughness, the relative height ( $e/h$ ) is kept as 0.05 and the pitch ratio ( $p/e$ ) is kept as 10. Base angles (same as flow angle of attack)  $\alpha$  varying from  $15^\circ$  to  $89^\circ$  are investigated (Figure 3.9). The results are summarized in Figure 3.11 (a and b) for the flow Reynolds numbers of 2900 and 5800, respectively.

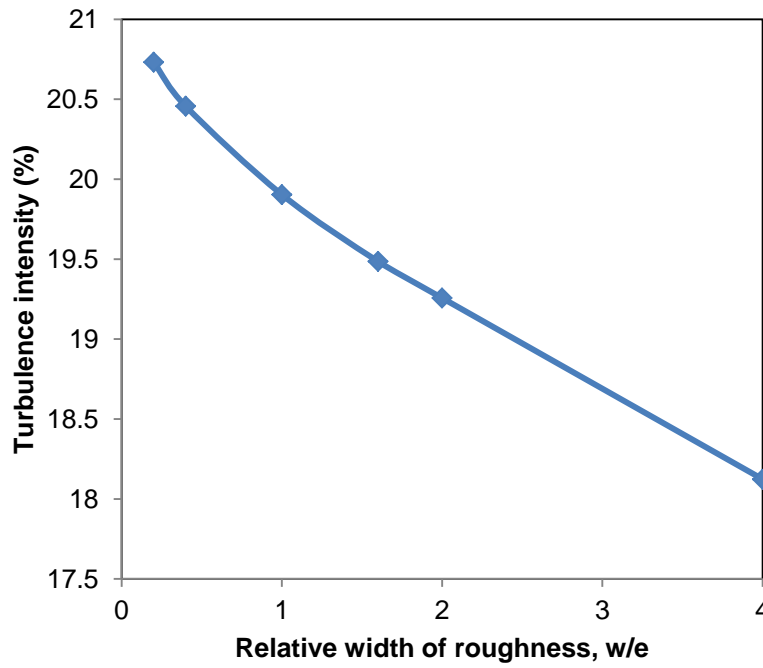
From Figure 3.11 (a and b), it can be seen that the magnitude of the turbulence intensity increases with the base angle ( $\alpha$ ) for both of the Reynolds numbers for base angles less than  $75^\circ$ . However, from  $75$  to  $89^\circ$ , the magnitude of the turbulence intensity is almost constant. Thus, the optimal isosceles triangle base angle ( $\alpha$ ) was chosen as  $75^\circ$  in this study. The magnitudes of the turbulence intensity for the optimum triangle shape of roughness (base angle equal to  $75^\circ$ ) are 9.36% and 21.09% for the Reynolds numbers of 2900 and 5800, respectively.

#### 3.3.5 Effect of Square Shape of Roughness

To optimize the rectangle shape of roughness, the relative height of roughness ( $e/h$ ) was kept as 0.05 and the pitch ratio ( $p/e$ ) was kept as 10. For the chosen height and pitch, different relative widths of roughness ( $w/e$ ) from 0.2 to 4 were investigated. The results were summarized in Figure 3.12 (a and b) for the Reynolds numbers of 2900 and 5800, respectively.



a)



b)

Figure 3.12 Effect of relative width ( $w/e$ ) on rectangle roughness. a)  $Re=2900$ ; b)  $Re=5800$

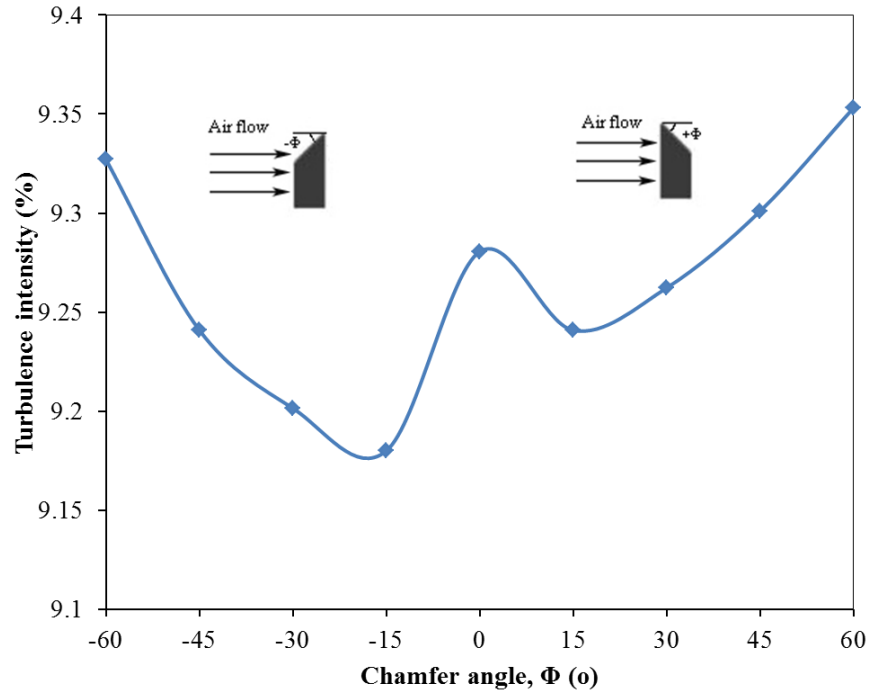
According to Figure 3.12 (a and b), the magnitude of turbulence intensity decreased when the roughness width increased for both Reynolds numbers 2900 and

5800. The results indicate that the roughness width should be kept as small as possible. The optimum roughness relative width is chosen as 0.02 in this study. The turbulence intensities are 9.33% and 20.73% corresponding to the Reynolds numbers of 2900 and 5800, respectively.

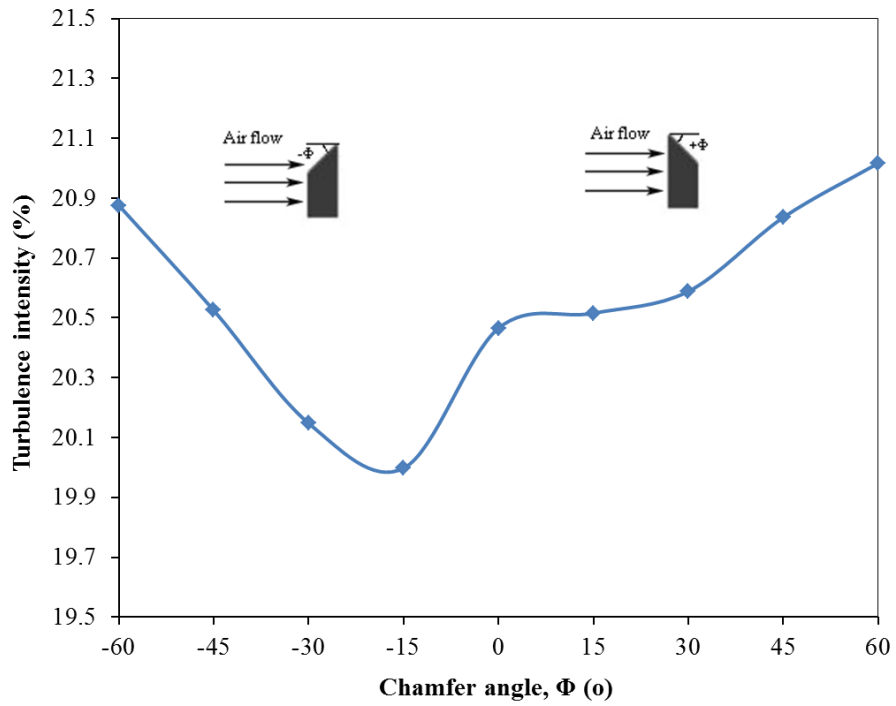
### 3.3.6 Effect of Chamfered Shape of Roughness

Similar to those mentioned above, the relative height of roughness ( $e/h$ ) is kept at 0.05, the pitch ratio ( $p/e$ ) is kept at 10, and the relative width of roughness ( $w/e$ ) is kept at 0.4. Different chamfer angles ( $\Phi$ ) from  $-60$  to  $60^\circ$  are investigated. The negative angles correspond to the flow attack at the chamfer side; the positive angles correspond to the flow attack at the back side of the chamfer, and the zero angles correspond to the rectangle roughness. The results are summarized in Figure 3.13 (a and b) for the flow Reynolds number of 2900 and 5800, respectively.

From Figure 3.13 (a and b), the magnitude of the turbulence intensity increased when the chamfer angle ( $\Phi$ ) is larger than the absolute value of  $15^\circ$ . The magnitude of the turbulence intensity may keep increasing when the absolute value of the chamfer angle is larger than  $60^\circ$ . However, as mentioned before, the roughness might be difficult to construct in a practical reactor if the zenith angle ( $\beta$ ) is too small since a larger chamfer angle ( $\Phi$ ) leads to a smaller zenith angle ( $\beta$ ). From Figure 3.13 (a and b), the magnitude of the turbulence intensity of flow attack at the back side of the chamfer ( $+\Phi$ ) is obviously larger than flow attack at the chamfer side ( $-\Phi$ ). Thus, the optimal chamfer angle ( $\Phi$ ) is chosen as  $60^\circ$  for the photoreactor channel in this study. The magnitudes of turbulence intensities for the optimum chamfer shape roughness ( $\Phi=60^\circ$ ) are 9.35% and 21.02% for the Reynolds numbers of 2900 and 5800, respectively.



a)



b)

Figure 3.13 Effect of flow angle of attack of chamfer shape roughness. a) Re=2900; b) Re=5800

Table 3.2 Summary of the optimal parameters for different shapes of roughness elements

	<b>Rectangle</b>	<b>Triangle</b>	<b>Round</b>	<b>Semiround</b>	<b>Chamfered</b>	<b>Smooth</b>
<b>Pitch ratio (p/e)</b>	10	10	10	10	10	----
<b>Relative height (e/h)</b>	0.05	0.05	0.05	0.05	0.05	0
<b>Relative width (w/e)</b>	0.2	----	----	----	----	----
<b>Zenith angle (<math>\beta</math>)</b>	----	30°	----	----	30°	----
<b>Turbulence intensity in optimal parameter (%)</b>	9.33 <sup>a</sup>	9.36 <sup>a</sup>	9.21 <sup>a</sup>	9.12 <sup>a</sup>	9.35 <sup>a</sup>	8.30 <sup>a</sup>
	20.73 <sup>b</sup>	21.09 <sup>b</sup>	19.73 <sup>b</sup>	19.39 <sup>b</sup>	21.02 <sup>b</sup>	15.74 <sup>b</sup>
<b>Others</b>	Smaller width is better	Larger base angle or smaller zenith angle is better	----	----	Positive chamfer angle with smaller zenith angle is better	----

Note: <sup>a</sup> Re equal to 2900; <sup>b</sup> Re equal to 5800.

Table 3.2 summarizes the optimal parameters for different shapes of roughness. When the chamfer angle ( $\Phi$ ) is increased, the zenith angle ( $\beta$ ) of the chamfered shape is decreased (Figure 3.9). This means the magnitude of the turbulence intensity is increased when the zenith angle ( $\beta$ ) of the chamfer is decreased. This result is quite similar with the triangle shape of roughness. From the results of these shapes of roughness elements, we may conclude that, in general, under similar conditions, the roughness elements with a smaller top width (or zenith) are always better for increasing the turbulence intensity in the channel independent of the shape. This rule could be used to choose the shape of the roughness element for enhancing the magnitude of turbulence intensity in a photoreactor duct.

From Table 3.2, we can also see that the magnitude of the turbulence intensity for the optimal isosceles triangle shape is slightly larger than the optimal chamfered shape. Also, as mentioned before, the isosceles triangle produces less shade than the chamfered shape roughness when the light source is positioned above the roughness elements. Thus, the isosceles triangle with the base angle ( $\alpha$ ) equal to  $75^\circ$  (or  $\beta=30^\circ$ ) is considered to be the best shape to maximize the turbulence intensity in the photocatalytic reactor channel.

### **3.4 Three Dimensional Analysis of Turbulence Intensity with Roughness Patterns**

In the three-dimensional (3D) study, the investigated surface roughness arrangements include transverse ribs, inclined ribs, V shape ribs, and mesh. The possibility of using a two-dimensional (2D) solution domain was ruled out because of the chosen roughness elements, such as the inclined rib and mesh roughness arrangements. Thus, a three-dimensional (3D) air flow passage was used in these studies.

### 3.4.1 Details of the 3D Photoreactor Passage Geometry

The photocatalytic reactor passage was assumed the same as that in the 2D study that is a rectangular duct with a cross-section of  $2.54 \times 12.7 \text{ cm}$  ( $1 \times 5 \text{ in}$ ,  $H \times W$ ), and length ( $L$ ) of  $63.5 \text{ cm}$  ( $25 \text{ in}$ ). The passage was divided into three parts: inlet section, test section, and outlet section (Figure 3.14). The inlet and outlet sections were smooth ducts, to reduce the end effects of the test section. The lengths of the inlet, test, and outlet sections were  $25.4$ ,  $25.4$ , and  $12.7 \text{ cm}$  ( $10$ ,  $10$ , and  $5 \text{ in}$ ), respectively. The height of the photoreactor passage was  $2.54 \text{ cm}$  ( $1 \text{ in}$ ). The roughness elements were introduced on the bottom surface of the test section, as shown in Figure 3.14.

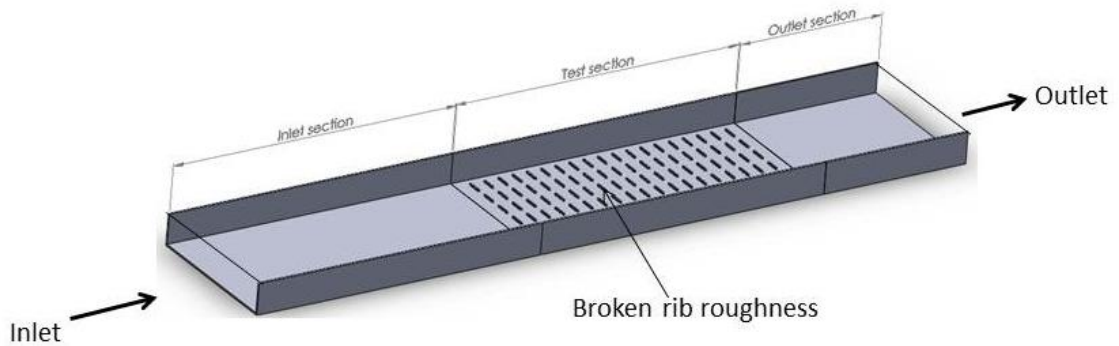


Figure 3.14 Photoreactor passage with transverse broken rib roughness elements on the bottom wall of the test section

### 3.4.2 Roughness Arrangements and Range of Parameters

Both isosceles triangle and square cross section rib roughness have been used as representative roughness elements (Figure 3.15). The base angle of the isosceles triangle roughness element was fixed at  $75^\circ$ . The investigated surface roughness arrangements include transverse continuous ribs, transverse broken ribs, inclined continuous ribs, inclined broken ribs, V shape continuous ribs, V shape broken ribs, and meshed for a fixed relative pitch ( $p/e$ ) of  $10$  and relative height ( $e/h$ ) of  $0.05$  (Figure 3.16). The

investigation also includes flow angles of attack ( $\alpha$ ) from 30 to 90° and Reynolds numbers (Re) ranging from 2900 to 5800 for all surface roughness arrangements except for the transverse roughness arrangement ( $\alpha$  equal to 90°).

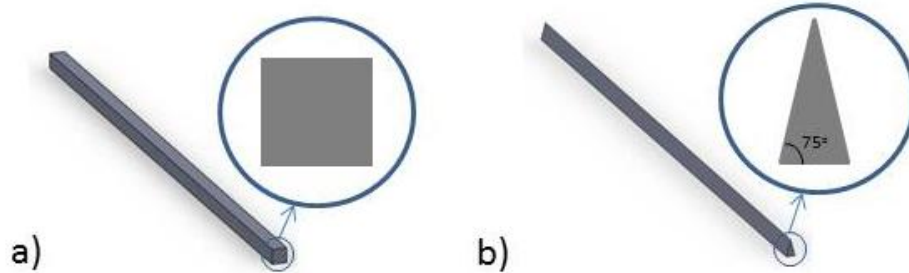


Figure 3.15 The representative shape of rib roughness. a) square cross section; b) isosceles triangle cross section

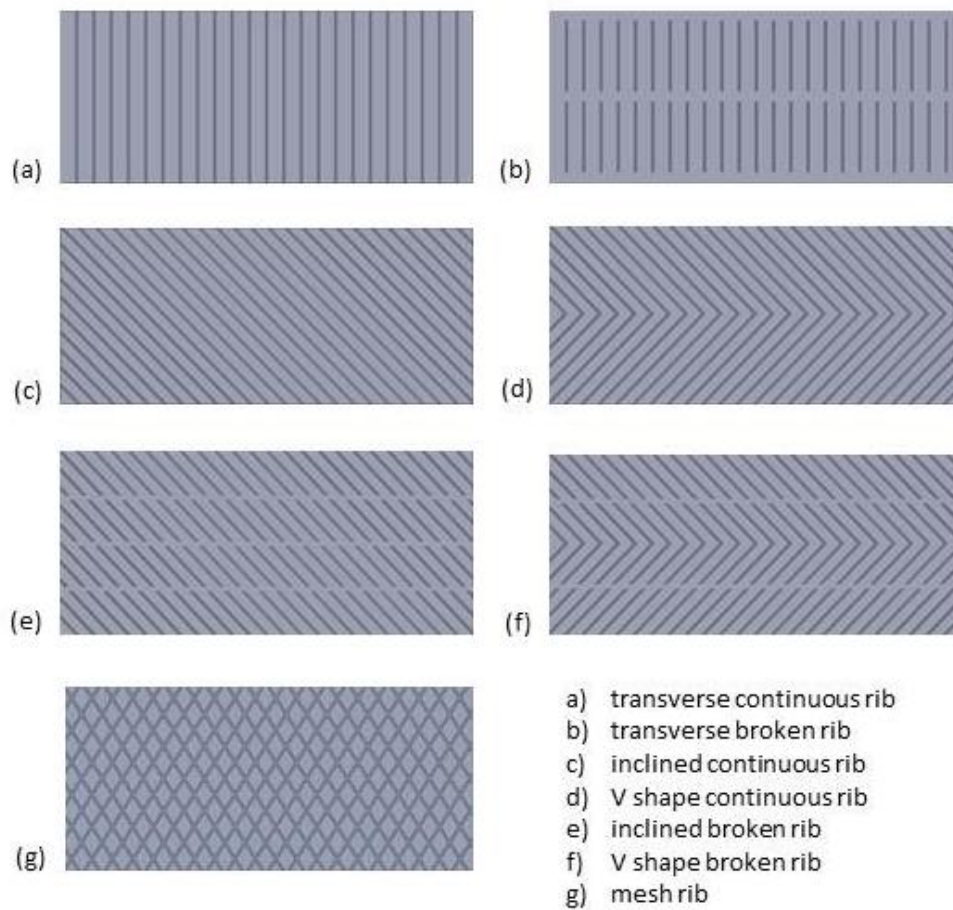


Figure 3.16 Different surface roughness elements arrangements



### 3.4.3 Mesh

For the 3D study, meshing has been done using the commercially available software Ansys Mesh 13.0. The non-uniform mesh was applied close to the rough surface with mesh adaption for  $y^+ < 3$ . The number of cells in each set of geometry varied from 1.5 to 2.5 million depending on the cross section of the rib roughness elements and the flow angle of attack ( $\alpha$ ). To ensure that the results were mesh independent and well resolved, the simulations were repeated with finer levels of meshing. It was found that there are no noticeable differences in the solutions.

### 3.4.4 CFD Analysis

A 3D analysis of air flow through the rectangular duct with various roughness element arrangements on a broad wall was carried out using the commercially available CFD software Ansys Fluent 13.0. The following assumptions were made in the mathematical model: a) The flow is steady, fully developed, and turbulent; and b) the working fluid, air, is incompressible for the operation. The Velocity-inlet has been used as the inlet boundary condition and The Pressure-outlet as the outlet boundary condition. The Reynolds number (Re) varied from 2900 to 5800. The corresponding range of the average air flow rate varied from 1 to 2 m/s as calculated from the Reynolds numbers. The outlet pressure of the outlet boundary condition was set equal to the atmospheric pressure, and no slip wall boundary conditions are used for the analysis. The second order upwind numerical scheme and SIMPLE algorithm were used to discretize the governing equations. A residual value equal to  $10^{-5}$  was applied for the resulting calculation convergence. The magnitude of the turbulence intensity in the test section was studied to find out how the roughness arrangements affect the air flow properties. In order to save

computer memory and computational time, the inlet section was simulated separately. The outlet velocity profile of the inlet section was used as the velocity inlet boundary condition of the test section.

#### 3.4.5 Numerical Modeling

The “realizable k-epsilon (k- $\epsilon$ )” model with Enhanced Wall Treatment was used for the solution of the turbulent momentum equations. The k-epsilon (k- $\epsilon$ ) model was chosen because of its simplicity, reasonable accuracy, and wide applicability under different flow situations [254-257]. The enhanced wall treatment increases the validity of the near-wall modeling beyond the viscous sublayer.

### 3.5 Three Dimensional Analysis Results and Discussions

As mentioned before, the effect of different roughness element arrangements on the bottom wall of the photocatalytic reactor duct are investigated in the range of Reynolds numbers from 2900 to 5800. Both the isosceles triangle and the square cross section ribs are used as representative shapes of roughness. The investigated surface roughness arrangements included transverse continuous ribs, transverse broken ribs, inclined continuous ribs, inclined broken ribs, V shape continuous ribs, V shape broken ribs, and mesh for a fixed relative pitch ( $p/e$ ) of 10 and relative height ( $e/h$ ) of 0.05. The magnitude of the turbulence intensity is numerically determined for various surface roughness arrangements. The aim is to compare the effect of various surface roughness arrangements in air flow and find out the optimum surface roughness arrangement, which would lead to maximum enhanced the magnitude of turbulence intensity in the reactor channel.

### 3.5.1 Effect of Transverse Broken Rib

The relative length of the rib ( $l/e$ ) and the relative gap of the rib ( $g/e$ ) are two of the most important parameters for the transverse broken ribs. The 'l' is the length of the rib and 'g' is the gap between two broken ribs (Figure 3.17). The flow angle of attack ( $\alpha$ ) is  $90^\circ$  for the transverse broken ribs.

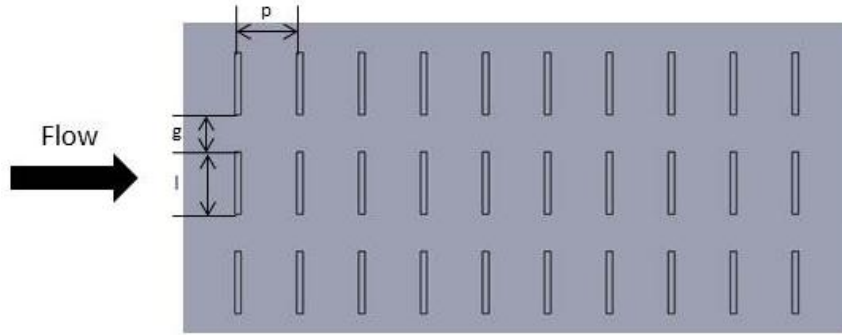


Figure 3.17 Transverse broken rib roughnesses

Table 3.3 summarizes the studied parameters of the transverse broken rib roughness. In the first study, the relative gap of the ribs ( $g/e$ ) is kept as 1, and the relative length of the ribs ( $l/e$ ) is varied from 0 to 48. The relative length of the rib ( $l/e$ ) equal to 0 corresponds to a smooth duct. Because the length of the rib roughness is changed and the width of the plate is kept constant, the number of ribs ( $n$ ) in flow vertical direction is also changed from 2 to 50 ribs. Figure 3.18 summarizes the results of study No. 1.

Table 3.3 The parameters of transverse broken rib roughness

Study	Cross section of rib	Relative gap of ribs ( $g/e$ )	Relative length of rib ( $l/e$ )	Number of ribs ( $n$ )	Reynolds number (Re)
1	■ ▲	1	0~48	2~50	2900~5800
2	■ ▲	0~16	10	3~9	2900~5800

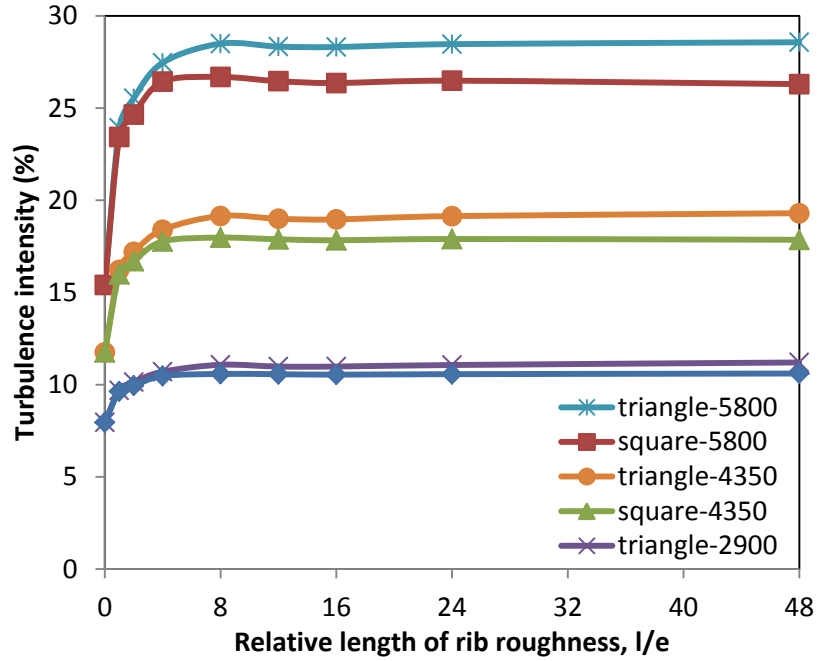


Figure 3.18 Effect of transverse broken rib with the relative gap ( $g/e$ ) kept as 1 (rib cross section: triangle, square;  $Re=2900, 4350, 5800$ )

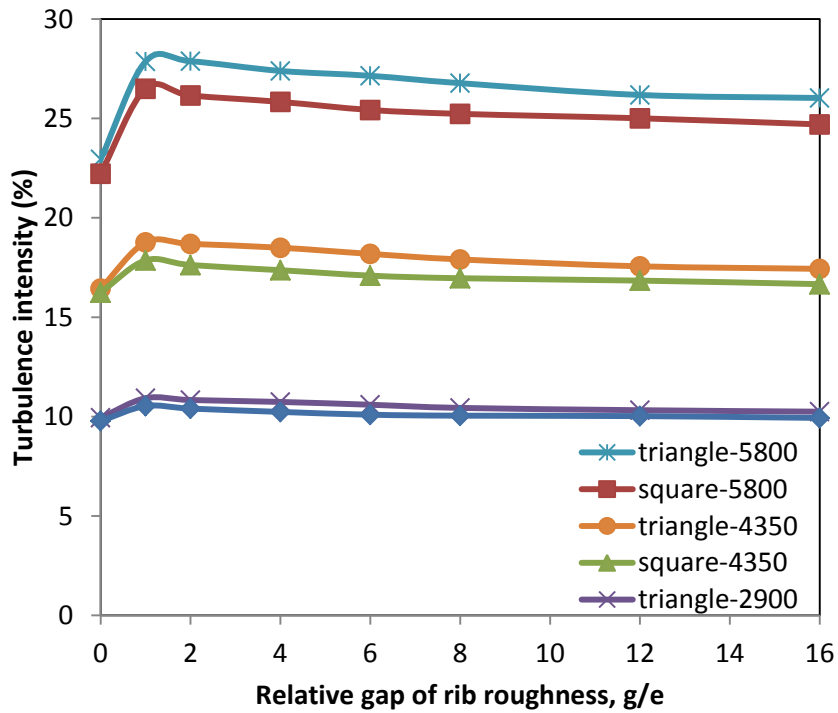


Figure 3.19 Effect of transverse broken rib with the relative length of roughness ( $l/e$ ) kept as 10 (Cross section of rib: triangle, square;  $Re=2900, 4350, 5800$ )

Figure 3.18 shows that the magnitude of the turbulence intensity in the test section is increased when the relative length of rib roughness ( $l/e$ ) increases from 0 to 8 for all cases. However, it is almost constant for  $l/e$  is larger than 8 under similar conditions.

From Figure 3.18, a triangle cross section of rib roughness always produces more turbulence than the square cross section under similar conditions. Comparison of different Reynolds numbers shows that the enhancement in the magnitude of the turbulence intensity for larger Reynolds numbers is much greater than for lower Reynolds numbers. In addition, the magnitude of the turbulence intensity is more sensitive with the shape of roughness for higher Reynolds numbers. Under similar conditions, the magnitude of the turbulence intensity is enhanced for all cases of transverse broken rib arrangements as compared to the transverse continuous rib. Thus, we may conclude that a transverse broken arrangement is more effective than a transverse continuous arrangement in increasing the magnitude of the turbulence intensity. The optimal relative length of the transverse broken rib ( $l/e$ ) would be 8~48. In our study, the results are not different if the transverse rib is broken into 2 ribs or 10 ribs.

For the study No.2 in Table 3.3, the relative length of rib roughness ( $l/e$ ) is kept at 10, and the relative gap of roughness ( $g/e$ ) is varied from 0 to 16. A relative gap of the rib ( $g/e$ ) equal to 0 corresponds to a continuous transverse rib. Because the relative gap of the rib ( $g/e$ ) is changed and the width of the channel is kept constant, the number of transverse ribs ( $n$ ) is changed from 3 to 9. Figure 3.19 summarizes the results of the study No. 2.

It is clear that the magnitude of the turbulence intensity in the test section reaches a maximum when the relative gap of rib roughness ( $g/e$ ) is equal to 1 for all studied cases.

Thus, the optimal relative gap of the transverse broken rib ( $g/e$ ) would be 1. Figure 3.19 also shows some results similar to study No.1, indicating that, the triangle cross section ribs produce more turbulence than the square cross section ribs under similar conditions. A comparison of different Reynolds numbers shows that the enhancement of the magnitude of the turbulence intensity is greater with higher Reynolds numbers.

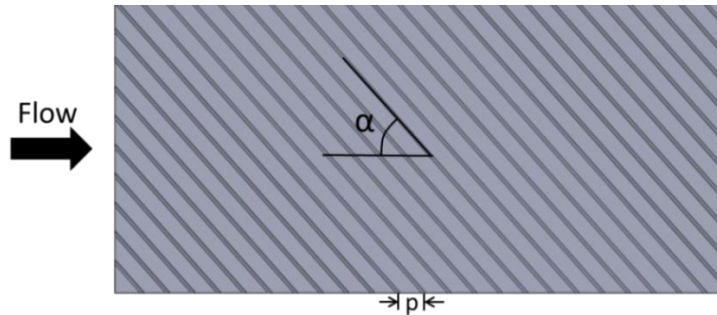


Figure 3.20 Studies of inclined continuous rib roughness sheet

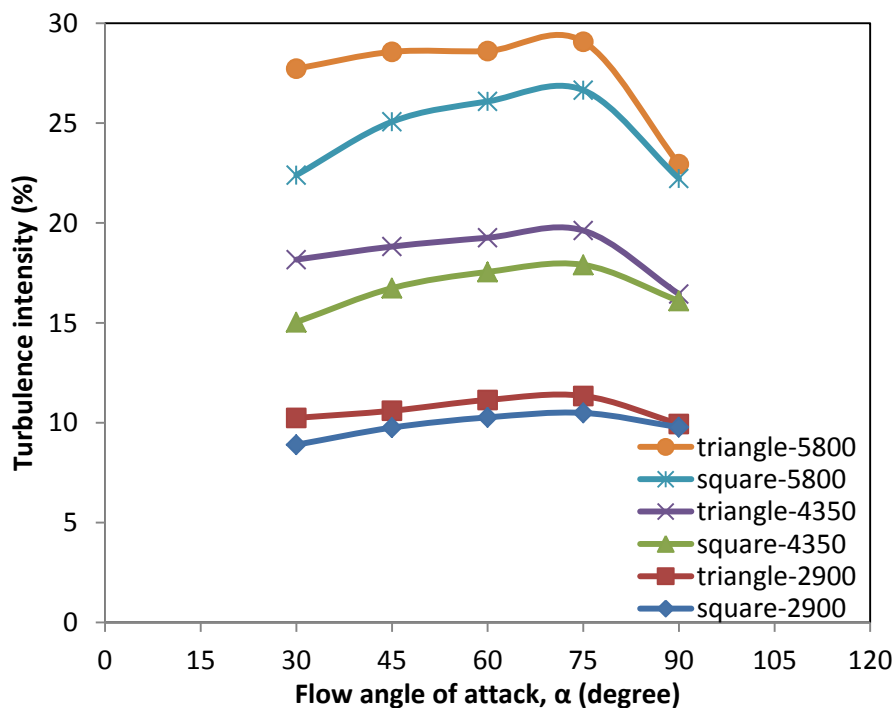


Figure 3.21 Effect of inclined continuous rib roughness (Cross section of rib: triangle, square;  $Re=2900, 4350, 5800$ )

### 3.5.2 Effect of Inclined Continuous Rib

To study the effect of an inclined continuous rib roughness in the channel, triangle and square cross section rib roughness are used as the representative shapes of roughness. The relative pitch ( $p/e$ ) and the relative height ( $e/h$ ) of roughness are kept as 10 and 0.05, respectively. The ribs are inclined at different angles to the flow direction, thus, the flow angle of attack ( $\alpha$ ) of the ribs is changed from 30 to 90° (Figure 3.20). The flow angle of attack ( $\alpha$ ) equal to 90° corresponds to a transverse continuous rib. The results are summarized in Figure 3.21.

Figure 3.21 shows that the magnitude of the turbulence intensity in the test section reaches a maximum when the flow angle of attack ( $\alpha$ ) is equal to 75° for all the cases. Thus, the optimum inclined continuous rib flow angle of attack ( $\alpha$ ) would be 75°.

### 3.5.3 Effect of Inclined Broken Rib

Since the optimal parameters of the relative gap ( $g/e$ ) and relative length ( $l/e$ ) are already found out from the study of the transverse broken ribs, these values could be used for the inclined broken ribs. Therefore, to study the effect of inclined broken ribs, the relative gap ( $g/e$ ) is kept as 1 and the transverse relative length ( $l/e$ ) is kept as 24. Thus, in this case, one full transverse rib is broken into 4 smaller ribs. The ribs are inclined at different angles to the flow direction and the flow angle of attack ( $\alpha$ ) of the rib is changed from 30 to 90° (Figure 3.22). The flow angle of attack ( $\alpha$ ) equal to 90° corresponds to the transverse broken rib. The results are summarized in Figure 3.23.

Figure 3.23 shows that the magnitude of the turbulence intensity is maximum when the flow angle of attack ( $\alpha$ ) is equal to 75° for all cases. However, this is very close to the value obtained with the flow angle of attack ( $\alpha$ ) of 90°. Thus, the optimum flow

angle of attack ( $\alpha$ ) for inclined broken ribs could be either 75 or 90° (transverse broken rib). The transverse broken ribs may be a better choice for a photocatalytic reactor duct since it seems easier to construct than the inclined broken rib arrangement.

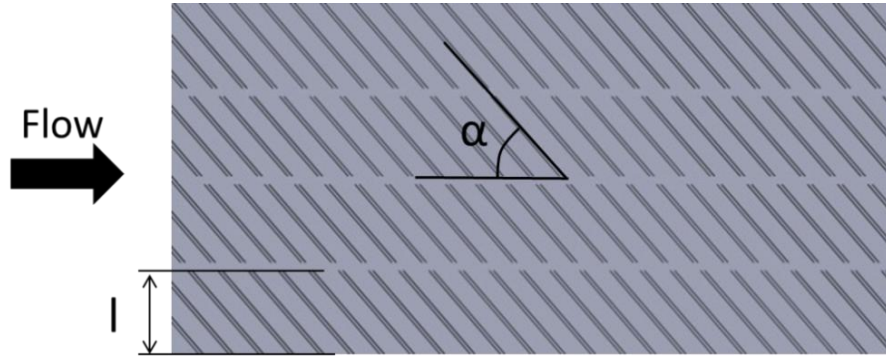


Figure 3.22 Studied of inclined broken rib roughness sheet

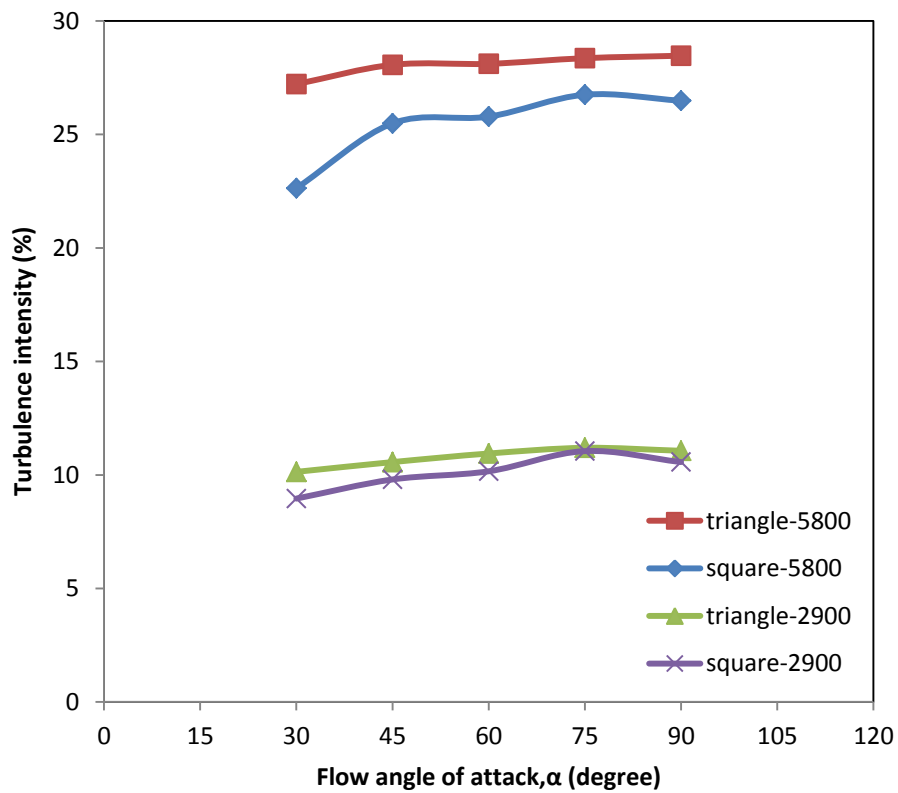


Figure 3.23 Effect of inclined broken rib (Cross section of rib: triangle, square; Re=2900, 5800)



### 3.5.4 Effect of V Shape Continuous Rib

The triangle and square cross section of rib roughness are used as representative shapes of roughness in the study of the effect of the V shape continuous rib roughness. The relative pitch ( $p/e$ ) and relative height ( $e/h$ ) of roughness are kept as 10 and 0.05, respectively. The flow angle of attack ( $\alpha$ ) for the ribs from 30 to 90° is considered. The 90° angle corresponds to a transverse continuous rib. The results are summarized in Figure 3.24.

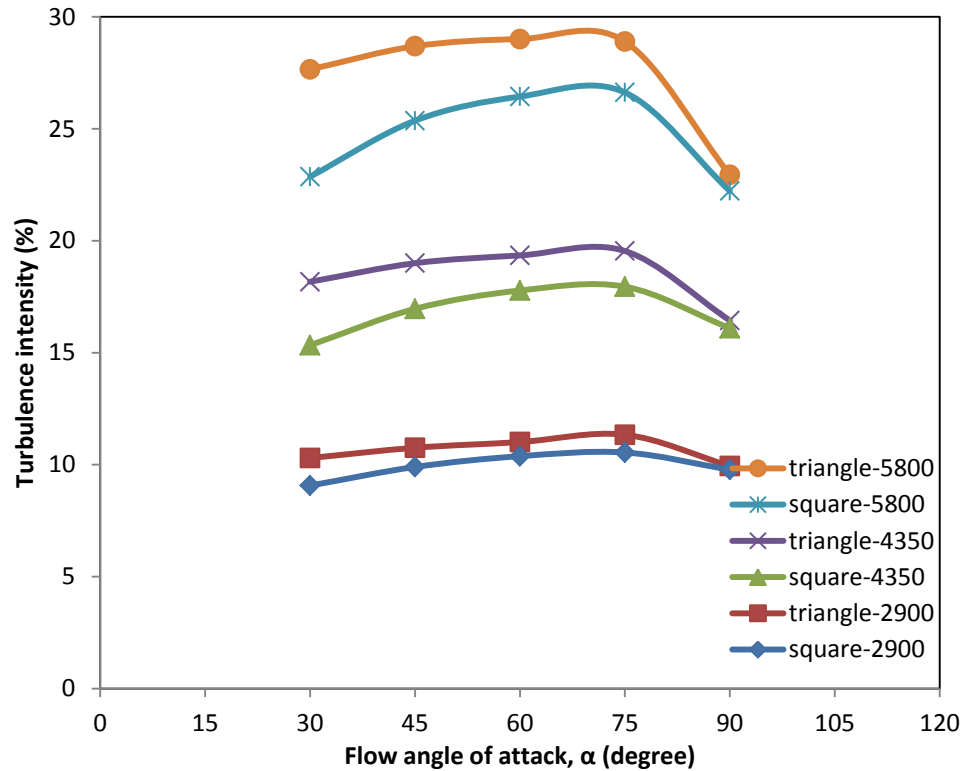


Figure 3.24 Effect of V shape continuous rib (Cross section of rib: triangle, square; Re=2900, 4350, 5800)

Figure 3.24 shows that the magnitude of the turbulence intensity reaches a maximum when the flow angle of attack ( $\alpha$ ) is equal to 75° for all cases. Thus, the optimal V shape continuous rib flow angle of attack ( $\alpha$ ) would be 75°. The results are

similar to the inclined continuous rib, where the optimal flow angle of attack ( $\alpha$ ) is also  $75^\circ$ .

### 3.5.5 Effect of V Shape Broken Rib

To study the effect of V shape broken rib, the relative gap ( $g/e$ ) is kept as 1 and the transverse relative length ( $l/e$ ) is kept as 24. The V shape rib is divided into three parts: one smaller V shape rib between two inclined ribs (Figure 3.25). The flow angle of attack ( $\alpha$ ) is varied from  $30^\circ$  to  $90^\circ$ . The  $90^\circ$  corresponds to the transverse broken rib. Other parameters are similar to those studied previously. The results are summarized in Figure 3.26.

Figure 3.26 shows that the maxima of the magnitudes of the turbulence intensity are different in different cases. However, when these maximum values are compared at the  $90^\circ$  flow angle of attack ( $\alpha$ ), the differences are very small.

### 3.5.6 Effect of Mesh Rib

Using conditions as mentioned above, the effect of mesh rib roughness was studied. The relative pitch ( $p/e$ ) and relative height ( $e/h$ ) of roughness are kept at 10 and 0.05, respectively. The flow angle of attack ( $\alpha$ ) for the mesh rib varied from  $30^\circ$  to  $90^\circ$  (Figure 3.27). The results are summarized in Figure 3.28.

Figure 3.28 shows that the maximum magnitude of the turbulence intensity occurs at a flow angle of attack ( $\alpha$ ) equal to  $60^\circ$  for a triangle cross section and is equal to  $75^\circ$  for a square cross section of mesh roughness. Thus, the optimum flow angle of attack ( $\alpha$ ) for the mesh rib plate would be  $60^\circ$  to  $75^\circ$  depending on the cross section of the rib roughness.

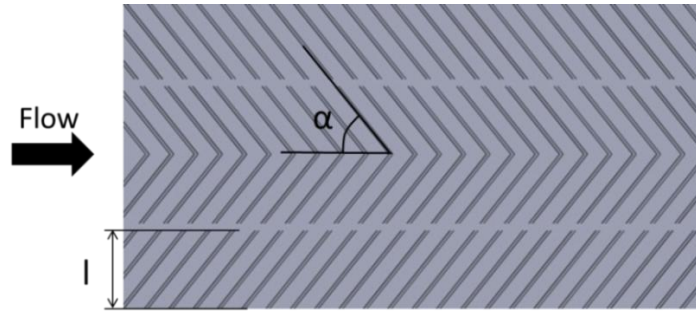


Figure 3.25 V shape broken rib roughness sheet

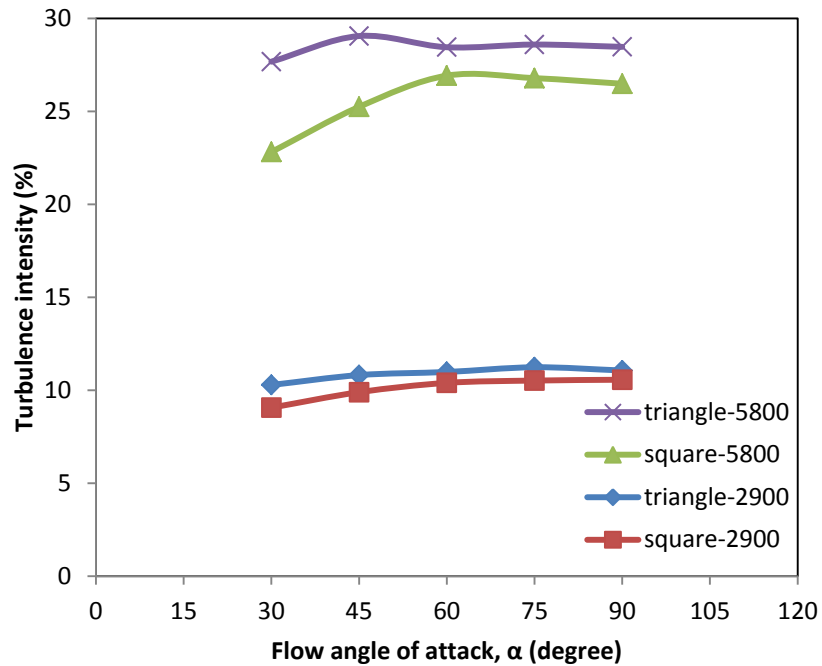


Figure 3.26 Effect of flow angle of attack on turbulence intensity for V shape broken ribs (Cross section of rib: triangle, square; Re=2900, 5800)

### 3.5.7 Comparison of Different Roughness Elements

Figure 3.29 compares the effect of the flow angle of attack on the turbulence intensity for continuous inclined, continuous V shape and mesh ribs at a Reynolds number of 5800 for a square shape roughness. It is clear that the magnitude of the turbulence intensity reaches a maximum when the flow angle of attack ( $\alpha$ ) is about  $75^\circ$  for all arrangements. For the incline and V shape rib plates, only a slight difference exists

between them. Thus, the choice of incline or V shape roughness depends on the cost of the construction. The effect of the mesh rib roughness arrangement is close to the incline and V shape ribs for a flow angle of attack ( $\alpha$ ) less than  $75^\circ$ . However, when the mesh at a flow angle of attack ( $\alpha$ ) equal to  $90^\circ$ , the turbulence is considerably larger as compared to the inclined and V shape rib roughness.

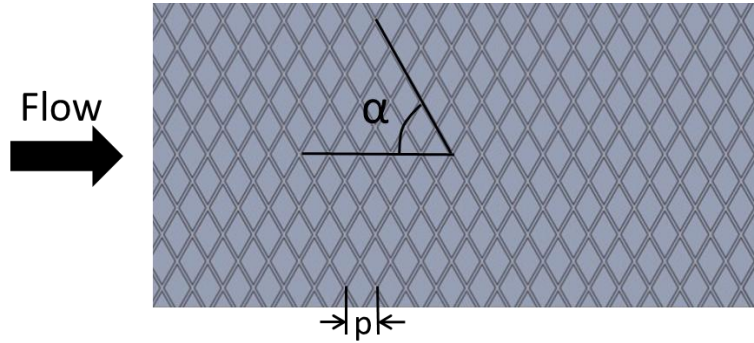


Figure 3.27 Mesh rib roughness sheet

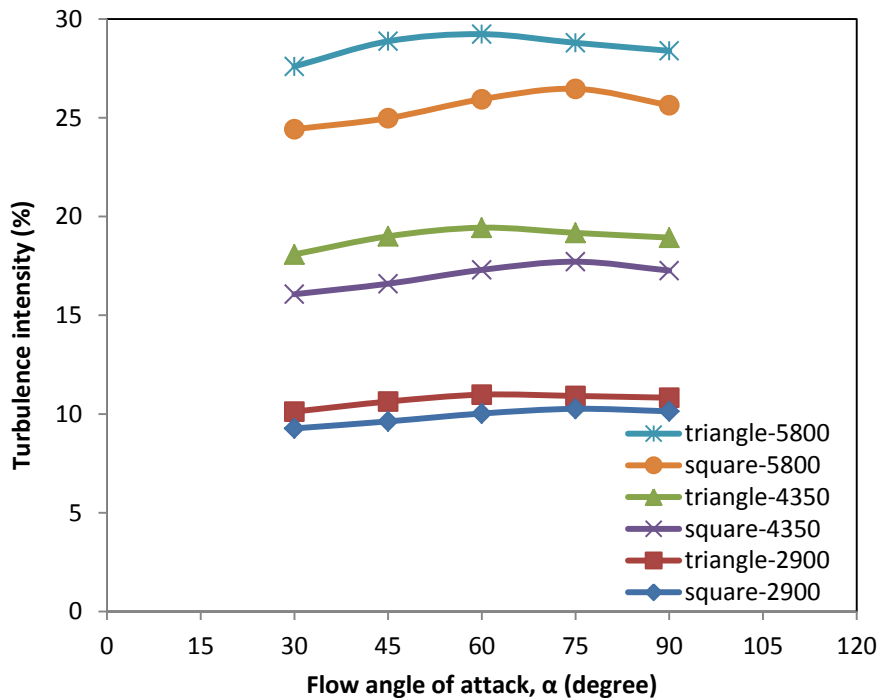


Figure 3.28 Effect of flow angle of attack on the turbulence intensity for a mesh rib plate (Cross section of rib: triangle, square;  $Re=2900, 4350, 5800$ )

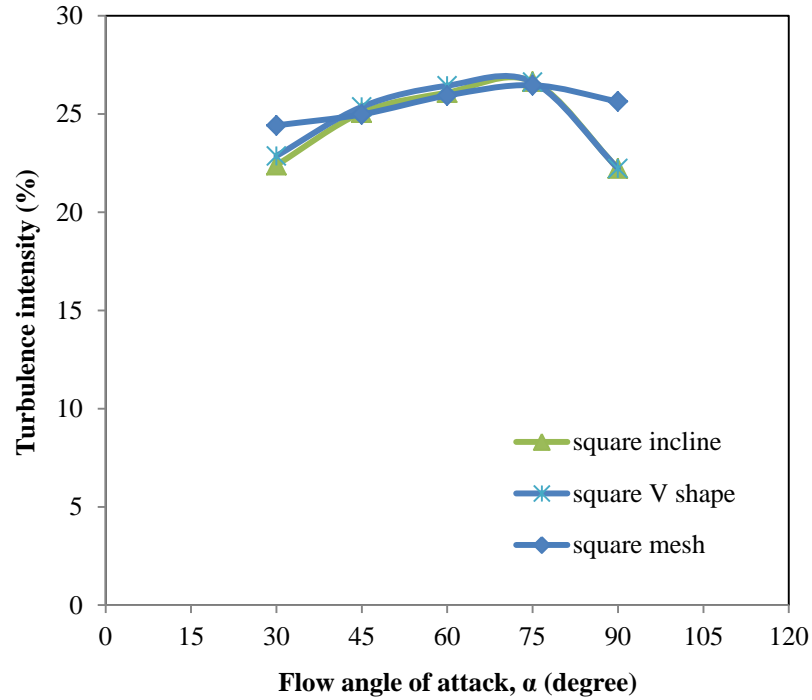


Figure 3.29 Comparison of the effect of flow angle of attack on the turbulence intensity for inclined, V shape and mesh of rib roughness (Cross section of rib: square;  $Re=5800$ )

Table 3.4 summarizes the optimum parameters of the studied roughness element arrangements and the magnitude of the turbulence intensity under optimal parameters. Compared to a smooth channel, the transverse continuous rib roughness arrangement increases the turbulence intensity in the channel. The turbulence intensity for the inclined and V shape continuous arrangements are greater than the transverse continuous arrangement for all cases. The difference between the optimal incline and V shape continuous arrangements is so small that it could be ignored. The magnitude of the turbulence intensity for the mesh arrangement is also greater than the transverse arrangement but slightly less than the incline or V shape arrangements, in most cases. Thus, we conclude the order of performance for continuous rib roughness arrangements is: V shape  $\approx$  inclined > mesh > transverse > smooth.

Table 3.4 Summary of the optimum parameters for different roughness arrangements

	Continuous rib roughness					Broken rib roughness		
	Smooth	Transverse	Inclined	V shape	Mesh	Transverse	Inclined	V shape
Pitch ratio (p/e)	----	10	10	10	10	10	10	10
Relative height (e/h)	----	0.05	0.05	0.05	0.05	0.05	0.05	0.05
Relative gap (g/e)	----	0	----	----	----	1	1	1
Relative length (l/e)	----	----	----	----	----	8~48	8~48	8~48
Flow angle of angle ( $\alpha$ )	----	----	75°	75°	60~75°	----	75°	45~90°
Turbulence intensity (Re=2900)	7.95%	9.78% <sup>a</sup> 9.94% <sup>b</sup>	10.49% <sup>a</sup> 11.34% <sup>b</sup>	10.54% <sup>a</sup> 11.34% <sup>b</sup>	10.26% <sup>a</sup> 10.98% <sup>b</sup>	10.58% <sup>a</sup> 11.08% <sup>b</sup>	11.05% <sup>a</sup> 11.20% <sup>b</sup>	10.57% <sup>a</sup> 11.24% <sup>b</sup>
Turbulence intensity (Re=5800)	15.41%	22.22% <sup>a</sup> 22.95% <sup>b</sup>	26.64% <sup>a</sup> 29.08% <sup>b</sup>	26.62% <sup>a</sup> 29.00% <sup>b</sup>	26.46% <sup>a</sup> 28.23% <sup>b</sup>	26.69% <sup>a</sup> 28.50% <sup>b</sup>	26.75% <sup>a</sup> 28.46% <sup>b</sup>	26.92% <sup>a</sup> 29.05% <sup>b</sup>

Note: <sup>a</sup> square cross section rib; <sup>b</sup> triangle cross section rib.

When comparing the transverse broken rib and the transverse continuous rib arrangements, the transverse broken arrangements are better than the transverse continuous arrangements for different shape of roughness and Reynolds numbers. The results for the inclined and V shape broken arrangements are somewhat more complicated. For a triangle shape roughness, continuous arrangements of inclined or V shape are better than the broken arrangements of inclined or V shape. However, for square shape roughness, the result is opposite. The broken arrangements of inclined or V shape are better than the continuous arrangements of inclined or V shape. Thus, the choice of broken rib of inclined or V shape should depend on the shape of roughness. However, inclined broken rib and V shape broken rib arrangements are only slightly better than the transverse broken rib arrangement. In addition, they might be more difficult to construct compared to the transverse broken rib arrangement. Thus, the inclined broken rib and V shape broken rib arrangements on the catalyst surface might not be the best choices for a photocatalytic reactor.

## **CHAPTER 4: EXPERIMENTAL STUDY OF A PHOTOCATALYTIC REACTOR WITH SURFACE ROUGHNESS<sup>1</sup>**

### **4.1 Introduction**

There are different kinds of air photocatalytic reactors that have already been reported in the literature, such as honeycomb reactor, plate reactor, annular reactor, etc. [21, 22, 26, 174, 176-179, 260]. For the majority of these, the catalyst is coated on a smooth substrate with the air flow being parallel to the catalyst surface. When the air flows parallel to a smooth catalytic surface, a laminar sublayer is formed over the surface that impedes the mass transfer of contaminants to the catalyst and the associated reaction products to the main flow, therefore, negatively affecting the photocatalytic reaction rate.

The conventional method for thinning the boundary layer is to increase the air flow rate in the reactor [33, 36, 206]. However, increasing airflow rate will reduce the residence time of the air contaminants and leads to incomplete contaminant destruction and more intermediates. An ideal reactor design would be one which enhances the mass transfer rate of the contaminants to the catalytic surface without reducing the residence time.

---

<sup>1</sup> Portions of these results have been previously published (Yangyang Zhang, Elias K. Stefanakos, D. Yogi Goswami. Effect of photocatalytic surface roughness on reactors effectiveness for indoor air cleaning. *Building and Environment*, 61, 188-196, 2013) or under review (Yangyang Zhang, Elias K. Stefanakos, D. Yogi Goswami. Optimum photocatalytic reactor performance with surface roughness arrangement for indoor air cleaning. *Building and Environment*, 2013) and are utilized with permission of the publisher.



Another approach for thinning the boundary layer is to increase the flow turbulent mixing by introducing surface roughness. The impact of surface roughness on the characteristics of fluid flow has been studied for a long time [261]. It has been widely accepted that surface roughness elements have a great effect on the turbulent flow structure leading to an increase in the turbulence intensity and enhanced mass/heat transfer [235-238, 243-246, 251, 253]. Artificial surface roughness could create local wall turbulence when fluid flow on a surface. Secondary recirculation also enhances the convective mass transfer. When air flows over a rough surface, roughness elements reduce the thickness of the boundary layer and a secondary flow from the surface to the core promotes mixing and thus increases the mass transfer (Figure 4.1).

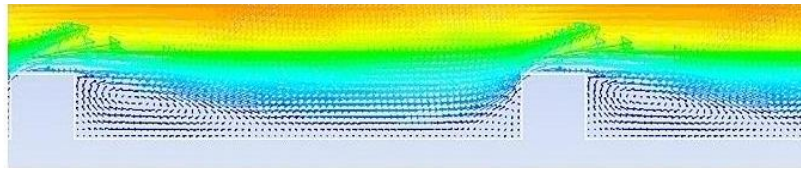


Figure 4.1 Flow pattern of the air flow over a rough surface

The artificial surface roughness can be produced by several methods such as sand blasting, machining, casting, forming, welding ribs and or fixing thin circular wires [262]. Although the effects of surface roughness elements in enhancing the heat/mass transfer have been known for a long time, the only theoretical study is contained in this dissertation (see Chapter 3).

The objective of this study is to verify the theoretical analysis results which are photocatalytic reactor performance improve with artificial roughness on the catalytic surface for indoor air purification. A model photo-reactor is fabricated. Various rough

catalyst plates are experimentally studied in the reactor for air purification. It is found that the photocatalytic reactor performance is greatly improved for all roughness patterns.

## 4.2 Experimental

### 4.2.1 Experimental Set-up

The experimental set-up has been designed and fabricated to study the effect of surface roughness elements in an air photocatalytic reactor. A closed chamber of dimensions 32×32×36in (L×W×H) was used for experimental study (Figure 4.2). A plate type photocatalytic reactor was designed, fabricated and placed inside the chamber. The average UV intensity on the catalyst plate was measured by an EPPLEY UV-A radiometer (290-385nm) and was equal to 100 W/m<sup>2</sup>.

The air flow rate could be regulated by adjusting the voltage of the DC fan and the actually average flow rate was measured by an ALNOR RVA801 anemometer at the inlet side of the reactor. The experimental process was carried out at room temperature and 50% relative humidity. Table 4.1 summarizes the parameters used in the experimental setup.

Table 4.1 Specifications and parameters used in the investigation

<b>Parameters</b>	<b>Specification</b>
Chamber	604 liters airtight
UV intensity	100 W/m <sup>2</sup>
Reynolds number	1450~5800
Air flow rate	0.5~2 m/s
Air contaminant	1ppm toluene
Sample analysis	GC/FID

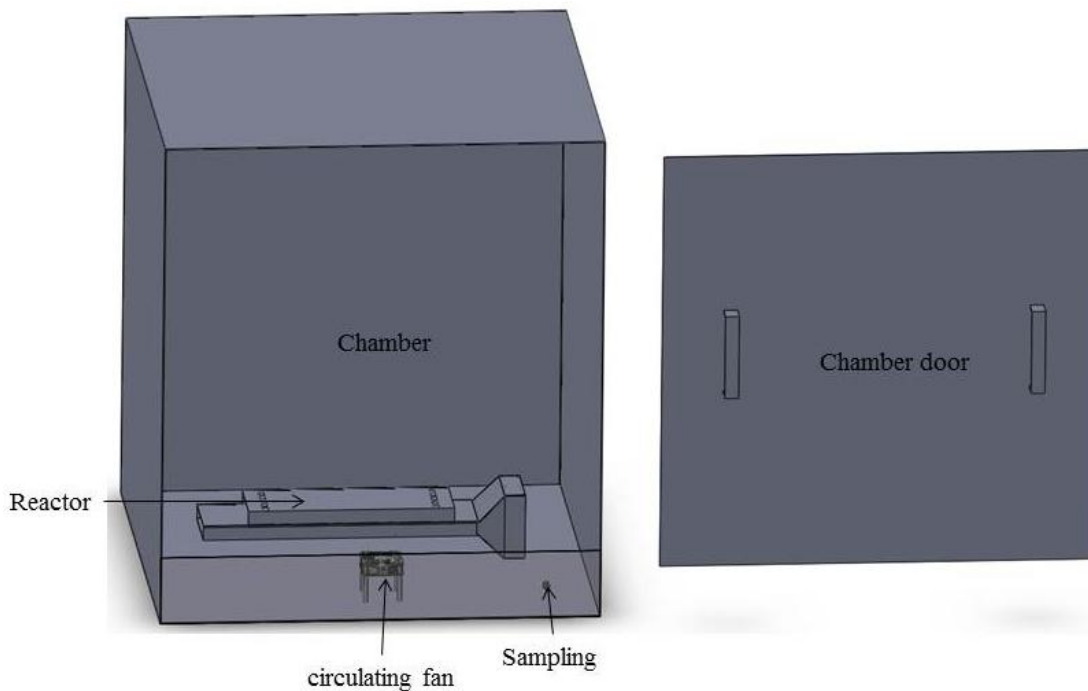


Figure 4.2 Schematic of the experimental set-up

Table 4.2 The details of the GC specification

<b>GC Parameters</b>	<b>Specifications</b>
GC model	SRI8610C
GC column	DB-624 30m
Oven temperature	80°C
Valve temperature	110°C
Detector	FID
Carrier gas	Helium (16psi)
Auxiliary	Air (7psi), H <sub>2</sub> (25psi)
Software	Peaksimple 2000
Sampling volume	1ml

One ppm toluene was used as the representative air contaminant obtained by evaporating 2.6µl of liquid toluene into the chamber. The process of evaporating liquid

toluene into the chamber consisted of the following steps: a) refresh the air in the chamber by turning on the fans with the door open for at least 30min; b) place 2.6 $\mu$ l of liquid toluene under the circulating fan; c) close and seal the chamber door immediately; d) turn on the circulating fan for 30 min to evaporate the toluene. The concentration of toluene in the chamber was analyzed by gas chromatography (GC) with flame ionization detector (FID). Table 4.2 summarizes the details of the GC specifications.

#### 4.2.2 Reactor Design and Fabrication

The reactor was designed and built as shown in Figure 4.3 and Figure 4.4, respectively. The reactor duct consists of a channel with a 2.54 $\times$ 12.7cm (1 $\times$ 5in, H $\times$ W) cross section and 50cm (20in), length (L) which includes three sections, namely, inlet section, test section, and exit section. Both inlet and exit sections were smooth ducts.

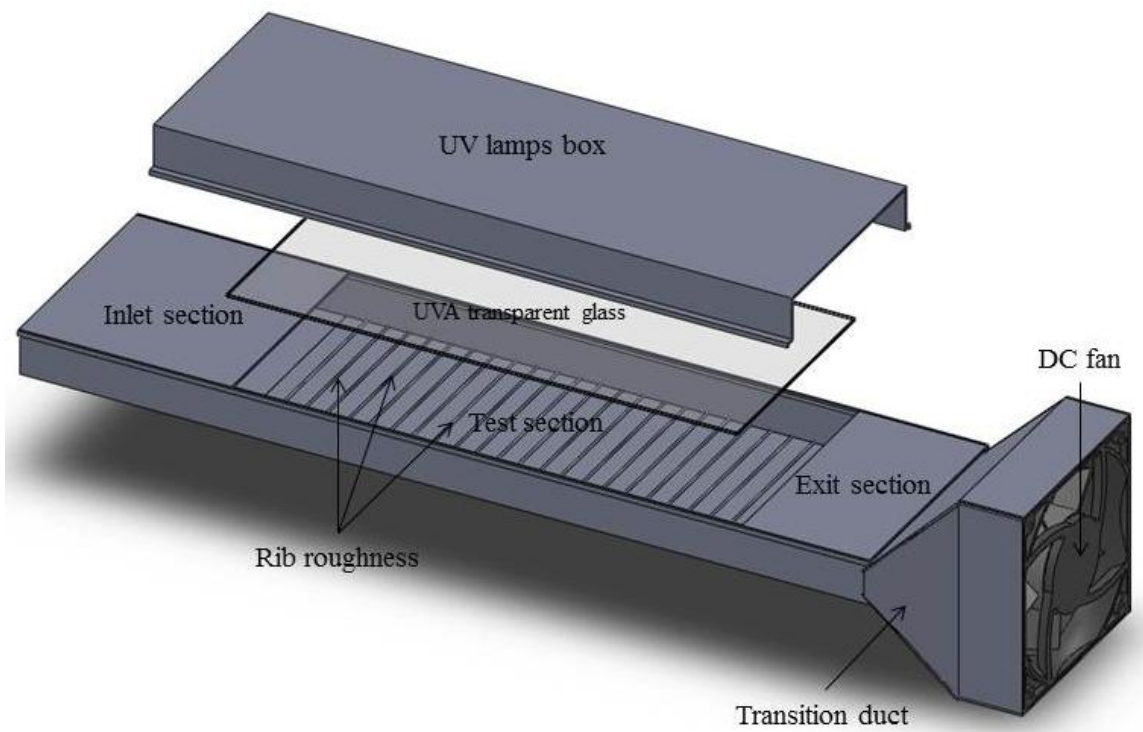


Figure 4.3 The sketch of the photocatalytic reactor

The reflective aluminum sheet (0.022in thick) was used as the main material to build the reactor duct. The catalyst coated aluminum plate was put on the bottom wall of the test section. In order to keep the channel height of the inlet, test and exit sections at the same level, smooth plates of the same thickness were placed on the bottom wall of the inlet and exit sections. A UVA (320-400nm) transparent glass was used as the lid of the test section. A UV lamp box was placed on the top of the test section as the light source. The lamp box includes five RPR-3500A° UVA lamps (12 inches long) and a reflective cover. The UVA lamps emit radiation in a wavelength range between 300 and 400 nm with an approximate Gaussian spectral distribution ( $\lambda_{\max}=350$  nm). The reflective cover was made from a reflective aluminum sheet. A 12V DC fan (5×1.5in, from McMaster-carr) was connected with a transition duct to the exit section to pull the air flow through the reactor (Figure 4.3).

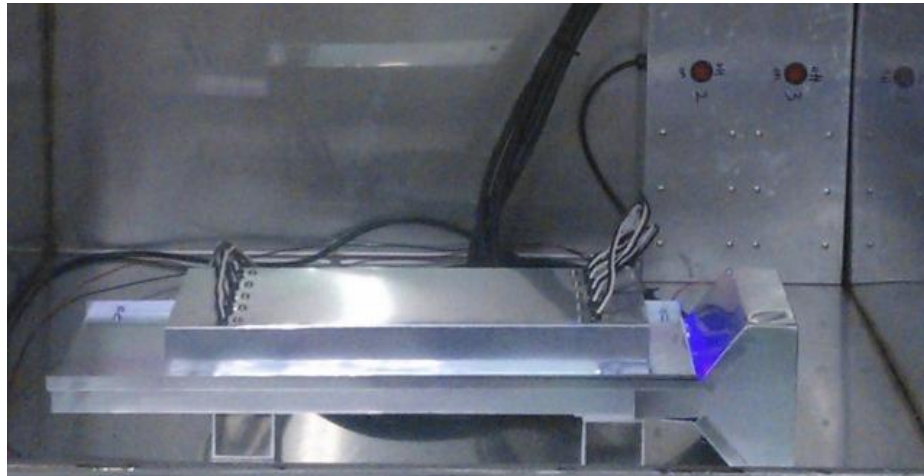


Figure 4.4 The fabricated photocatalytic reactor

#### 4.2.3 Rough Plate Fabrication

The fabrications of rough plates were based on the theoretical analysis results. From the theoretical analysis, the optimal height of roughness ( $e/h$ ) and pitch ratio ( $p/e$ )

was 0.05 and 10, respectively. The optimal flow angle of attack was  $75^\circ$  for inclined, V shape, mesh roughness patterns.

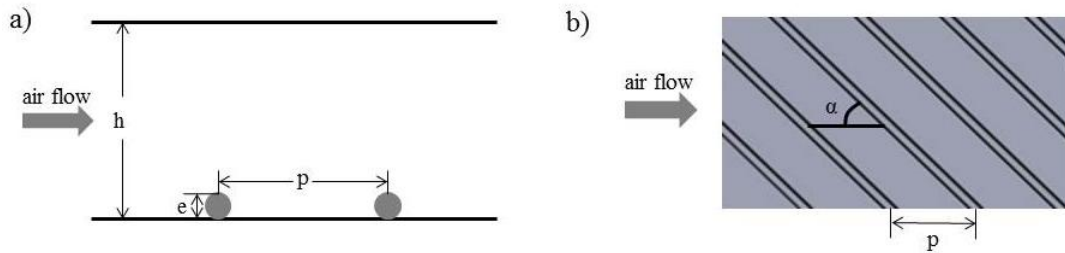


Figure 4.5 Sketch of the roughness elements. a) roughness elements in a channel; b) inclined rough plate. (h: channel height; e: roughness elements height; p: pitch or the distant between two closed roughness elements;  $\alpha$ : air flow angle of attack)

An aluminum plate (0.05in thick) of 12.7×30.48cm (5×12in) size was used as the photocatalyst support substrate. For the transverse, inclined, and V shape roughness, the roughness elements on the roughened plate were chosen as 16 AWG (0.05in diameter) aluminum wires with the distance between two roughness elements as 1.27cm (0.5in) which gives the relative roughness height ( $e/h$ ) and pitch ratio ( $p/e$ ) are 0.05 and 10, respectively (Figure 4.5). Aluminum wires were fixed on the aluminum plate as rib roughness elements by drilling small holes on the edge of the plate and tying a 36 AWG (0.005in diameter) wire on it. For the mesh roughness plate, a commercial stainless steel flattened mesh was fixed on the plate. The thickness of the mesh was 0.127cm (0.050in) and the overall diamond size of the mesh was 1.27×3.2cm (0.5×1.26in). Thus, the relative roughness height ( $e/h$ ) and pitch ratio ( $p/e$ ) of the mesh roughness were 0.05 and 10, respectively. In order to study the effect of non-optimal roughness surface, a transverse continuous rib with a pitch ratio ( $p/e$ ) of 5 (transverse No.2) and a random rough catalyst surface were also fabricated. Table 4.3 summarizes the parameters of the various studied roughness plates.

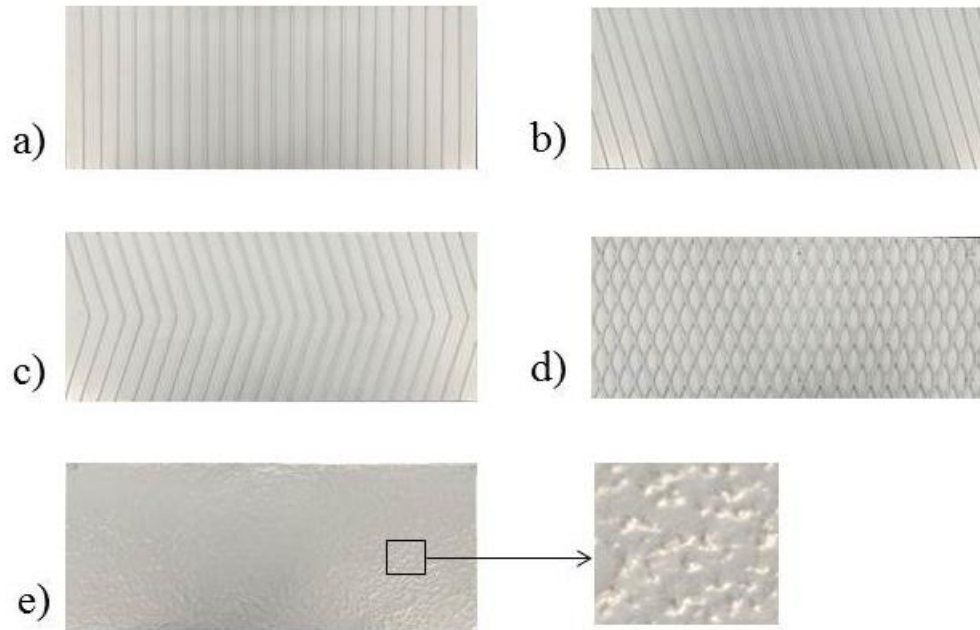


Figure 4.6 Various rough plates. a) transverse; b) inclined; c) V shape; d) mesh; e) random.

Table 4.3 The detail parameters of various studied rough catalyst plates

Roughness type	Height of roughness	Pitch ratio	Flow angle of attack
	(e/h)	(p/e)	( $\alpha$ )
transverse No.1	0.05	10	90°
transverse No.2	0.05	5	90°
inclined	0.05	10	75°
V shape	0.05	10	75°
mesh	0.05	10	75°
random	0~0.05	--	--
smooth	0	--	--

#### 4.2.4 Catalyst Coating

The photocatalyst (TiO<sub>2</sub>, Degussa P25) was immobilized on the aluminum plates by the spray coating method. The coating procedure was:

1. Aluminum plates were cleaned by 95% ethanol prior to spraying.
2. 1g of TiO<sub>2</sub> powder was suspended in 20ml 95% ethanol to make TiO<sub>2</sub>-ethanol slurry.
3. The TiO<sub>2</sub>-ethanol slurry by stirred by a mini vortexer for 5min to produce uniform TiO<sub>2</sub>-ethanol slurry.
4. The suspension was uniformly sprayed on the cleaned aluminum plates using a spraying device (Paasche HAPK airbrush).
5. After spraying, the plates were kept at room temperature for 1h and then dried in an oven at 110°C for 12h.



Figure 4.7 TiO<sub>2</sub> photocatalyst was sprayed on the transverse No.1 rough plate

Due to some TiO<sub>2</sub> being sprayed outside the plate (Figure 4.7), the amount of TiO<sub>2</sub> sprayed on the plate (W) was calculated from:

$$W = \frac{V_s \times C_{\text{TiO}_2}}{A_s} \times A_p \quad (4.1)$$

where W is the total weight of TiO<sub>2</sub> sprayed on the plate; V<sub>s</sub> is the volume sprayed; C<sub>TiO<sub>2</sub></sub> is the concentration of the TiO<sub>2</sub>-ethanol solution; A<sub>s</sub> is the area of spray; A<sub>p</sub> is the area of the plate.



In order to study the effect of catalyst loading on the reactor performance, different volumes of TiO<sub>2</sub>-ethanol solutions were sprayed to make different amounts (or different thickness) photocatalyst coatings on plates varying from 50 to 300 mg per plate. For the rough plates, a value of 250mg TiO<sub>2</sub> was chosen. After TiO<sub>2</sub> was immobilized on the aluminum plates, they were tested at 35psi compressed air to make certain that the catalyst retained good adherences.

### 4.3 Results and Discussion

#### 4.3.1 The Effect of Catalyst Loading

Figure 4.8 shows the results of the photocatalytic reactor degradation 1ppm toluene in the chamber with different amounts of catalyst spray on the smooth plate from 0.13 to 0.78mg/cm<sup>2</sup> (50 to 300mg/plate). The Reynolds number is 2900 and the average air flow rate is 1m/s.

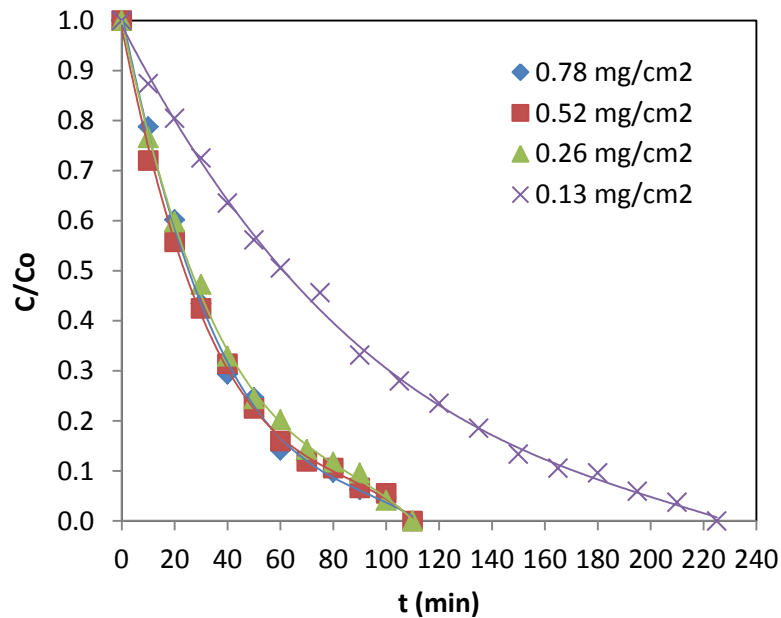


Figure 4.8 Effect of catalyst loading on a smooth plate on the photocatalytic oxidation 1ppm toluene at Reynolds number of 2900

It is clear that the cleaning times are greatly reduced when the catalyst loading increased from 0.13 to 0.26 mg/cm<sup>2</sup>. However, for the catalyst loading over 0.26 mg/cm<sup>2</sup> (100 mg/plate), the performance does not improve with the catalyst loading. Although thick films favor catalytic oxidation, the photocatalysis process only occurs on the catalyst surface or near the surface where the UV light is incident. In order to ensure sufficient thickness, a catalyst loading of 0.65 mg/cm<sup>2</sup> (or 250 mg/plate) is used in this study.

#### 4.3.2 The Effect of Reynolds Number

Both smooth and transverse rough plates are studied to determine the effect of Reynolds numbers on the reactor performance. Figure 4.9 shows the results for a smooth catalyst plate with the Reynolds number varying from 1450 to 5800. The corresponding average air flow rate varied from 0.5 to 2 m/s.

From Figure 4.9, the times for cleaning 1ppm toluene are 155, 110, 80, and 75min for a smooth catalyst plate at the Reynolds numbers of 1450, 2900, 4300, and 5800, respectively. The cleaning time is reduced substantially when the flow transitions from laminar to turbulent. The turbulent flow increases the mass transfer of the contaminants to the catalyst surface and leads to an enhancement in the effectiveness of photocatalysis. Moreover, there is more air passing through the reactor at higher air flow rate for the same period, therefore, the concentration of toluene is reduced faster in the chamber. However, with further increase in the Reynolds number, the cleaning time reduced is less affected by Reynolds number. Although there is greater volume of air passing through the reactor at higher Reynolds numbers (higher air flow rate) for the same time period, the residence time of the air contaminants is reduced, therefore, the single pass oxidation

efficiency is also reduced. Thus, the cleaning times are only slightly different between Reynolds number at 4300 and 5800.

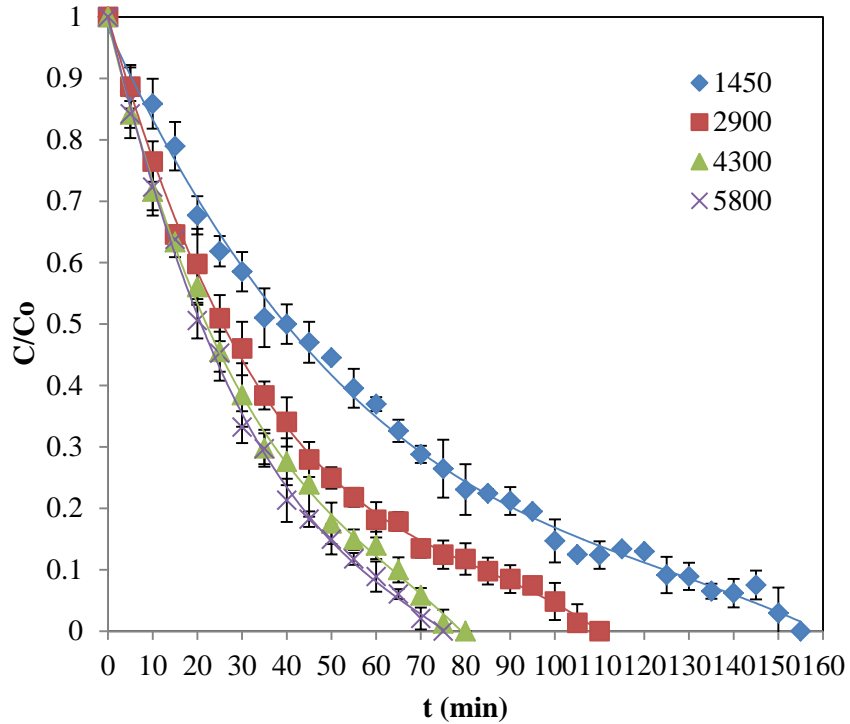


Figure 4.9 Comparison of results for different Reynolds numbers for a smooth catalyst plate and 1ppm toluene degradation in the chamber (Reynolds number: 1450~5800, Catalyst loading: 0.65 mg/cm<sup>2</sup>; error bars represent standard deviation for the tests)

Figure 4.10 shows the results of the reactor with transverse No.1 rough catalyst plate for Reynolds numbers from 1450 to 5800. The 1ppm toluene cleaning times are 120, 65, 55, and 50 min for the Reynolds number of 1450, 2900, 4300, and 5800, respectively. The cleaning time is greatly reduced compared to a reactor with a smooth catalyst plate for the same Reynolds number (Table 4.4). The transverse ribs roughness on the catalytic surface creates local wall turbulence and enhanced the convective mass transfer of air contaminants to the catalytic surface and thus enhanced the effectiveness of photocatalysis.

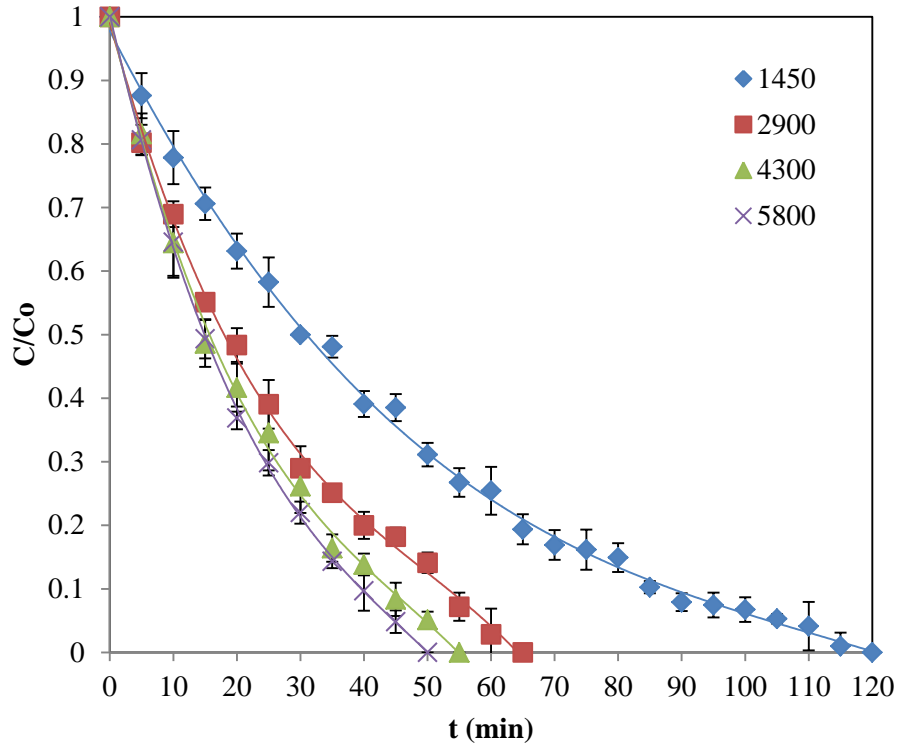


Figure 4.10 Comparison of transverse No.1 rough catalyst plates with different Reynolds numbers for 1ppm toluene degradation (Reynolds number: 1450~5800, error bars represent the standard deviation for the tests)

Table 4.4 Comparison of the 1ppm toluene cleaning time between smooth and transverse No.1 catalyst plate

Reynolds number	Cleaning time (min)	
	Smooth	Transverse No.1
1450	155	120
2900	110	65
4300	80	55
5800	75	50

For the reactor with transverse No.1 catalyst surface, the cleaning time is greatly reduced when the Reynolds number is increased from 1450 to 2900. However, the reactor

performance is less affected by the Reynolds number at higher Reynolds number. For the Reynolds number of 2900, the cleaning time is 65min which is almost half of the Reynolds number at 1450 in 120min. For Reynolds number higher than 2900, the cleaning time is only slightly reduced especially when the Reynolds number is higher than 4300.

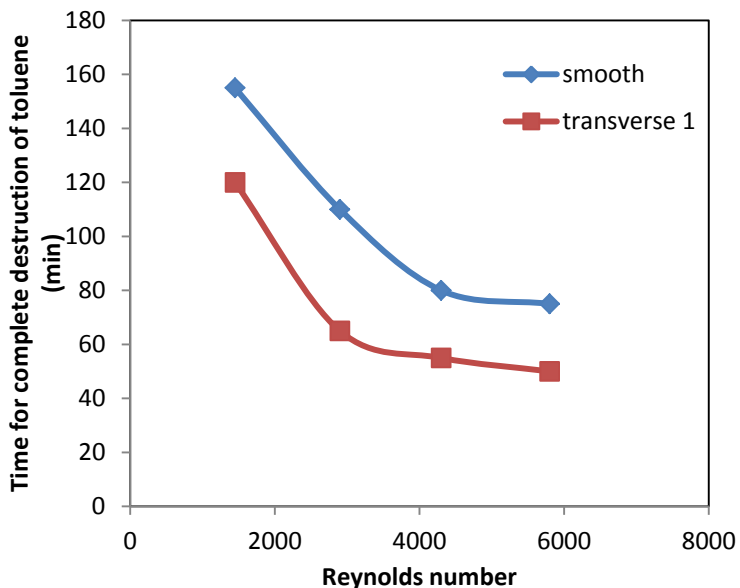


Figure 4.11 Comparison of cleaning times of 1ppm toluene in the chamber for the reactors with a smooth catalyst plate and a transverse rough catalyst plate

#### 4.3.3 The Effect of the Increased Surface Area in the Rough Plates

The reaction surface area plays an important role in photocatalysis. Although the surface area of the rough surface in this study is slightly larger than a smooth surface, rough surfaces also create shadows or higher UV incident angle when compared to a smooth surface. In order to study the impact of the increased surface area in a rough catalyst surface, the transverse continuous rib catalyst plate with the roughness elements without coated catalyst (transverse No.3) is studied. In the transverse No.3 catalyst plate, the clean wires are fixed on a smooth catalyst plate with the pitch ratio (p/e) as 10. Thus,

the reaction surface area of the transverse No.3 was reduced compared to a smooth catalyst plate due to the increased shadows during the photocatalysis process (Figure 4.12).

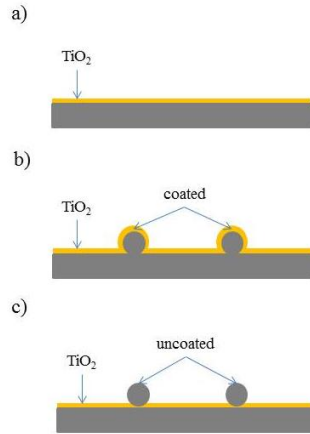


Figure 4.12 Schematic of  $\text{TiO}_2$  coated on various plates. (a) smooth surface (b) transverse No.1 (c) transverse No.3

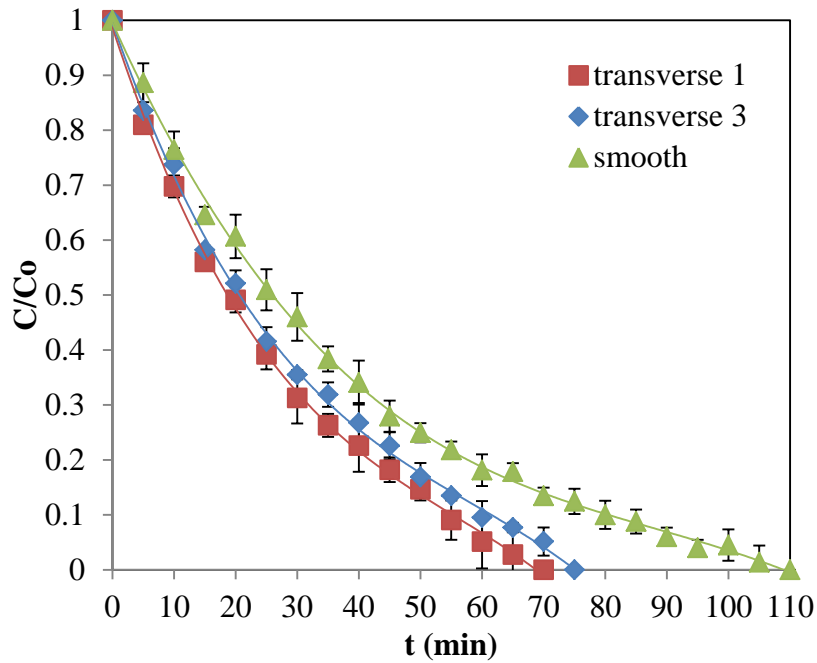


Figure 4.13 Comparison of toluene photocatalytic oxidation of the reactor with the transverse No.1, transverse No.3 and smooth catalyst plates at Reynolds number 2900. (transverse 1: rib roughness elements coated. transverse 3: rib roughness element without coated catalyst)

Figure 4.13 compares the toluene degradation of the smooth, transverse No.1 (ribs coated) and transverse No.3 (ribs not coated) catalyst plates. The overall reaction rate constants ( $k$ ) are 0.0278, 0.0381, 0.0346, and  $\text{min}^{-1}$  respectively for the reactors with smooth, transverse No.1 and transverse No.3 catalyst plate. The performance of the transverse No.3 is much higher than a smooth catalyst surface and close to transverse No.1 even though the reaction surface area is the smallest. Thus, the increased turbulence intensity is much greater than the slightly increased reaction surface area of a rough catalyst surface. The contribution of the increased reaction surface area of the rough plate in photocatalytic process could be ignored in this study. The slightly different of the transverse No. 3 and transverse No.1 is because the roughness ribs are not coated of the transverse No.3.

#### 4.3.4 The Effect of Various Roughness Patterns

Figure 4.14 compares the toluene degradation in the reactor with different roughness patterns on the catalyst surface at the Reynolds number of 2900. It is clear that the cleaning time is greatly reduced for a reactor with various rough catalyst surfaces compared to a reactor with a smooth catalyst surface. Although there is some difference in the cleaning time for the various roughness patterns, it is difficult to distinguish the performance between them because the cleaning times are very close to each other and there are larger detected errors at lower concentrations of toluene.

In this study, photocatalytic oxidation may follow a pseudo-first-order expression due to the low concentration of toluene (less than 1ppm) [32]:

$$r = -\frac{d[\text{toluene}]}{dt} = kC_{\text{toluene}} \quad (4.2)$$

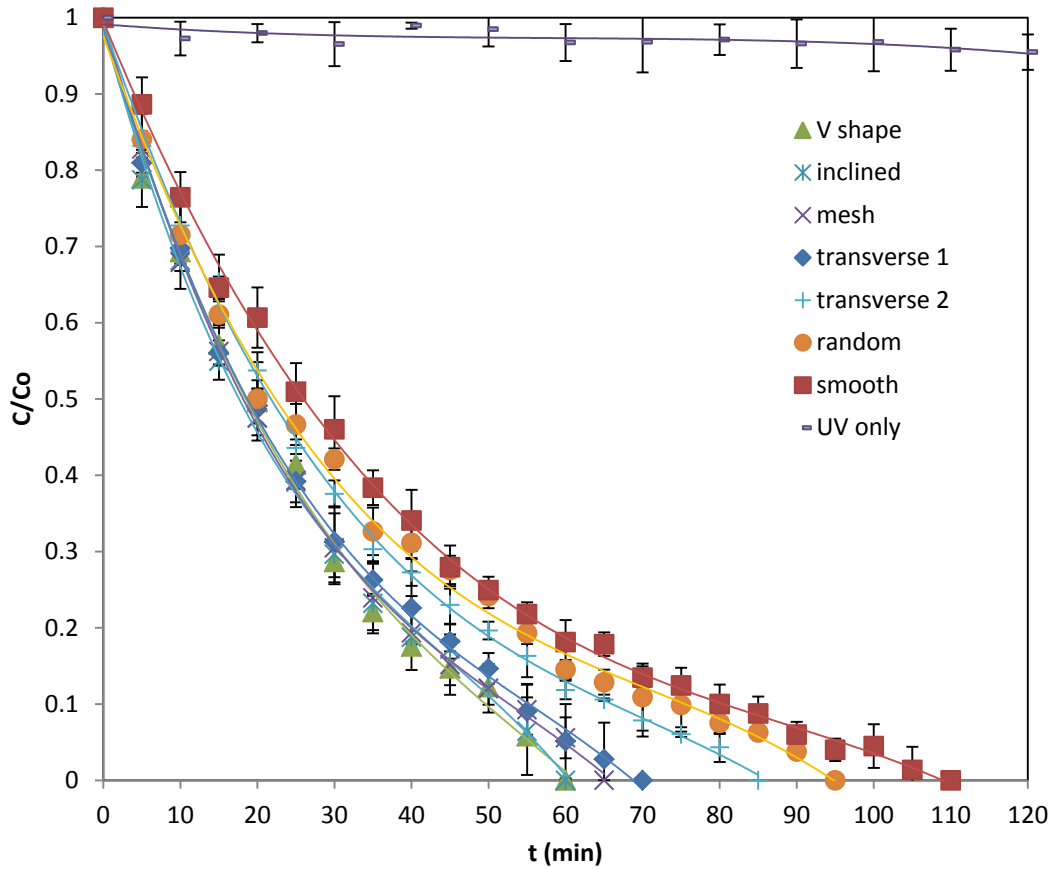


Figure 4.14 Comparison of the photocatalytic reactor performance results for the reactor with smooth and various rough catalyst surfaces for cleaning the contaminated air in the chamber (transverse 1:  $p/e=10$ ; transverse 2:  $p/e=5$ ; Contaminants: 1ppm toluene; Reynolds number: 2900; error bars represent standard deviations for the tests.)

Figure 4.15 presents the degradation rate in terms of  $-\ln(C/C_0)$ . The slope of each line represents the overall reaction rate constant ( $k$ ), which is 0.0418, 0.0411, 0.0394, 0.0381, 0.0357, 0.0312, 0.0277  $\text{min}^{-1}$  respectively for the reactors with V shape, inclined, mesh, transverse No.1, transverse No.2, random, and smooth catalyst plate. Thus, the order of the reactor performance with various rough catalyst surfaces could be V shape > inclined > mesh > transverse No.1 > transverse No.2 > random > smooth. The results match the theoretical study and indicate that study of the turbulence intensity of reactor channels is an effective way to predict the performance of the photocatalytic reactor.



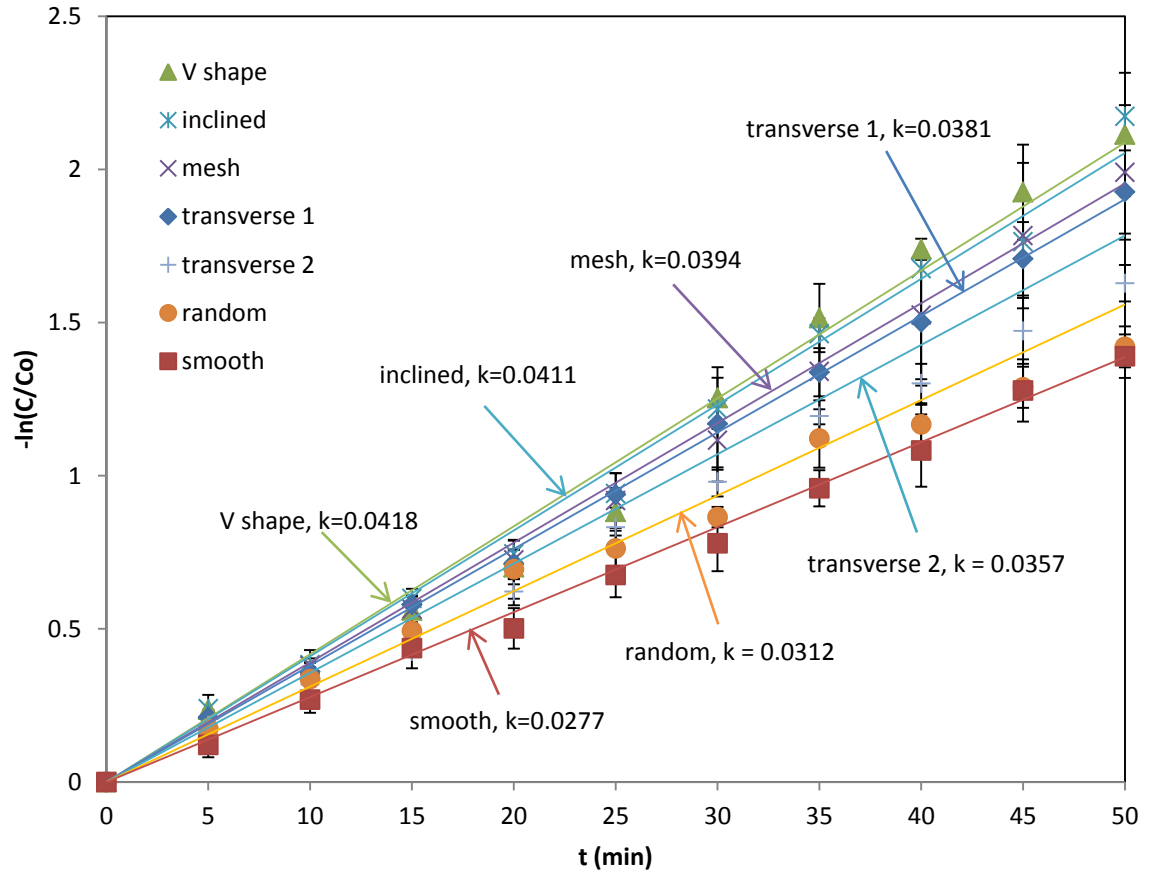


Figure 4.15 Comparison of toluene photocatalytic oxidation results for the reactor with various rough catalyst plates at a Reynolds number of 2900 in terms of  $-\ln(C/C_0)$  (transverse 1:  $p/e=10$ ; transverse 2:  $p/e=5$ ; error bars represent the standard deviations for the tests.)

#### 4.3.5 Empirical Correlation

Two main factors affecting the performance of the reactor considered in this study are the turbulence intensity (I) and the Reynolds number (Re). Figure 4.16 plots the overall reaction rate constant (k) with the corresponding turbulence intensity in the reactor at Reynolds numbers from 2900 to 5800. It is clear that the relationship between the reaction rate constant (k) and the turbulence intensity (I) is linear for the each Reynolds number.

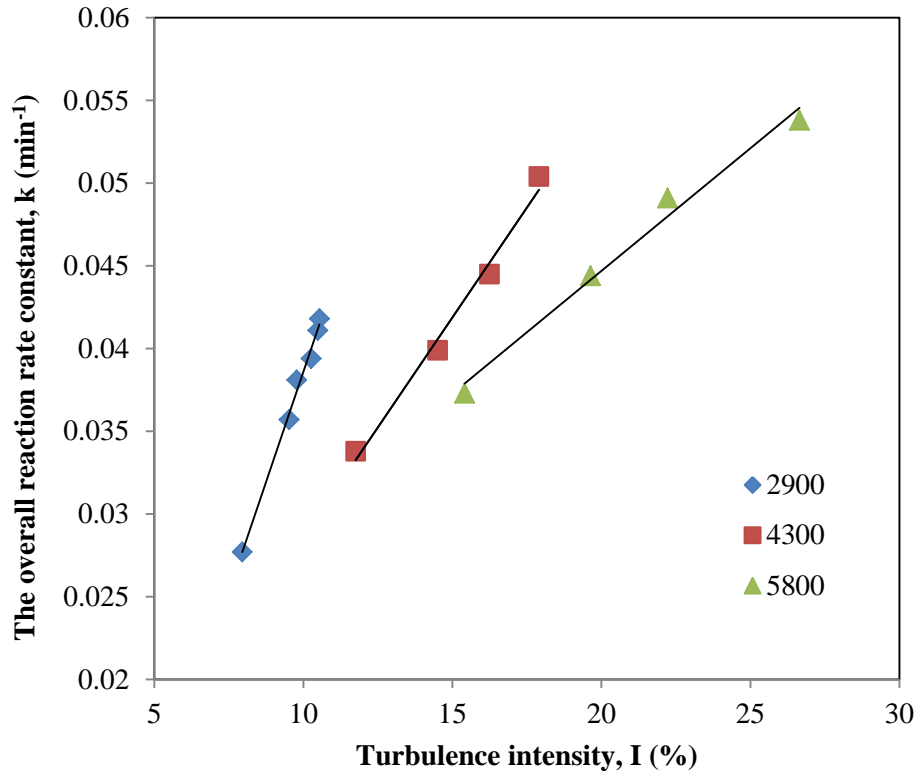


Figure 4.16 Plot of the overall reaction rate constant ( $k$ ) versus turbulence intensity for the Reynolds numbers of 2900, 4300, and 5800

Based on the above relationship between the reaction rate constant ( $k$ ) and the turbulence intensity ( $I$ ) at the Reynolds numbers from 2900 to 5800, an empirical correlation could be written as:

$$k = \left[ 0.0028 \times \left( \frac{Re}{2900} \right)^2 - 0.0122 \times \left( \frac{Re}{2900} \right) + 0.0147 \right] \times I + \left[ 0.0296 \times \left( \frac{Re}{2900} \right) - 0.0436 \right] \quad (4.3)$$

where  $k$  is the overall reaction rate ( $\text{min}^{-1}$ );

$Re$  is the Reynolds number (2900~5800);

$I$  is the magnitude of the turbulence intensity (%).

Figure 4.17 shows a comparison of the results from experiments and the empirical correlations. The empirical correlations match well with the experimental values at different Reynolds numbers. Thus, the empirical correlations expression (4.3) could be

used to find out the overall reaction rate constant ( $k$ ) of the photocatalytic reactor for different Reynolds numbers and turbulence intensities.

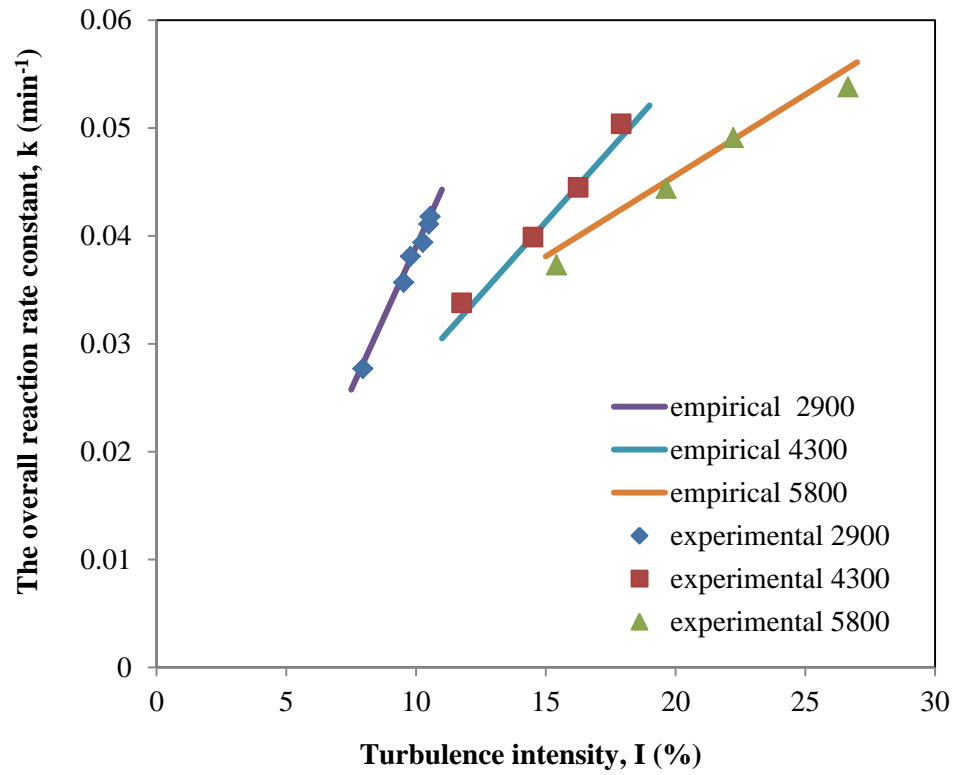


Figure 4.17 Comparison of experimental values and empirical correlation at Reynolds numbers from 2900 to 5800

## CHAPTER 5: ZINC OXIDE NANOWIRE PHOTOCATALYSTS<sup>1</sup>

### 5.1 Introduction

Although TiO<sub>2</sub> is the most commonly studied photocatalyst in both air and water for the decontamination of organic compounds, ZnO could be an alternative because of its comparable band gap energy (3.3eV) [263] with TiO<sub>2</sub> (3.2eV) [264] and relatively lower production cost [96-98]. The problem of ZnO in high acidic environments could be solved by regulation of the pH before water treatment. Moreover, ZnO has been shown to be a more efficient photocatalytic nanomaterial than TiO<sub>2</sub> particularly noticeable for photooxidation of 2-phenylphenol and phenol [99-102, 265] due to higher generation and separation of photo-induced electrons and holes [96, 103, 104].

The surface area of the photocatalyst plays a significant role because the contaminants needed to be absorbed on the surface for a decontamination and degradation processes. The nanoparticles have shown the larger surface area, but have been limited in suspension which requires the separation and recovery in photocatalyst remediation. However, the photocatalyst immobilize on the steady substrates could able to eliminate such problems. Normally, nanowires offer a higher surface to volume ratio compared to the nanoparticles coated on flat surfaces [51]. Chemical vapor deposition

---

<sup>1</sup> Portions of these results have been previously published (Yangyang Zhang, Manoj K. Ram, Elias K. Stefanakos, D. Yogi Goswami. Enhanced photocatalytic activity of iron doped zinc oxide nanowires for water decontamination. *Surface & Coatings and Technology*, 217, 119-123, 2012) and are utilized with permission of the publisher.

(CVD) [266], physical vapor deposition (PVD) [267], vapor-liquid-solid (VLS) methods [120], and hydrothermal methods [268] have been used to synthesize ZnO nanowires. The recent studies on hydrothermally grown nanowires have shown inherent oxygen vacancies in grown ZnO crystal [51]. The photocatalytic nanomaterials with inherent oxygen defects have been found to photocatalytic activity even without the transitional metal doping [125]. Moreover, the hydrothermal method is simple water based synthesis and could be suitable for the large-scale preparation [97].

Although many different modifications of ZnO nanowires have been studied, to the best of our knowledge, the synthesis of ZnO/Fe nanowires for photocatalytic detoxification applications has not been investigated. In this study, a conventional hydrothermal method is used to synthesize ZnO and ZnO/Fe nanowires on glass substrates. The photocatalytic activities of ZnO and ZnO/Fe nanowires have been grown on glass substrates for the photocatalytic decomposition of dichlorobenzene (DCB) and methyl orange (MO) in water.

## **5.2 Experimental Procedure**

### **5.2.1 ZnO Nanowire Growth**

25 mM zinc nitrate ( $\text{Zn}(\text{NO}_3)_2$ ) and 25 mM of hexamethylenetetramine (HMTA) were dissolved in deionized (DI) as the growth solution.

500  $\mu\text{l}$  of seed solution (5 mM of zinc acetate in ethanol) was dropped on a pre-cleaned 9 cm glass petri dish. Subsequently, the dish was tilted at different directions and assures uniform coverage of the dish bottom surface. The ethanol was allowed to evaporate from the dish for certain time. The dish was dried in a furnace at  $80^\circ\text{C}$  for 10

min, followed by calcination at 390°C for 30 min to form a ZnO seeded layer on the bottom of petri dish. The ZnO seeded layer acted as a nucleation site for nanowire growth.

A schematic of the ZnO nanowire growth procedure is presented in Figure 5.1. The ZnO seeded petri dish was submerged into the growth solution at 90 °C for 2 hours. The solution was stirred constantly. The dish was removed from the solution, rinsed with DI water, and dried by using hot air. The dish was then dried in a furnace at 100 °C for 10 min to remove water and organic solvents, followed by raising the temperature to 250 °C for 1 hour to further remove any unreacted organic compound.

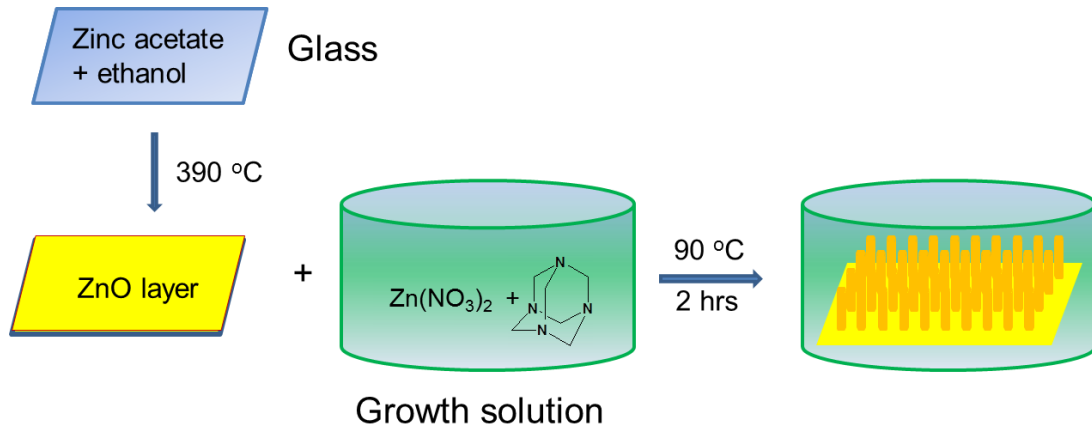


Figure 5.1 A flow schematic of the ZnO nanowire growth procedure

The ZnO/Fe nanowires were grown on a Fe doped ZnO seeding layer using 5 mM of zinc acetate and 5 mM FeCl<sub>3</sub> in ethanol as the seed solution. The seeding layer is expected to produce a ZnO/Fe film after calcination. The other processes were similar to that used for the growth of ZnO nanowires. It is important to point out that Fe<sup>3+</sup> ions cannot be added directly into the growth solution for doping nanowires during the synthesis process. Based on our experiments, the solution would promote the Fe(OH)<sub>3</sub>

phase during synthesis process if  $\text{Fe}^{3+}$  ions were added into the growth solution. This is because the solution product ( $K_{sp}$ ) of  $\text{Fe}(\text{OH})_3$  is much smaller than  $\text{Zn}(\text{OH})_2$ .

#### 5.2.2 The Amount of Grown Nanowires

The amount of nanowires grown on the glass plate was estimated by weighing the plate before and after the ZnO nanowire growth.

#### 5.2.3 $\text{TiO}_2$ Coated on the Dish

In order to compare the photoactivity of ZnO nanowires with  $\text{TiO}_2$  (P25), the  $\text{TiO}_2$  was coated on a similar petri dish. A certain amount of  $\text{TiO}_2$  (same as the ZnO nanowire growth on the dish) was dispersed in 50 ml of ethanol. The solution was poured onto a 9 cm glass petri dish and slowly evaporated in a fume hood. Once the visible ethanol was evaporated, the dish was dried in a furnace at 80 °C for 10 min followed by an hour of drying at 250°C.

#### 5.2.4 Surface/structure Characterization

Ultraviolet-visible (UV-vis) diffuse reflectance spectra were measured by Ocean Optics spectrophotometer. The dimensions and crystal structure of the nanowires were investigated by Hitachi S-800 scanning electron microscope (SEM) operated at 25 kV. The crystallinity of the nanowires and the preferred crystal orientation were measured using Philips X-ray diffraction (XRD). The optical band shifts were measured using Raman spectroscopy by a Renishaw Raman spectrophotometer.

#### 5.2.5 Photocatalysis Study

The photocatalytic activity was evaluated by the photo degradation of two important contaminants, dichlorobenzene (DCB) and methyl orange (MO), in water with initial concentrations of 10 ppm and 20 ppm, respectively. Both UV and white light

irradiation were used in this study. The DCB photo degradation was studied by using 50 ml of DCB in a petri dish containing the nanowires. The depth of water was calculated to be 0.78 cm. The dish was covered by a BK-7 glass to reduce evaporation during the photocatalytic process (Figure 5.2). The intensity of irradiation on the catalyst surface was measured by LI-COR pyranometer. The intensity of white light used in the experiment was  $60 \text{ W/m}^2$  in the visible spectrum, in addition to  $2 \text{ W/m}^2$  in the UV spectrum. The intensity of UV light was  $30 \text{ W/m}^2$ . The DCB sample was analyzed using gas chromatograph (GC) with flame ionization detector (FID). The GC was SRI8600 with a 30 m DB-624 capillary column. The experimental setup for the photocatalytic degradation of methyl orange (MO) was similar to that used for the DCB degradation. 50ml of 20 ppm MO was put into a petri dish containing nanowires. Ocean Optics spectrophotometer was used to monitor the decolorization of the MO by detecting the absorption at 460nm.

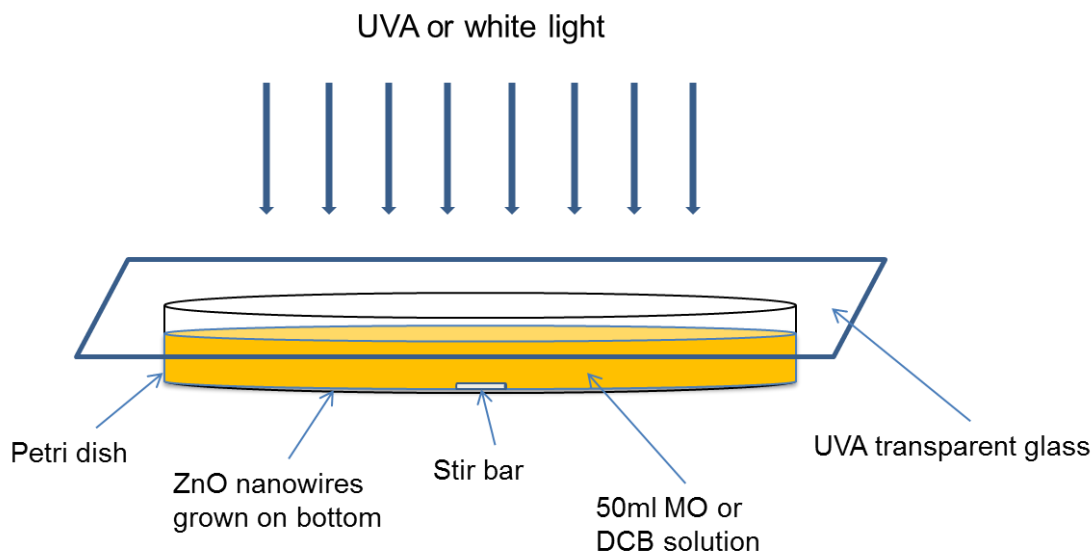


Figure 5.2 Experimental setup of the photocatalytic study



### 5.3 Results and Discussion

#### 5.3.1 The Growth Amount of Nanowires

Table 5.1 shows the net weight of the nanowires on a 9 cm glass petri dish synthesized for 2 hours. The average weight of the nanowires is calculated to be 19.7 mg. The density of nanowires on the dish is mostly uniform with the average nanowire density being estimated at about 0.286 mg/cm<sup>2</sup>. For the ZnO/Fe nanowires, the seeding layer was formed using 500 µl of 5 mM zinc acetate and 5 mM FeCl<sub>3</sub> in ethanol as the seed solution. Thus, the seeding layer is expected to be a ZnO/Fe film with 0.14 mg Fe. The percentage of Fe in the overall ZnO/Fe nanowires is then calculated to be about 0.7%.

Table 5.1 The growth amount of nanowires on the 9cm diameter petri dish

	1	2	3	4	5	Average
Net weight (mg)	18.1	20.3	17.2	22.0	20.8	19.7

#### 5.3.2 UV-vis Absorbance Spectrum

Figure 5.3a compares the UV-vis absorbance spectrum of different ZnO nanostructures. The ZnO nanoparticles (US Research Nanomaterials, Inc. 10-30nm) do not absorb visible light which the wavelength from 400 to 700 nm. However, the ZnO nanowires show some absorption in the visible range. The ZnO/Fe nanowires improve absorption in both the UV and visible light than the ZnO nanoparticles and ZnO nanowires, revealing the significance in photocatalytic degradation under both UV and visible light. This may be because Fe<sub>2</sub>O<sub>3</sub> present in the ZnO/Fe nanowires.

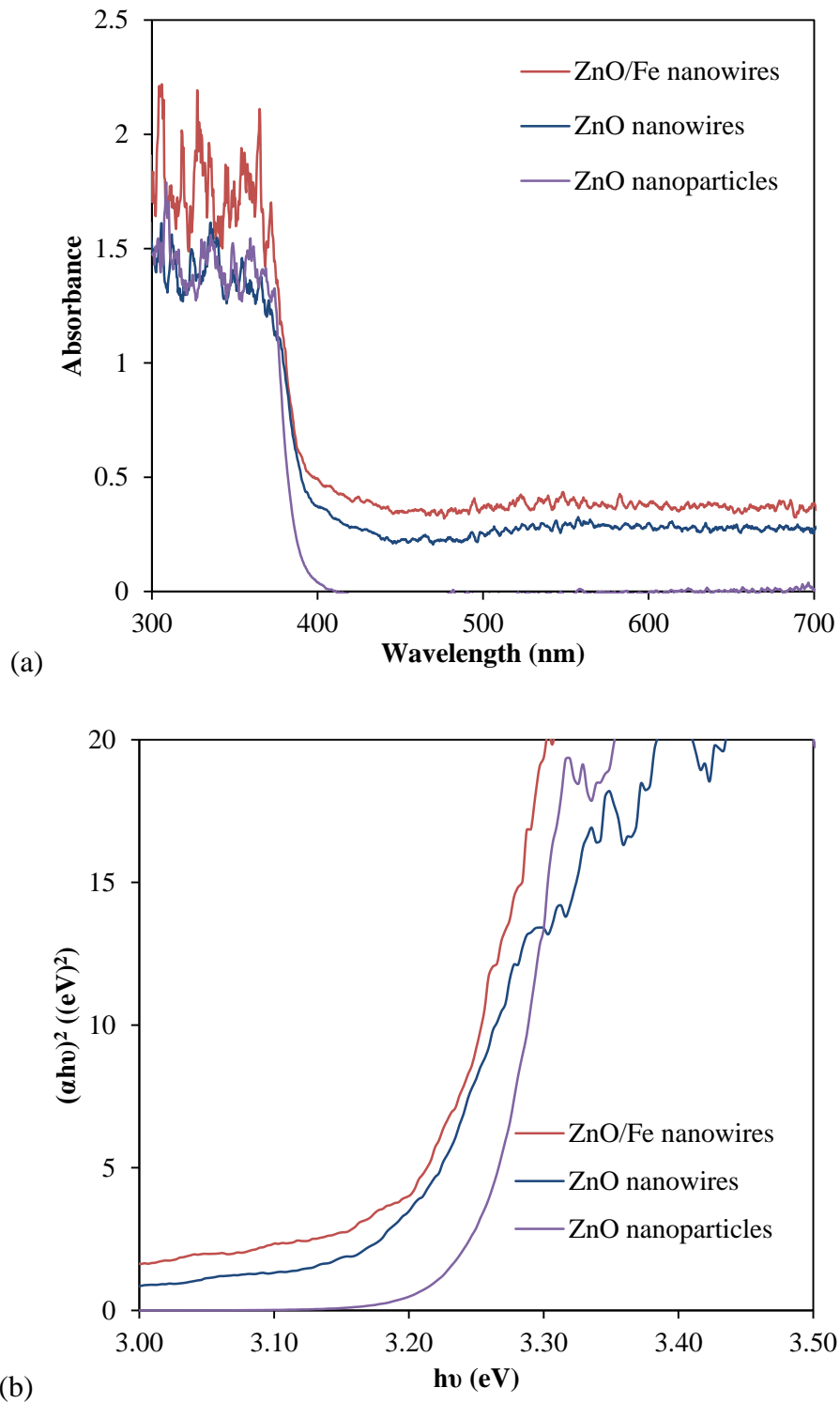


Figure 5.3 UV-vis. (a) Absorption spectra. (b) Plots of  $(\alpha h\nu)^2$  versus  $h\nu$  of the catalysts

For a semiconductor, the optical absorbance can be expressed by the equation [269]:

$$\alpha h\nu = B(h\nu - E_g)^{1/2} \quad (5.1)$$

where  $\alpha$  is the absorbance intensity at a light frequency  $\nu$ ,  $B$  is the absorbance constant and  $E_g$  is the band gap energy.

Figure 5.3b shows the plots of  $(\alpha h\nu)^2$  versus  $h\nu$ . The direct band gap energies are obtained by the intercept of the linear extrapolation to the  $h\nu$  axis. The direct band gap energies of ZnO nanoparticles, ZnO nanowires, and ZnO/Fe nanowires are estimated to be 3.26, 3.18, and 3.17 eV, respectively. The band gaps of ZnO (3.18 eV) and ZnO/Fe (3.17 eV) nanowires are lower than the bandgap of ZnO (3.26 eV) nanoparticles. The smaller band gap of vertically grown ZnO nanowires has been reported in the literature and is caused by the crystalline defects in the nanowires due to the hydrothermal synthesis [270, 271].

### 5.3.3 Structural Studies

Figure 5.4 depicts a top down image of ZnO nanowires (Figure 5.4a) and ZnO/Fe nanowires (Figure 5.4b). The diameter of the ZnO nanowires varies from 30 to 50 nm. The diameter of the ZnO/Fe nanowires varies from 50 to 100 nm with a definitive hexagonal structure. The average diameters of the ZnO/Fe and ZnO nanowires are different because of the different seeded layers [131].

Figure 5.5 (a and b) shows the X-ray diffraction (XRD) patterns of ZnO nanowires and ZnO/Fe nanowires. In Figure 5.5, the two samples do not show any obvious difference. This finding could be explained by considering that the Fe content in the ZnO/Fe samples is below the detection limit. Another explanation is that all the Fe

atoms might substitute Zn atoms and integrate into the crystal lattice of ZnO. The diffraction peak at (002) in ZnO nanowires is due to a higher degree of orientation along the vertical c-axis. The XRD results show highly crystallized structures of both ZnO and ZnO/Fe nanowires.

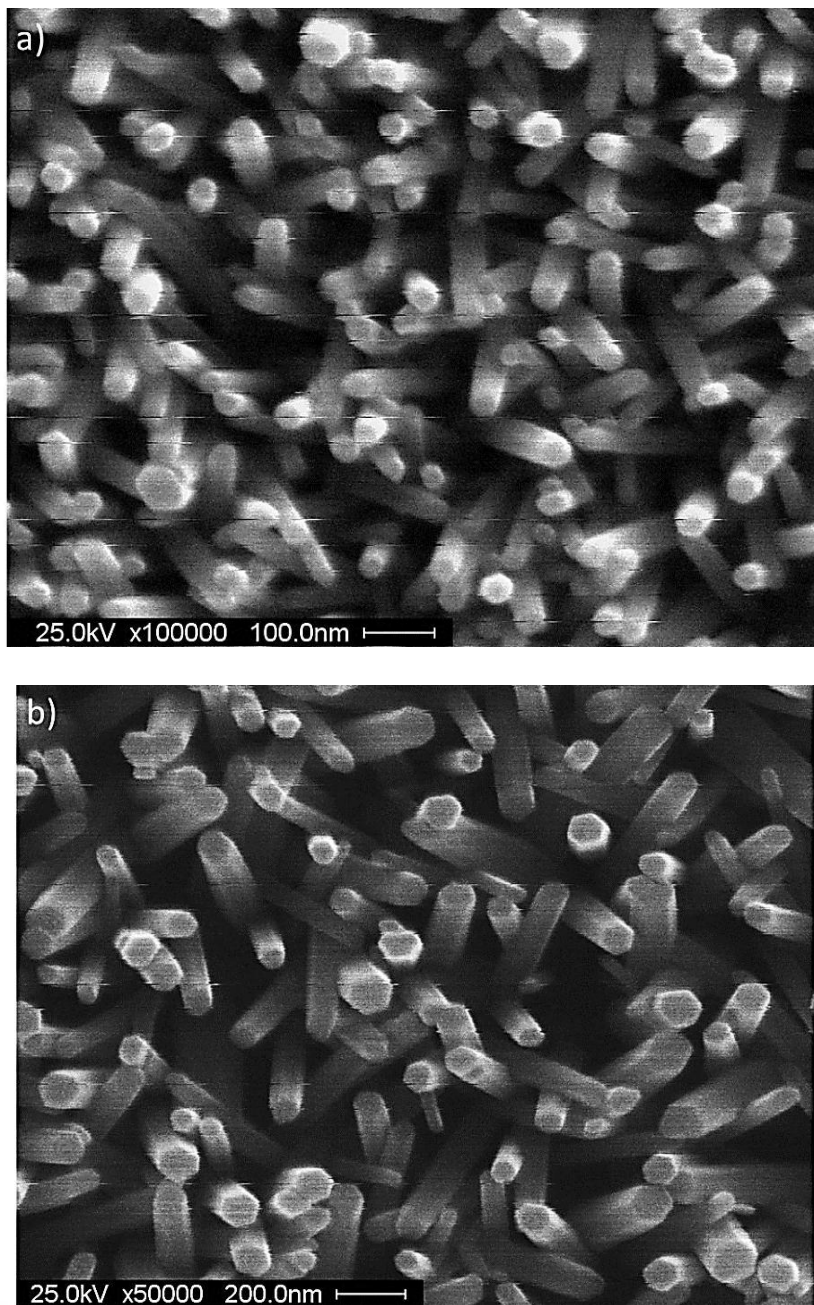


Figure 5.4 SEM images. a) ZnO nanowires and b) ZnO/Fe nanowires

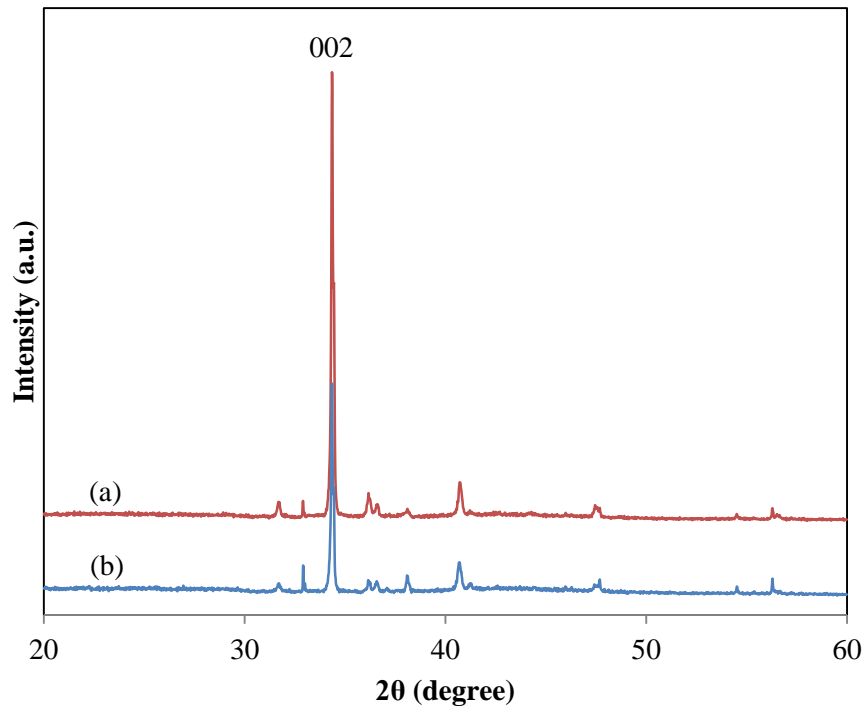


Figure 5.5 XRD spectrum. a) ZnO nanowires and b) ZnO/Fe nanowires

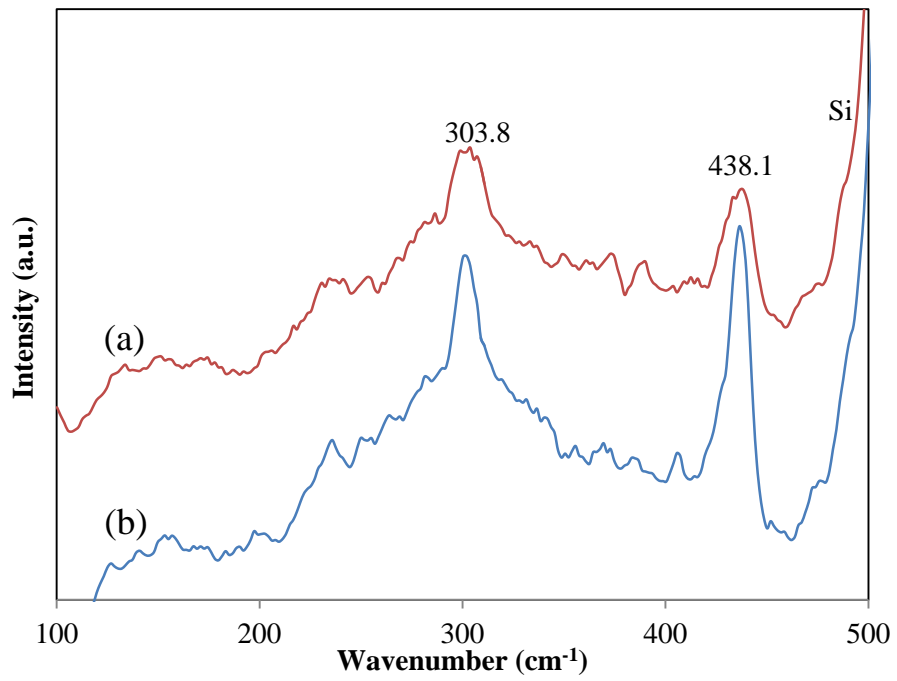


Figure 5.6 Raman spectrum. a) ZnO nanowires and b) ZnO/Fe nanowires

Figure 5.6 shows the Raman spectra of the ZnO and ZnO/Fe nanowires grown on Si substrates. The characteristic Raman bands at 303.8 and 438.1 $\text{cm}^{-1}$  were observed. The peak at 303.8  $\text{cm}^{-1}$  can be assigned to the  $2E_2$  mode due to acoustic phonons and phonon of the bulk ZnO crystal. The peak at 438 $\text{cm}^{-1}$  corresponds to the  $E_2$  mode of the ZnO oriented crystal structure. The sample of ZnO/Fe nanowires shows a higher intensity than of the ZnO nanowires because the ZnO/Fe nanowires incorporate Fe atoms.

#### 5.3.4 Photocatalysis Studies

The photocatalytic performance of ZnO and ZnO/Fe nanowires is studied for the decontamination of two representative contaminants, dichlorobenzene (DCB) and methyl orange (MO), in water. The initial concentrations of DCB and MO are kept at 10 ppm and 20 ppm, respectively. Because DCB is volatile organic compound (VOC), the molecules vaporize very easily from the water solution at room temperature. The photocatalysis testing system is not completely sealed therefore the DCB molecules could leak out from the system (Figure 5.7a control). However, we are able to compare the performance of the catalysts under similar conditions such as UV intensity, container, etc. Figure 5.7 shows the photocatalytic decontamination of DCB under: a) white light and b) UV light. The white light intensity is 60  $\text{W}/\text{m}^2$  in the visible spectrum with the addition of 2  $\text{W}/\text{m}^2$  of UV light. The intensity of UV light is 30  $\text{W}/\text{m}^2$  on the catalyst surface.

Figure 5.7 shows the enhanced photocatalytic activity of the ZnO/Fe nanowires compared to ZnO nanowires for both white light and UV light. Figure 5.7a compares the performance of the nanowires to that of P25 under white light irradiation. The ZnO nanowires exhibit similar photocatalytic activity compared to P25, while the ZnO/Fe nanowires perform even better than the P25. The catalysts expose to the UV light (Figure

5.7b) show less photocatalytic activity for ZnO than P25 nanoparticles. The ZnO/Fe nanowires reveal a similar photocatalytic activity as the TiO<sub>2</sub>. The higher photocatalytic efficiency is observed in the ZnO/Fe nanowires could be due to more surface oxygen deficiencies in the nanowires, which act as electron capture centers. In addition, the electron orbit of the Fe atom is empty in the d-orbit which could trap free electrons and thus reducing the probability of the electron/hole recombination. Both of these are able to lower the electron/hole pair recombination rate and lead to an increase in the photocatalytic efficiency compared to TiO<sub>2</sub> and ZnO. Moreover, compared to TiO<sub>2</sub> coated on a flat substrate, the one dimensional nanostructure of nanowires offers a higher surface area, which is able to facilitate adsorption of contaminants and a more effective utilization of the light source.

The mechanism of DCB degradation by photocatalysis has been proposed by Lin et al [272] and Andreozzi et al [273]. Based on them, a more detailed of mechanism is proposed in here. The photocatalyst is excited to produce hydroxyl radicals (OH•) by the absorption of light of appropriate incident wavelength. The OH• is the main oxidant to break down the DCB. The first step in the reaction is the OH• attack on the ortho or meta positions of DCB to generate 2, 3-dichlorophenol and 3, 4-dichlorophenol, respectively. The 2,3-dichlorophenol and 3,4-dichlorophenol could be nucleophilic replaced by hydroxyl ions (OH<sup>-</sup>) leading to the formation of 1,2,3-trihydroxybenzene and 1,2,4-trihydroxybenzene. The DCB could also be nucleophilic replaced by hydroxyl ions (OH<sup>-</sup>) directly to generate 2-chlorophenol or 1, 2-dihydroxybenzene. 2-chlorophenol could be attached by OH• to generate 2-chloro-1, 4-dihydroxybenzene. The 2-chloro-1, 4-dihydroxybenzene could be further nucleophilic replaced by hydroxyl ions and lead to 1,

2, 4-trihydroxybenzene generation. 1,2-dihydroxybenzene, 1,2,3-trihydroxybenzene and 1,2,4-trihydroxybenzene have been reported to be rapidly degraded by direct photolysis or photodecomposition and become  $\text{CO}_2$  and  $\text{H}_2\text{O}$  [274].

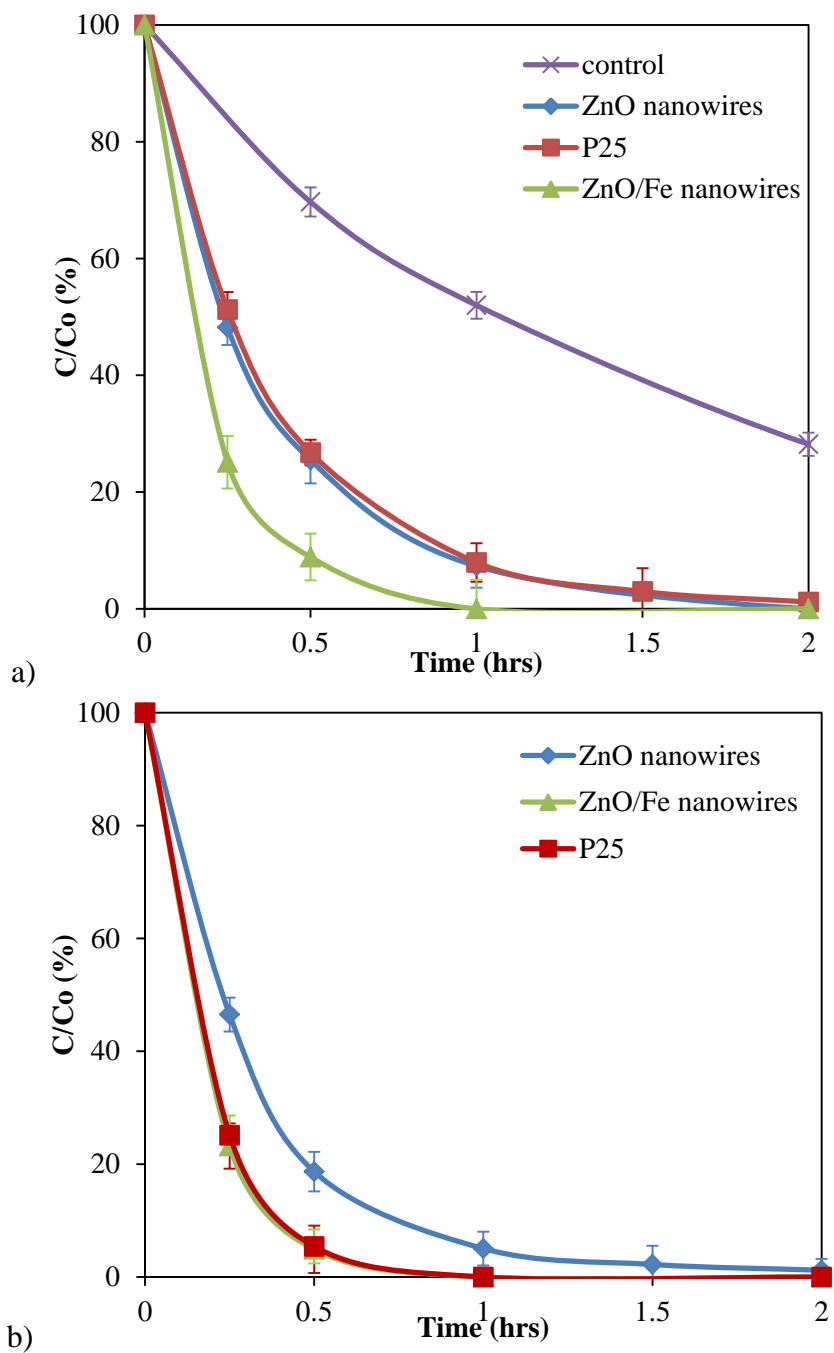


Figure 5.7 Photodegradation of DCB. a) white light irradiation b) UV irradiation



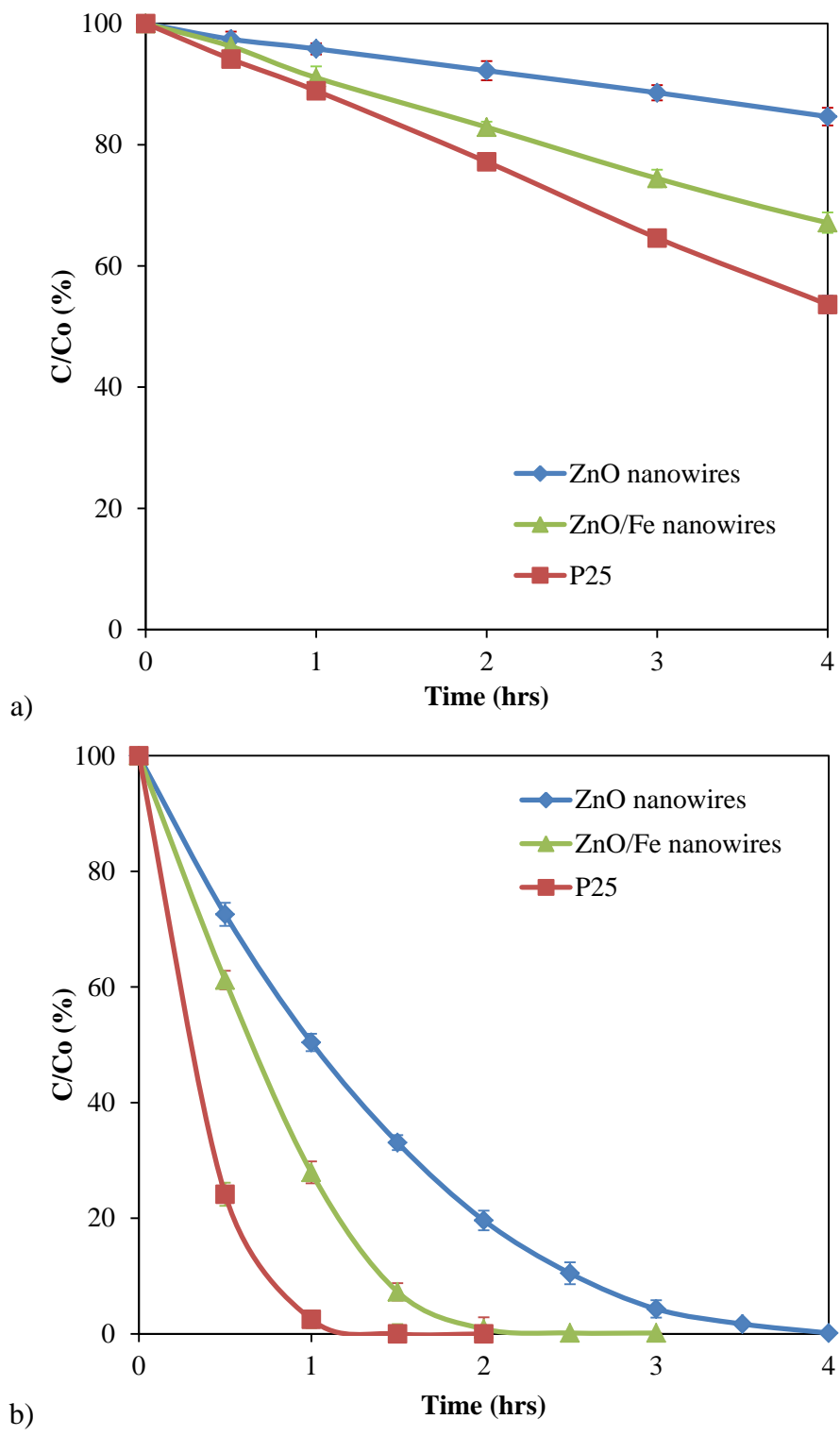


Figure 5.8 Photodegradation of MO. a) visible light irradiation and b) UV irradiation

Figure 5.8 shows the photocatalytic decoloration of MO under: a) white light and b) UV light. The light sources used are the same as those used in the DCB photodegradation experiments. Under both white light and UV light irradiation, ZnO/Fe nanowires exhibit an enhanced photocatalytic activity compared to ZnO nanowires. The results of ZnO and ZnO/Fe nanowires are similar with the DCB degradation under both white light and UV irradiation. The photocatalytic activities of ZnO and ZnO/Fe nanowires were also compared with TiO<sub>2</sub> P25. The results showed that P25 is more effective for the decolorization of MO.

The mechanism for the MO degradation by photocatalysis has been studied by Dai et al. [275] and He et al. [276]. The OH• is the main oxidant for the degradation of MO molecules in water. The OH• attaches to the aromatic ring of MO, and later finds multiple substitutions. The MO molecules could be degraded through demethylation, which is a process where the N-C bond of the amine group leads to the substitution of a methyl group with a hydrogen atom. The intermediate could be further attacked by OH• and subsequently could break into smaller molecules generating CO<sub>2</sub> and H<sub>2</sub>O at the end of the reaction.

## **CHAPTER 6: SUMMARY, CONCLUSIONS AND RECOMMENDATIONS**

The research includes three main tasks: (a) theoretical analysis of photocatalytic reactor with surface roughness for indoor air purification; (b) experimental verification of photocatalytic reactor performance with surface roughness for indoor air purification and (c) ZnO/Fe photocatalyst development. The overall goal is to develop an efficient photocatalytic reactor for indoor air purification applications.

### **6.1 Theoretical Analysis**

In a photocatalytic reactor channel, a rough catalyst surface could increase the local wall turbulence. The increased turbulence could then translate into an enhancement of mass transport to the catalyst surface, resulting in improved photocatalytic performance. The effect of different roughness patterns (shapes, sizes, arrangements, etc.) on turbulence intensity was numerically modeled. The optimum roughness patterns leading to maximum enhancement in turbulence intensity, possibly leading to maximum enhancement in photocatalytic performance, were determined. The conclusions of this study are:

1. Artificial roughness elements on a catalyst surface lead to an enhancement in turbulence intensity, resulting in increased mass transfer and improved rate of photocatalysis.

2. The optimum pitch ratio ( $p/e$ ) was determined to be 10 for all shapes of roughness elements to maximize the turbulence intensity.
3. To enhance the turbulence intensity near the catalyst surface of the photoreactor channel, a relative height ( $e/h$ ) of 0.05 was determined to be optimum for all the shapes of the roughness elements.
4. The isosceles triangle shape of roughness with a base angle equal to  $75^\circ$  was considered to be the best shape roughness element.
5. For transverse broken rib roughness arrangements, the optimum relative gap ( $g/e$ ) was determined to be 1 and the optimum relative length ( $l/e$ ) was determined to be 8~48.
6. The optimum flow angle of attack ( $\alpha$ ) was  $75^\circ$  for inclined, V shape and mesh roughness arrangements.
7. The magnitude of the turbulence intensity for various continuous roughness patterns is: V shape  $\approx$  inclined  $>$  mesh  $>$  transverse  $>$  smooth, which is also the possible order of a photocatalytic reactor performance.

Some of the recommendations for future work in the theoretical analysis of a photocatalytic reactor with surface roughness for indoor air purification are:

1. Improve the accuracy of the current model.
2. The mass transport equations maybe integrated into the current model to determine the mass transfer directly as a function of the roughness pattern.
3. The chemical surface reaction kinetics maybe integrated for modeling the degradation of air contaminants in the reactor with various rough catalyst surfaces.

4. Other roughness patterns may be modeled to further increase the potential reactor performance.
5. A different scale of reactor may be modeled for practical reactor design.

## 6.2 Experimental Study

A model photocatalytic reactor for indoor air purification was fabricated. The experimental investigation was carried out with various roughness patterns for indoor air purification to verify the theoretical analysis results. The conclusions of the study are:

1. From the study of catalyst loading, the reactor performance was greatly improved with the catalyst loading but it does not change for catalyst loading over 100 mg/plate ( $0.26 \text{ mg/cm}^2$ ).
2. The order of reactor performance for various roughness patterns was V shape > inclined > mesh > transverse > smooth, which compares well with the theoretical analysis of turbulence intensity.
3. A relationship between the overall reaction rate constant ( $k$ ) of the reactor and the turbulence intensity was found out.
4. An empirical correlation expression for the overall reaction rate constant, the turbulence intensity and the Reynolds number was proposed.

Future work in this area could use the following recommendations:

1. Other types rough patterns (like broken rib) on catalyst plates may be fabricated and studied.
2. The study could be extended to disinfection of microorganisms for a complete understanding the reactor capabilities.

3. Photocatalytic reactor performance under solar irradiation could be studied.
4. A design methodology for photocatalytic reactors for air purification may be developed.

### **6.3 Photocatalyst Development**

Iron doped zinc oxide (ZnO/Fe) nanowire photocatalyst was formulated by using hydrothermal method. The photocatalytic activities under white light and UV light irradiation were separately investigated for the degradation of dichlorobenzene (DCB) and methyl orange (MO) molecules in water. The photocatalytic activity was also compared with ZnO nanowires and Degussa P25 TiO<sub>2</sub>. The conclusions of this study are:

1. The ZnO/Fe nanowires were found to exhibit enhanced photocatalytic activity compared to ZnO nanowires regardless of the type of contaminants and light sources.
2. The ZnO/Fe nanowires exhibited enhanced photocatalytic activity under white light and a similar level of activity under UV irradiation compared to P25 TiO<sub>2</sub> in the degradation of dichlorobenzene (DCB) in water.
3. The results indicate that ZnO/Fe nanowires could be a better photocatalyst in sunlight.

A few recommendations for future work in the area of enhanced photocatalysts are:

1. Additional characterization of ZnO/Fe nanowires could be carried out to better understand the enhanced photoactivity of the ZnO/Fe nanowires.
2. Additional experimental study should be carried out to find the optimum Fe doping to increase the photocatalyst activity.

3. The study should be extended to microorganism for disinfection.
4. The photocatalytic activity of nanowires could be studied in the gas phase for detoxification and disinfection.
5. The photocatalytic activity under solar irradiation could be studied.
6. Long-term experiments could be carried out to study the effectiveness of the enhanced photocatalyst for reuse.

## REFERENCES

1. Austin BS, Greenfield SM, Weir BR, Anderson GE, Behar JV: Modeling the indoor environment. *Environmental Science & Technology* 1992, 26(5):851-858.
2. Jones AP: Indoor air quality and health. *Atmospheric Environment* 1999, 33(28):4535-4564.
3. Bernstein JA, Alexis N, Bacchus H, Bernstein IL, Fritz P, Horner E, Li N, Mason S, Nel A, Oullette J *et al*: The health effects of nonindustrial indoor air pollution. *Journal of Allergy and Clinical Immunology* 2008, 121(3).
4. Zhang YP, Yang R, Zhao RY: A model for analyzing the performance of photocatalytic air cleaner in removing volatile organic compounds. *Atmospheric Environment* 2003, 37(24):3395-3399.
5. Kabir E, Kim KH, Sohn JR, Kweon BY, Shin JH: Indoor air quality assessment in child care and medical facilities in Korea. *Environmental Monitoring and Assessment* 2012, 184(10).
6. St-Jean M, St-Amand A, Gilbert NL, Soto JC, Guay M, Davis K, Gyorkos TW: Indoor air quality in Montreal area day-care centres, Canada. *Environmental Research* 2012, 118.
7. Sundell J, Levin H, Nazaroff WW, Cain WS, Fisk WJ, Grimsrud DT, Gyntelberg F, Li Y, Persily AK, Pickering AC *et al*: Ventilation rates and health: multidisciplinary review of the scientific literature. *Indoor Air* 2011, 21(3).
8. Mendell MJ: Indoor residential chemical emissions as risk factors for-respiratory and allergic effects in children: a review. *Indoor Air* 2007, 17(4).
9. Mestl HES, Aunan K, Seip HM: Health benefits from reducing indoor air pollution from household solid fuel use in China - Three abatement scenarios. *Environment International* 2007, 33(6).
10. Fisk WJ, Rosenfeld AH: Estimates of improved productivity and health from better indoor environments. *Indoor Air-International Journal of Indoor Air Quality and Climate* 1997, 7(3).



11. World Health Report 2002, [http://www.who.int/whr/2002/en/whr02\\_en.pdf](http://www.who.int/whr/2002/en/whr02_en.pdf), World Health Organization, 1211 Geneva 27, Switzerland.
12. Vredevoogd M: Indoor air quality problems: controlling the sources visual. Vredevoogd heating and cooling; 2012.
13. Alberici RM, Jardim WE: Photocatalytic destruction of VOCs in the gas-phase using titanium dioxide. *Applied Catalysis B-Environmental* 1997, 14(1-2):55-68.
14. Darby S, Hill D, Auvinen A, Barrios-Dios JM, Baysson H, Bochicchio F, Deo H, Falk R, Forastiere F, Hakama M *et al*: Radon in homes and risk of lung cancer: collaborative analysis of individual data from 13 European case-control studies. *British Medical Journal* 2005, 330(7485).
15. Balasubramanian R, Nainar P, Rajasekar A: Airborne bacteria, fungi, and endotoxin levels in residential microenvironments: a case study. *Aerobiologia* 2012, 28(3).
16. Wang B, Mortazavi R, Haghghat F: Evaluation of Modeling and Measurement Techniques of Ultraviolet Germicidal Irradiation Effectiveness - Towards the Design of Immune Buildings. *Indoor and Built Environment* 2009, 18(2).
17. Qian H, Li Y, Sun H, Nielsen PV, Huang X, Zheng X: Particle removal efficiency of the portable HEPA air cleaner in a simulated hospital ward. *Building Simulation* 2010, 3(3).
18. Li L, Liu S, Liu J: Surface modification of coconut shell based activated carbon for the improvement of hydrophobic VOC removal. *Journal of Hazardous Materials* 2011, 192(2).
19. Kwong CW, Chao CYH, Hui KS, Wan MP: Removal of VOCs from indoor environment by ozonation over different porous materials. *Atmospheric Environment* 2008, 42(10).
20. Lee BU, Yermakov M, Grinshpun SA: Removal of fine and ultrafine particles from indoor air environments by the unipolar ion emission. *Atmospheric Environment* 2004, 38(29).
21. Vohra A, Goswami DY, Deshpande DA, Block SS: Enhanced photocatalytic disinfection of indoor air. *Applied Catalysis B-Environmental* 2006, 64(1-2):57-65.
22. Goswami DY, Trivedi DM, Block SS: Photocatalytic disinfection of indoor air. *Journal of Solar Energy Engineering-Transactions of the Asme* 1997, 119(1):92-96.

23. Hingorani S, Greist H, Goswami T, Goswami Y: Clean-up of contaminated indoor air using photocatalytic technology. In. San Antonio, TX: Proceedings of the Twelfth Symposium on Improving Building Systems in Hot and Humid Climates; 2000.
24. Srinivasan SS, Wade J, Stefanakos EK, Goswami Y: Synergistic effects of sulfation and co-doping on the visible light photocatalysis of TiO<sub>2</sub>. *Journal of Alloys and Compounds* 2006, 424(1-2):322-326.
25. Zhang H, Lv X, Li Y, Wang Y, Li J: P25-Graphene Composite as a High Performance Photocatalyst. *Acs Nano* 2010, 4(1):380-386.
26. Goswami DY: Decontamination of ventilation systems using photocatalytic air cleaning technology. *Journal of Solar Energy Engineering-Transactions of the Asme* 2003, 125(3):359-365.
27. Vohra A, Goswami DY, Deshpande DA, Block SS: Enhanced photocatalytic inactivation of bacterial spores on surfaces in air. *Journal of Industrial Microbiology & Biotechnology* 2005, 32(8):364-370.
28. Kislov N, Lahiri J, Verma H, Goswami DY, Stefanakos E, Batzill M: Photocatalytic Degradation of Methyl Orange over Single Crystalline ZnO: Orientation Dependence of Photoactivity and Photostability of ZnO. *Langmuir* 2009, 25(5):3310-3315.
29. Srinivasan S, Escobar D, Goswami Y, Stefanakos E: Effects of catalysts doping on the thermal decomposition behavior of Zn(BH<sub>4</sub>)<sub>2</sub>. *International Journal of Hydrogen Energy* 2008, 33(9):2268-2272.
30. Vijayaraghavan S, Goswami DY: Photocatalytic oxidation of toluene in water from an algae pond with high dissolved oxygen content. *Journal of Solar Energy Engineering-Transactions of the Asme* 2003, 125(2):230-232.
31. Zhong LX, Haghightat F, Blondeau P, Kozinski J: Modeling and physical interpretation of photocatalytic oxidation efficiency in indoor air applications. *Building and Environment* 2010, 45(12):2689-2697.
32. Mo J, Zhang Y, Xu Q, Lamson JJ, Zhao R: Photocatalytic purification of volatile organic compounds in indoor air: A literature review. *Atmospheric Environment* 2009, 43(14):2229-2246.
33. Salvado-Estivill I, Hargreaves DM, Puma GL: Evaluation of the intrinsic photocatalytic oxidation kinetics of indoor air pollutants. *Environmental Science & Technology* 2007, 41(6):2028-2035.

34. Queffeuilou A, Geron L, Schaer E: Prediction of photocatalytic air purifier apparatus performances with a CFD approach using experimentally determined kinetic parameters. *Chemical Engineering Science* 2010, 65(18):5067-5074.
35. Mercedes Zacarias S, Celia Vaccari M, Mario Alfano O, Antonio Irazoqui H, Eduardo Imoberdorf G: Effect of the radiation flux on the photocatalytic inactivation of spores of *Bacillus subtilis*. *Journal of Photochemistry and Photobiology B Biology* 2010, 214(2-3):171-180.
36. Yang R, Zhang Y, Xu Q, Mo J: A mass transfer based method for measuring the reaction coefficients of a photocatalyst. *Atmospheric Environment* 2007, 41(6):1221-1229.
37. Goswami DY, Kreith F, Kreider JF: Principles of solar engineering, Second edn: Taylor & Francis Group; 2000.
38. Braslavsky SE, Braun AM, Cassano AE, Emeline AV, Litter MI, Palmisano L, Parmon VN, Serpone N, Alfano OM, Anpo M *et al*: Glossary of terms used in photocatalysis and radiation catalysis (IUPAC Recommendations 2011). *Pure and Applied Chemistry* 2011, 83(4).
39. Ollis DF, Pelizzetti E, Serpone N: Photocatalyzed destruction of water contaminants. *Environmental Science and Technology* 1991, 25(9):1523-1529.
40. Saltiel C, Martin A, Goswami DY: Performance analysis of solar water detoxification systems by detailed simulation. In., vol. 1. ASME: Solar engineering; 1992.
41. Klausner JF, Goswami DY, Wyness PR: Energy consumption of wastewater treatment technologies. In., vol. 1. ASME: Solar engineering; 1992.
42. Faustini M, Nicole L, Boissiere C, Innocenzi P, Sanchez C, Grosso D: Hydrophobic, Antireflective, Self-Cleaning, and Antifogging Sol-Gel Coatings: An Example of Multifunctional Nanostructured Materials for Photovoltaic Cells. *Chemistry of Materials* 2010, 22(15).
43. Pichat P: Some views about indoor air photocatalytic treatment using TiO<sub>2</sub>: Conceptualization of humidity effects, active oxygen species, problem of C-1-C-3 carbonyl pollutants. *Applied Catalysis B-Environmental* 2010, 99(3-4):428-434.
44. Matsuoka M, Kitano M, Takeuchi M, Tsujimaru K, Anpo M, Thomas JM: Photocatalysis for new energy production - Recent advances in photocatalytic water splitting reactions for hydrogen production. *Catalysis Today* 2007, 122(1-2).
45. Tan SS, Zou L, Hu E: Photocatalytic reduction of carbon dioxide into gaseous hydrocarbon using TiO<sub>2</sub> pellets. *Catalysis Today* 2006, 115(1-4).

46. Li C, Srinivasan S, Kislov N, Schmidt M, Stefanakos L, Goswami Y: Enhancement of TiO<sub>2</sub> photocatalytic activity by N-doping using the gas phase impregnation method. In: *MRS: 2009*.
47. Vohra A: Photocatalytic disinfection of indoor air: Effect of relative humidity and surface roughness of photocatalytic reactor. University of Florida; 2005.
48. Wyness P, Klausner JF, Goswami DY, Schanze KS: Performance of nonconcentrating solar photocatalytic oxidation reactors .1. flate-plate configuration. *Journal of Solar Energy Engineering-Transactions of the Asme* 1994, 116(1):2-7.
49. Wyness P, Klausner JF, Goswami DY, Schanze KS: Performance of nonconcentrating solar photocatalytic oxidation reactors .2. shallow pond configuration. *Journal of Solar Energy Engineering-Transactions of the Asme* 1994, 116(1):8-13.
50. Zhang Y, Ram MK, Stefanakos EK, Goswami DY: Synthesis, Characterization, and Applications of ZnO Nanowires. *Journal of Nanomaterials* 2012.
51. Baruah S, Abbas M, Myint M, Bora T, Dutta J: Enhanced visible light photocatalysis through fast crystallization of zinc oxide nanorods. In., vol. 1. Beilstein journal of nanotechnology; 2010: 14-20.
52. Rehman S, Ullah R, Butt AM, Gohar ND: Strategies of making TiO<sub>2</sub> and ZnO visible light active. *Journal of Hazardous Materials* 2009, 170(2-3):560-569.
53. Chong MN, Jin B, Chow CWK, Saint C: Recent developments in photocatalytic water treatment technology: A review. *Water Research* 2010, 44(10):2997-3027.
54. Ahmed S, Rasul MG, Martens WN, Brown R, Hashib MA: Heterogeneous photocatalytic degradation of phenols in wastewater: A review on current status and developments. *Desalination* 2010, 261(1-2):3-18.
55. Mozia S: Photocatalytic membrane reactors (PMRs) in water and wastewater treatment. A review. *Separation and Purification Technology* 2010, 73(2).
56. Fogler HS: Elements of Chemical Reaction Engineering: Prentice-Hall PTR Inc; 1999.
57. Pera-Titus M, Garcia-Molina V, Banos MA, Gimenez J, Esplugas S: Degradation of chlorophenols by means of advanced oxidation processes: a general review. *Applied Catalysis B-Environmental* 2004, 47(4):219-256.
58. Carp O, Huisman CL, Reller A: Photoinduced reactivity of titanium dioxide. *Progress in Solid State Chemistry* 2004, 32(1-2):33-177.

59. Mills A, Davies RH, Worsley D: Water-purification by semiconductor photocatalysis. *Chemical Society Reviews* 1993, 22(6).
60. Linic S, Christopher P, Ingram D: Plasmonic-metal nanostructures for efficient conversion of solar to chemical energy. *Nature materials* 2011, 10:911-921.
61. Srinivasan SS, Wade J, Stefanakos EK: Synthesis and characterization of photocatalytic TiO<sub>2</sub>-ZnFe<sub>2</sub>O<sub>4</sub> nanoparticles. *Journal of Nanomaterials* 2006.
62. Bhatkhande DS, Pangarkar VG, Beenackers A: Photocatalytic degradation for environmental applications - a review. *Journal of Chemical Technology and Biotechnology* 2002, 77(1):102-116.
63. Linic S, Christopher P, Ingram D: Plasmonic-metal nanostructures for efficient conversion of solar to chemical energy. *Nature materials* 2011, 10:911-921.
64. Lee DM, Yun HJ, Yu S, Yun SJ, Lee SY, Mang SH, Yi J: Design of an efficient photocatalytic reactor for the decomposition of gaseous organic contaminants in air. *Chemical Engineering Journal* 2012, 187.
65. Fujishima A, Zhang XT: Titanium dioxide photocatalysis: present situation and future approaches. *Comptes Rendus Chimie* 2006, 9(5-6):750-760.
66. Zhao J, Yang XD: Photocatalytic oxidation for indoor air purification: a literature review. *Building and Environment* 2003, 38(5).
67. Ding Z, Lu GQ, Greenfield PF: Role of the crystallite phase of TiO<sub>2</sub> in heterogeneous photocatalysis for phenol oxidation in water. *Journal of Physical Chemistry B* 2000, 104(19).
68. Gerischer H, Heller A: Photocatalytic oxidation of organic molecules at TiO<sub>2</sub> particles by sunlight in aerated water. *Journal of the Electrochemical Society* 1992, 139(1).
69. Bickley RI, Gonzalezcarreno T, Lees JS, Palmisano L, Tilley RJD: A structural investigation of titanium-dioxide photocatalysts. *Journal of Solid State Chemistry* 1991, 92(1).
70. Tanaka K, Capule MFV, Hisanaga T: Effect of crystallinity of TiO<sub>2</sub> on its photocatalytic action. *Chemical Physics Letters* 1991, 187(1-2).
71. Bacsa RR, Kiwi J: Effect of rutile phase on the photocatalytic properties of nanocrystalline titania during the degradation of p-coumaric acid. *Applied Catalysis B-Environmental* 1998, 16(1).

72. Gummy D, Morais C, Bowen P, Pulgarin C, Giraldo S, Hajdu R, Kiwi J: Catalytic activity of commercial of TiO<sub>2</sub> powders for the abatement of the bacteria (E-coli) under solar simulated light: Influence of the isoelectric point. *Applied Catalysis B-Environmental* 2006, 63(1-2).
73. Hurum DC, Agrios AG, Gray KA, Rajh T, Thurnauer MC: Explaining the enhanced photocatalytic activity of Degussa P25 mixed-phase TiO<sub>2</sub> using EPR. *Journal of Physical Chemistry B* 2003, 107(19).
74. Malato S, Fernandez-Ibanez P, Maldonado MI, Blanco J, Gernjak W: Decontamination and disinfection of water by solar photocatalysis: Recent overview and trends. *Catalysis Today* 2009, 147(1):1-59.
75. Bahnemann W, Muneer M, Haque MM: Titanium dioxide-mediated photocatalysed degradation of few selected organic pollutants in aqueous suspensions. *Catalysis Today* 2007, 124(3-4).
76. Stark WJ, Pratsinis SE: Aerosol flame reactors for manufacture of nanoparticles. *Powder Technology* 2002, 126(2).
77. Znad H, Kawase Y: Synthesis and characterization of S-doped Degussa P25 with application in decolorization of Orange II dye as a model substrate. *Journal of Molecular Catalysis a-Chemical* 2009, 314(1-2).
78. Wu TS, Wang KX, Li GD, Sun SY, Sun J, Chen JS: Montmorillonite-Supported Ag/TiO<sub>2</sub> Nanoparticles: An Efficient Visible-Light Bacteria Photodegradation Material. *Acs Applied Materials & Interfaces* 2010, 2(2):544-550.
79. Sakthivel S, Shankar MV, Palanichamy M, Arabindoo B, Bahnemann DW, Murugesan V: Enhancement of photocatalytic activity by metal deposition: characterisation and photonic efficiency of Pt, Au and Pd deposited on TiO<sub>2</sub> catalyst. *Water Research* 2004, 38(13).
80. Herrmann JM, Tahiri H, AitIchou Y, Lassaletta G, GonzalezElipse AR, Fernandez A: Characterization and photocatalytic activity in aqueous medium of TiO<sub>2</sub> and Ag-TiO<sub>2</sub> coatings on quartz. *Applied Catalysis B-Environmental* 1997, 13(3-4).
81. Meng Y, Chen J, Wang Y, Ding H, Shan Y: (N, F)-codoped TiO<sub>2</sub> Nanocrystals as Visible Light-activated Photocatalyst. *Journal of Materials Science & Technology* 2009, 25(1).
82. Ohno T, Akiyoshi M, Umebayashi T, Asai K, Mitsui T, Matsumura M: Preparation of S-doped TiO<sub>2</sub> photocatalysts and their photocatalytic activities under visible light. *Applied Catalysis a-General* 2004, 265(1).

83. Ren W, Ai Z, Jia F, Zhang L, Fan X, Zou Z: Low temperature preparation and visible light photocatalytic activity of mesoporous carbon-doped crystalline TiO<sub>2</sub>. *Applied Catalysis B-Environmental* 2007, 69(3-4).
84. Li D, Haneda H, Labhsetwar NK, Hishita S, Ohashi N: Visible-light-driven photocatalysis on fluorine-doped TiO<sub>2</sub> powders by the creation of surface oxygen vacancies. *Chemical Physics Letters* 2005, 401(4-6).
85. Serpone N: Is the band gap of pristine TiO<sub>2</sub> narrowed by anion- and cation-doping of titanium dioxide in second-generation photocatalysts? *Journal of Physical Chemistry B* 2006, 110(48).
86. Srinivasan SS, Wade J, Stefanakos EK: Visible light photocatalysis via CdS/TiO<sub>2</sub> nanocomposite materials. *Journal of Nanomaterials* 2006.
87. Lu F, Cai W, Zhang Y: ZnO hierarchical micro/nanoarchitectures: Solvothermal synthesis and structurally enhanced photocatalytic performance. *Advanced Functional Materials* 2008, 18(7):1047-1056.
88. Jun Z, Xu N, Zhong LW: Dissolving behavior and stability of ZnO wires in biofluids: A study on biodegradability and biocompatibility of ZnO nanostructures. *Advanced Materials* 2006, 18(18):2432.
89. Chu S, Wang G, Zhou W, Lin Y, Chernyak L, Zhao J, Kong J, Li L, Ren J, Liu J: Electrically pumped waveguide lasing from ZnO nanowires. *Nature Nanotechnology* 2011, 6(8):506-510.
90. Na JH, Kitamura M, Arita M, Arakawa Y: Hybrid p-n junction light-emitting diodes based on sputtered ZnO and organic semiconductors. *Applied Physics Letters* 2009, 95(25).
91. Sudhagar P, Kumar RS, Jung JH, Cho W, Sathyamoorthy R, Won J, Kang YS: Facile synthesis of highly branched jacks-like ZnO nanorods and their applications in dye-sensitized solar cells. *Materials Research Bulletin* 2011, 46(9):1473-1479.
92. Wang ZL, Yang R, Zhou J, Qin Y, Xu C, Hu Y, Xu S: Lateral nanowire/nanobelt based nanogenerators, piezotronics and piezo-phototronics. *Materials Science & Engineering R-Reports* 2010, 70(3-6):320-329.
93. Xu J, Han J, Zhang Y, Sun Ya, Xie B: Studies on alcohol sensing mechanism of ZnO based gas sensors. *Sensors and Actuators B-Chemical* 2008, 132(1):334-339.
94. Lu C-Y, Chang S-J, Chang S-P, Lee C-T, Kuo C-F, Chang H-M, Chiou Y-Z, Hsu C-L, Chen IC: Ultraviolet photodetectors with ZnO nanowires prepared on ZnO : Ga/glass templates. *Applied Physics Letters* 2006, 89(15).

95. Cho S, Kim S, Jang J-W, Jung S-H, Oh E, Lee BR, Lee K-H: Large-Scale Fabrication of Sub-20-nm-Diameter ZnO Nanorod Arrays at Room Temperature and Their Photocatalytic Activity. *Journal of Physical Chemistry C* 2009, 113(24):10452-10458.
96. Sapkota A, Anceno AJ, Baruah S, Shipin OV, Dutta J: Zinc oxide nanorod mediated visible light photoinactivation of model microbes in water. *Nanotechnology* 2011, 22(21).
97. Ladanov M, Ram MK, Matthews G, Kumar A: Structure and Opto-electrochemical Properties of ZnO Nanowires Grown on n-Si Substrate. *Langmuir* 2011, 27(14):9012-9017.
98. Fouad DM, Mohamed MB: Comparative Study of the Photocatalytic Activity of Semiconductor Nanostructures and Their Hybrid Metal Nanocomposites on the Photodegradation of Malathion. *Journal of Nanomaterials* 2012.
99. Khodja AA, Sehili T, Pilichowski JF, Boule P: Photocatalytic degradation of 2-phenylphenol on TiO<sub>2</sub> and ZnO in aqueous suspensions. *Journal of Photochemistry and Photobiology a-Chemistry* 2001, 141(2-3):231-239.
100. Marci G, Augugliaro V, Lopez-Munoz MJ, Martin C, Palmisano L, Rives V, Schiavello M, Tilley RJD, Venezia AM: Preparation characterization and photocatalytic activity of polycrystalline ZnO/TiO<sub>2</sub> systems. 2. Surface, bulk characterization, and 4-nitrophenol photodegradation in liquid-solid regime. *Journal of Physical Chemistry B* 2001, 105(5):1033-1040.
101. Sobana N, Swaminathan M: The effect of operational parameters on the photocatalytic degradation of acid red 18 by ZnO. *Separation and Purification Technology* 2007, 56(1):101-107.
102. Wan Q, Wang TH, Zhao JC: Enhanced photocatalytic activity of ZnO nanotetrapods. *Applied Physics Letters* 2005, 87(8).
103. Kaneva NV, Dimitrov DT, Dushkin CD: Effect of nickel doping on the photocatalytic activity of ZnO thin films under UV and visible light. *Applied Surface Science* 2011, 257(18):8113-8120.
104. Sakthivel S, Neppolian B, Shankar MV, Arabindoo B, Palanichamy M, Murugesan V: Solar photocatalytic degradation of azo dye: comparison of photocatalytic efficiency of ZnO and TiO<sub>2</sub>. *Solar Energy Materials and Solar Cells* 2003, 77(1):65-82.
105. Baruah S, Rafique RF, Dutta J: Visible light photocatalysis by tailoring crystal defects in zinc oxide nanostructures. *Nano* 2008, 3(5):399-407.



106. Yi GC, Wang CR, Park WI: ZnO nanorods: synthesis, characterization and applications. *Semiconductor Science and Technology* 2005, 20(4):S22-S34.
107. Petersen EW, Likovich EM, Russell KJ, Narayanamurti V: Growth of ZnO nanowires catalyzed by size-dependent melting of Au nanoparticles. *Nanotechnology* 2009, 20(40).
108. Protasova LN, Rebrov EV, Choy KL, Pung SY, Engels V, Cabaj M, Wheatley AEH, Schouten JC: ZnO based nanowires grown by chemical vapour deposition for selective hydrogenation of acetylene alcohols. *Catalysis Science & Technology* 2011, 1(5):768-777.
109. Ashraf S, Jones AC, Bacsa J, Steiner A, Chalker PR, Beahan P, Hindley S, Odedra R, Williams PA, Heys PN: MOCVD of Vertically Aligned ZnO Nanowires Using Bidentate Ether Adducts of Dimethylzinc. *Chemical Vapor Deposition* 2011, 17(1-3):45-53.
110. Wang LS, Zhang XZ, Zhao SQ, Zhou GY, Zhou YL, Qi JJ: Synthesis of well-aligned ZnO nanowires by simple physical vapor deposition on c-oriented ZnO thin films without catalysts or additives. *Applied Physics Letters* 2005, 86(2).
111. Wang JS, Yang CS, Chen PI, Su CF, Chen WJ, Chiu KC, Chou WC: Catalyst-free highly vertically aligned ZnO nanoneedle arrays grown by plasma-assisted molecular beam epitaxy. *Applied Physics a-Materials Science & Processing* 2009, 97(3):553-557.
112. Tien LC, Pearton SJ, Norton DP, Ren F: Synthesis and microstructure of vertically aligned ZnO nanowires grown by high-pressure-assisted pulsed-laser deposition. *Journal of Materials Science* 2008, 43(21):6925-6932.
113. Kitamura K, Yatsui T, Ohtsu M, Yi GC: Fabrication of vertically aligned ultrafine ZnO nanorods using metal-organic vapor phase epitaxy with a two-temperature growth method. *Nanotechnology* 2008, 19(17).
114. Suh D-I, Byeon CC, Lee C-L: Synthesis and optical characterization of vertically grown ZnO nanowires in high crystallinity through vapor-liquid-solid growth mechanism. *Applied Surface Science* 2010, 257(5):1454-1456.
115. Wang XD, Song JH, Li P, Ryou JH, Dupuis RD, Summers CJ, Wang ZL: Growth of uniformly aligned ZnO nanowire heterojunction arrays on GaN, AlN, and Al<sub>0.5</sub>Ga<sub>0.5</sub>N substrates. *Journal of the American Chemical Society* 2005, 127(21):7920-7923.
116. Song JH, Wang XD, Riedo E, Wang ZL: Systematic study on experimental conditions for large-scale growth of aligned ZnO nanowires on nitrides. *Journal of Physical Chemistry B* 2005, 109(20):9869-9872.

117. Wang XD, Song JH, Summers CJ, Ryou JH, Li P, Dupuis RD, Wang ZL: Density-controlled growth of aligned ZnO nanowires sharing a common contact: A simple, low-cost, and mask-free technique for large-scale applications. *Journal of Physical Chemistry B* 2006, 110(15):7720-7724.
118. Chu F-H, Huang C-W, Hsin C-L, Wang C-W, Yu S-Y, Yeh P-H, Wu W-W: Well-aligned ZnO nanowires with excellent field emission and photocatalytic properties. *Nanoscale* 2012, 4(5):1471-1475.
119. Hindley S, Jones AC, Ashraf S, Bacsa J, Steiner A, Chalker PR, Beahan P, Williams PA, Odedra R: Metal Organic Chemical Vapour Deposition of Vertically Aligned ZnO Nanowires Using Oxygen Donor Adducts. *Journal of Nanoscience and Nanotechnology* 2011, 11(9):8294-8301.
120. Huang MH, Wu YY, Feick H, Tran N, Weber E, Yang PD: Catalytic growth of zinc oxide nanowires by vapor transport. *Advanced Materials* 2001, 13(2):113-116.
121. Zeng YJ, Ye ZZ, Xu WZ, Zhu LP, Zhao BH: Well-aligned ZnO nanowires grown on Si substrate via metal-organic chemical vapor deposition. *Applied Surface Science* 2005, 250(1-4):280-283.
122. Zhang B, Zhou S, Liu B, Gong H, Zhang X: Fabrication and green emission of ZnO nanowire arrays. *Science in China Series E-Technological Sciences* 2009, 52(4):883-887.
123. Kim J-Y, Cho JW, Kim SH: The characteristic of the ZnO nanowire morphology grown by the hydrothermal method on various surface-treated seed layers. *Materials Letters* 2011, 65(8):1161-1164.
124. Song J, Baek S, Lee H, Lim S: Selective Growth of Vertical ZnO Nanowires with the Control of Hydrothermal Synthesis and Nano-Imprint Technology. *Journal of Nanoscience and Nanotechnology* 2009, 9(6):3909-3913.
125. Baruah S, Dutta J: Hydrothermal growth of ZnO nanostructures. *Science and Technology of Advanced Materials* 2009, 10(1).
126. Sugunan A, Warad HC, Boman M, Dutta J: Zinc oxide nanowires in chemical bath on seeded substrates: Role of hexamine. *Journal of Sol-Gel Science and Technology* 2006, 39(1):49-56.
127. Weintraub B, Zhou Z, Li Y, Deng Y: Solution synthesis of one-dimensional ZnO nanomaterials and their applications. *Nanoscale* 2010, 2(9):1573-1587.

128. Xu S, Lao C, Weintraub B, Wang ZL: Density-controlled growth of aligned ZnO nanowire arrays by seedless chemical approach on smooth surfaces. *Journal of Materials Research* 2008, 23(8):2072-2077.
129. Greene LE, Law M, Tan DH, Montano M, Goldberger J, Somorjai G, Yang PD: General route to vertical ZnO nanowire arrays using textured ZnO seeds. *Nano Letters* 2005, 5(7):1231-1236.
130. Baruah S, Dutta J: Effect of seeded substrates on hydrothermally grown ZnO nanorods. *Journal of Sol-Gel Science and Technology* 2009, 50(3):456-464.
131. Ghayour H, Rezaie HR, Mirdamadi S, Nourbakhsh AA: The effect of seed layer thickness on alignment and morphology of ZnO nanorods. *Vacuum* 2011, 86(1):101-105.
132. Wu W-Y, Yeh C-C, Ting J-M: Effects of Seed Layer Characteristics on the Synthesis of ZnO Nanowires. *Journal of the American Ceramic Society* 2009, 92(11):2718-2723.
133. Kenanakis G, Vernardou D, Koudoumas E, Katsarakis N: Growth of c-axis oriented ZnO nanowires from aqueous solution: The decisive role of a seed layer for controlling the wires' diameter. *Journal of Crystal Growth* 2009, 311(23-24):4799-4804.
134. Ji L-W, Peng S-M, Wu J-S, Shih W-S, Wu C-Z, Tang IT: Effect of seed layer on the growth of well-aligned ZnO nanowires. *Journal of Physics and Chemistry of Solids* 2009, 70(10):1359-1362.
135. Tian J-H, Hu J, Li S-S, Zhang F, Liu J, Shi J, Li X, Tian Z-Q, Chen Y: Improved seedless hydrothermal synthesis of dense and ultralong ZnO nanowires. *Nanotechnology* 2011, 22(24).
136. Al-Harbi T: Hydrothermal synthesis and optical properties of Ni doped ZnO hexagonal nanodiscs. *Journal of Alloys and Compounds* 2011, 509(2):387-390.
137. Wang JM, Gao L: Wet chemical synthesis of ultralong and straight single-crystalline ZnO nanowires and their excellent UV emission properties. *Journal of Materials Chemistry* 2003, 13(10):2551-2554.
138. Gong L, Wu X, Chen H, Qu F, An M: Synthesis of Vertically Aligned Dense ZnO Nanowires. *Journal of Nanomaterials* 2011.
139. Hu H, Huang X, Deng C, Chen X, Qian Y: Hydrothermal synthesis of ZnO nanowires and nanobelts on a large scale. *Materials Chemistry and Physics* 2007, 106(1):58-62.

140. Govender K, Boyle DS, Kenway PB, O'Brien P: Understanding the factors that govern the deposition and morphology of thin films of ZnO from aqueous solution. *Journal of Materials Chemistry* 2004, 14(16):2575-2591.
141. Ashfold MNR, Doherty RP, Ndifor-Angwafor NG, Riley DJ, Sun Y: The kinetics of the hydrothermal growth of ZnO nanostructures. *Thin Solid Films* 2007, 515(24):8679-8683.
142. Wang S-F, Tseng T-Y, Wang Y-R, Wang C-Y, Lu H-C, Shih W-L: Effects of preparation conditions on the growth of ZnO nanorod arrays using aqueous solution method. *International Journal of Applied Ceramic Technology* 2008, 5(5):419-429.
143. Kim AR, Lee J-Y, Jang BR, Lee JY, Kim HS, Jang NW: Effect of Zn(2+) Source Concentration on Hydrothermally Grown ZnO Nanorods. *Journal of Nanoscience and Nanotechnology* 2011, 11(7):6395-6399.
144. Yuan Z, Yu J, Wang N, Jiang Y: Well-aligned ZnO nanorod arrays from diameter-controlled growth and their application in inverted polymer solar cell. *Journal of Materials Science-Materials in Electronics* 2011, 22(11):1730-1735.
145. Law M, Greene LE, Johnson JC, Saykally R, Yang PD: Nanowire dye-sensitized solar cells. *Nature Materials* 2005, 4(6):455-459.
146. Baruah S, Dutta J: pH-dependent growth of zinc oxide nanorods. *Journal of Crystal Growth* 2009, 311(8):2549-2554.
147. Akhavan O, Mehrabian M, Mirabbaszadeh K, Azimirad R: Hydrothermal synthesis of ZnO nanorod arrays for photocatalytic inactivation of bacteria. *Journal of Physics D-Applied Physics* 2009, 42(22).
148. Kim MK, Yi DK, Paik U: Tunable, Flexible Antireflection Layer of ZnO Nanowires Embedded in PDMS. *Langmuir* 2010, 26(10):7552-7554.
149. Li L, Zhai T, Zeng H, Fang X, Bando Y, Golberg D: Polystyrene sphere-assisted one-dimensional nanostructure arrays: synthesis and applications. *Journal of Materials Chemistry* 2011, 21(1):40-56.
150. Lee CY, Li SY, Lin P, Tseng TY: ZnO nanowires hydrothermally grown on PET polymer substrates and their characteristics. *Journal of Nanoscience and Nanotechnology* 2005, 5(7):1088-1094.
151. Baruah S, Thanachayanont C, Dutta J: Growth of ZnO nanowires on nonwoven polyethylene fibers. *Science and Technology of Advanced Materials* 2008, 9(2).

152. Qin Y, Wang X, Wang ZL: Microfibre-nanowire hybrid structure for energy scavenging. *Nature* 2008, 451(7180):809-U805.
153. Liu TY, Liao HC, Lin CC, Hu SH, Chen SY: Biofunctional ZnO nanorod arrays grown on flexible substrates. *Langmuir* 2006, 22(13):5804-5809.
154. Ahn H, Park J-H, Kim S-B, Jee SH, Yoon YS, Kim D-J: Vertically Aligned ZnO Nanorod Sensor on Flexible Substrate for Ethanol Gas Monitoring. *Electrochemical and Solid State Letters* 2010, 13(11):J125-J128.
155. Baruah S, Jaisai M, Imani R, Nazhad MM, Dutta J: Photocatalytic paper using zinc oxide nanorods. *Science and Technology of Advanced Materials* 2010, 11(5).
156. Afsal M, Chen L-J: Anomalous adhesive superhydrophobicity on aligned ZnO nanowire arrays grown on a lotus leaf. *Journal of Materials Chemistry* 2011, 21(44):18061-18066.
157. Zhou Y, Wu W, Hu G, Wu H, Cui S: Hydrothermal synthesis of ZnO nanorod arrays with the addition of polyethyleneimine. *Materials Research Bulletin* 2008, 43(8-9):2113-2118.
158. Chen L-Y, Yin Y-T, Chen C-H, Chiou J-W: Influence of Polyethyleneimine and Ammonium on the Growth of ZnO Nanowires by Hydrothermal Method. *Journal of Physical Chemistry C* 2011, 115(43):20913-20919.
159. Hassan JJ, Hassan Z, Abu-Hassan H: High-quality vertically aligned ZnO nanorods synthesized by microwave-assisted CBD with ZnO-PVA complex seed layer on Si substrates. *Journal of Alloys and Compounds* 2011, 509(23):6711-6719.
160. Zhang L, Zhu Y-J: ZnO micro- and nano-structures: microwave-assisted solvothermal synthesis, morphology control and photocatalytic properties. *Applied Physics a-Materials Science & Processing* 2009, 97(4):847-852.
161. Unalan HE, Hiralal P, Rupesinghe N, Dalal S, Milne WI, Amaratunga GAJ: Rapid synthesis of aligned zinc oxide nanowires. *Nanotechnology* 2008, 19(25).
162. Zhang K-Z, Lin B-Z, Chen Y-L, Xu B-H, Pian X-T, Kuang J-D, Li B: Fe-doped and ZnO-pillared titanates as visible-light-driven photocatalysts. *Journal of Colloid and Interface Science* 2011, 358(2):360-368.
163. Wang B, Shan X, Fu Q, Iqbal J, Yan L, Fu H, Yu D: Photoluminescence properties of Co-doped ZnO nanorods array fabricated by the solution method. *Physica E-Low-Dimensional Systems & Nanostructures* 2009, 41(3):413-417.

164. Li Y, Zhao X, Fan W: Structural, Electronic, and Optical Properties of Ag-Doped ZnO Nanowires: First Principles Study. *Journal of Physical Chemistry C* 2011, 115(9):3552-3557.
165. Li Q, Li YW, Wu PG, Xie RC, Shang JK: Palladium Oxide Nanoparticles on Nitrogen-Doped Titanium Oxide: Accelerated Photocatalytic Disinfection and Post-Illumination Catalytic "Memory". *Advanced Materials* 2008, 20(19):3717-3723.
166. Wu C, Shen L, Zhang Y-C, Huang Q: Solvothermal synthesis of Cr-doped ZnO nanowires with visible light-driven photocatalytic activity. *Materials Letters* 2011, 65(12):1794-1796.
167. Lu Y, Lin Y, Wang D, Wang L, Xie T, Jiang T: A high performance cobalt-doped ZnO visible light photocatalyst and its photogenerated charge transfer properties. *Nano Research* 2011, 4(11):1144-1152.
168. Jia T, Wang W, Long F, Fu Z, Wang H, Zhang Q: Fabrication, characterization and photocatalytic activity of La-doped ZnO nanowires. *Journal of Alloys and Compounds* 2009, 484(1-2):410-415.
169. Wu JM, Fang C-W, Lee L-T, Yeh H-H, Lin Y-H, Yeh P-H, Tsai L-N, Lin L-J: Photoresponsive and Ultraviolet to Visible-Light Range Photocatalytic Properties of ZnO:Sb Nanowires. *Journal of the Electrochemical Society* 2011, 158(1):K6-K10.
170. Wu C, Shen L, Yu H, Huang Q, Zhang YC: Synthesis of Sn-doped ZnO nanorods and their photocatalytic properties. *Materials Research Bulletin* 2011, 46(7):1107-1112.
171. Wu C, Huang Q: Synthesis of Na-doped ZnO nanowires and their photocatalytic properties. *Journal of Luminescence* 2010, 130(11):2136-2141.
172. Jung S, Yong K: Fabrication of CuO-ZnO nanowires on a stainless steel mesh for highly efficient photocatalytic applications. *Chemical Communications* 2011, 47(9):2643-2645.
173. Obee TN: Photooxidation of sub-parts-per-million toluene and formaldehyde levels on titania using a glass-plate reactor. *Environmental Science & Technology* 1996, 30(12).
174. Hossain MM, Raupp GB, Hay SO, Obee TN: Three-dimensional developing flow model for photocatalytic monolith reactors. *Aiche Journal* 1999, 45(6):1309-1321.

175. Choi W, Ko JY, Park H, Chung JS: Investigation on TiO<sub>2</sub>-coated optical fibers for gas-phase photocatalytic oxidation of acetone. *Applied Catalysis B-Environmental* 2001, 31(3).
176. Dibble LA, Raupp GB: Fluidized-bed photocatalytic oxidation of trichloroethylene in contaminated airstreams. *Environmental Science & Technology* 1992, 26(3):492-495.
177. Larson SA, Widegren JA, Falconer JL: Transient studies of 2-propanol photocatalytic oxidation on titania. *Journal of Catalysis* 1995, 157(2):611-625.
178. Obee TN, Brown RT: TiO<sub>2</sub> photocatalysis for indoor air applications – effects of humidity and trace contaminant levels on the oxidation rates of formaldehyde, toluene, and 1,3-butadiene. *Environmental Science & Technology* 1995, 29(5):1223-1231.
179. Riffat SB, Zhao X: Preliminary study of the performance and operating characteristics of a mop-fan air cleaning system for buildings. *Building and Environment* 2007, 42(9):3241-3252.
180. Maira AJ, Lau WN, Lee CY, Yue PL, Chan CK, Yeung KL: Performance of a membrane-catalyst for photocatalytic oxidation of volatile organic compounds. *Chemical Engineering Science* 2003, 58(3-6).
181. Obee TN, Hay SO: Effects of moisture and temperature on the photooxidation of ethylene on Titania. *Environmental Science & Technology* 1997, 31(7).
182. Imoberdorf GE, Irazoqui HA, Cassano AE, Alfano OM: Photocatalytic degradation of tetrachloroethylene in gas phase on TiO<sub>2</sub> films: A kinetic study. *Industrial & Engineering Chemistry Research* 2005, 44(16).
183. Yang R, Zhang YP, Zhao RY: An improved model for analyzing the performance of photocatalytic oxidation reactors in removing volatile organic compounds and its application. *Journal of the Air & Waste Management Association* 2004, 54(12).
184. Puddu V, Choi H, Dionysiou DD, Puma GL: TiO<sub>2</sub> photocatalyst for indoor air remediation: Influence of crystallinity, crystal phase, and UV radiation intensity on trichloroethylene degradation. *Applied Catalysis B-Environmental* 2010, 94(3-4).
185. Tang F, Yang X: A "deactivation" kinetic model for predicting the performance of photocatalytic degradation of indoor toluene, o-xylene, and benzene. *Building and Environment* 2012, 56.

186. Eliyas A, Kumbilieva K, Iliev V, Rakovsky S: Transferring concepts from classical catalysis to the new field of photocatalysis. *Reaction Kinetics Mechanisms and Catalysis* 2011, 102(2).
187. Salvado-Estivill I, Brucato A, Puma GL: Two-dimensional Modeling of a flat-plate photocatalytic reactor for oxidation of indoor air pollutants. *Industrial & Engineering Chemistry Research* 2007, 46(23).
188. Mo J, Zhang Y, Xu Q, Zhu Y, Lamson JJ, Zhao R: Determination and risk assessment of by-products resulting from photocatalytic oxidation of toluene. *Applied Catalysis B-Environmental* 2009, 89(3-4).
189. Lin CY, Li CS: Inactivation of microorganisms on the photocatalytic surfaces in air. *Aerosol Science and Technology* 2003, 37(12).
190. Wayne DM: Direct determination of trace noble metals (palladium, platinum and rhodium) in automobile catalysts by glow discharge mass spectrometry. *Journal of Analytical Atomic Spectrometry* 1997, 12(10).
191. Li L, Zhang F, Guan N: Ir/ZSM-5/cordierite monolith for catalytic NO<sub>x</sub> reduction from automobile exhaust. *Catalysis Communications* 2008, 9(3).
192. Sauer ML, Ollis DF: Acetone oxidation in a photocatalytic monolith reactor. *Journal of Catalysis* 1994, 149(1).
193. Zhong L, Haghghat F: Modeling and validation of a photocatalytic oxidation reactor for indoor environment applications. *Chemical Engineering Science* 2011, 66(23).
194. Sun RD, Nakajima A, Watanabe I, Watanabe T, Hashimoto K: TiO<sub>2</sub>-coated optical fiber bundles used as a photocatalytic filter for decomposition of gaseous organic compounds. *Journal of Photochemistry and Photobiology a-Chemistry* 2000, 136(1-2).
195. Wang W, Ku Y: Photocatalytic degradation of gaseous benzene in air streams by using an optical fiber photoreactor. *Journal of Photochemistry and Photobiology a-Chemistry* 2003, 159(1).
196. Lim TH, Jeong SM, Kim SD, Gyenis J: Photocatalytic decomposition of NO by TiO<sub>2</sub> particles. *Journal of Photochemistry and Photobiology a-Chemistry* 2000, 134(3).
197. Zhang M, An T, Fu J, Sheng G, Wang X, Hu X, Ding X: Photocatalytic degradation of mixed gaseous carbonyl compounds at low level on adsorptive TiO<sub>2</sub>/SiO<sub>2</sub> photocatalyst using a fluidized bed reactor. *Chemosphere* 2006, 64(3).



198. Lim TY, Kim SD: Photocatalytic degradation of trichloroethylene over TiO<sub>2</sub>/SiO<sub>2</sub> in an annulus fluidized bed reactor. *Korean Journal of Chemical Engineering* 2002, 19(6).
199. Jacoby WA, Blake DM, Fennell JA, Boulter JE, Vargo LM, George MC, Dolberg SK: Heterogeneous photocatalysis for control of volatile organic compounds in indoor air. *Journal of the Air & Waste Management Association* 1996, 46(9).
200. Tang C, Chen V: The photocatalytic degradation of reactive black 5 using TiO<sub>2</sub>/UV in an annular photoreactor. *Water Research* 2004, 38(11).
201. Pillai UR, Sahle-Demessie E: Selective oxidation of alcohols in gas phase using light-activated titanium dioxide. *Journal of Catalysis* 2002, 211(2).
202. Jovic F, Kosar V, Tomasic V, Gomzi Z: Non-ideal flow in an annular photocatalytic reactor. *Chemical Engineering Research & Design* 2012, 90(9).
203. Palau J, Colomer M, Penya-Roja JM, Martinez-Soria V: Photodegradation of Toluene, m-Xylene, and n-Butyl Acetate and Their Mixtures over TiO<sub>2</sub> Catalyst on Glass Fibers. *Industrial & Engineering Chemistry Research* 2012, 51(17).
204. Assadi AA, Bouzaza A, Wolbert D: Photocatalytic oxidation of trimethylamine and isovaleraldehyde in an annular reactor: Influence of the mass transfer and the relative humidity. *Journal of Photochemistry and Photobiology a-Chemistry* 2012, 236.
205. Paz Y: Application of TiO<sub>2</sub> photocatalysis for air treatment: Patents' overview. *Applied Catalysis B-Environmental* 2010, 99(3-4).
206. Queffeuilou A, Geron L, Archambeau C, Le Gall H, Marquaire PM, Zahraa O: Kinetic Study of Acetaldehyde Photocatalytic Oxidation with a Thin Film of TiO<sub>2</sub> Coated on Stainless Steel and CFD Modeling Approach. *Industrial & Engineering Chemistry Research* 2010, 49(15):6890-6897.
207. Chong SH, Wang SB, Tade M, Ang HM, Pareek V: Simulations of Photodegradation of Toluene and Formaldehyde in a Monolith Reactor Using Computational Fluid Dynamics. *Aiche Journal* 2011, 57(3):724-734.
208. Selishchev DS, Kolinko PA, Kozlov DV: Adsorbent as an essential participant in photocatalytic processes of water and air purification: Computer simulation study. *Applied Catalysis a-General* 2010, 377(1-2):140-149.
209. Li C, Deng BQ, Kim CN: A numerical prediction on the reduction of microorganisms with UV disinfection. *Journal of Mechanical Science and Technology* 2010, 24(7):1465-1473.

210. Zacarias SM, Vaccari MC, Alfano OM, Irazoqui HA, Imoberdorf GE: Effect of the radiation flux on the photocatalytic inactivation of spores of *Bacillus subtilis*. *Journal of Photochemistry and Photobiology a-Chemistry* 2010, 214(2-3):171-180.
211. Duran JE, Taghipour F, Mohseni M: Irradiance modeling in annular photoreactors using the finite-volume method. *Journal of Photochemistry and Photobiology a-Chemistry* 2010, 215(1):81-89.
212. Pareek V, Chong SH, Tade M, Adesina AA: Light intensity distribution in heterogenous photocatalytic reactors. *Asia-Pacific Journal of Chemical Engineering* 2008, 3(2):171-201.
213. Duran JE, Mohseni M, Taghipour F: Modeling of annular reactors with surface reaction using computational fluid dynamics (CFD). *Chemical Engineering Science* 2010, 65(3):1201-1211.
214. Daisey JM, Angell WJ, Apte MG: Indoor air quality, ventilation and health symptoms in schools: an analysis of existing information. *Indoor Air* 2003, 13(1).
215. Lee SC, Guo H, Li WM, Chan LY: Inter-comparison of air pollutant concentrations in different indoor environments in Hong Kong. *Atmospheric Environment* 2002, 36(12).
216. Asahi R, Morikawa T, Ohwaki T, Aoki K, Taga Y: Visible-light photocatalysis in nitrogen-doped titanium oxides. *Science* 2001, 293(5528):269-271.
217. Li Q, Li YW, Wu PG, Xie RC, Shang JK: Palladium Oxide Nanoparticles on Nitrogen-Doped Titanium Oxide: Accelerated Photocatalytic Disinfection and Post-Illumination Catalytic "Memory". *Advanced Materials* 2008, 20(19):3717.
218. Ohno T, Mitsui T, Matsumura M: Photocatalytic activity of S-doped TiO<sub>2</sub> photocatalyst under visible light. *Chemistry Letters* 2003, 32(4).
219. Irie H, Watanabe Y, Hashimoto K: Carbon-doped anatase TiO<sub>2</sub> powders as a visible-light sensitive photocatalyst. *Chemistry Letters* 2003, 32(8).
220. Cassano AE, Martin CA, Brandi RJ, Alfano OM: Photoreactor analysis and design – fundamentals and applications. *Industrial & Engineering Chemistry Research* 1995, 34(7):2155-2201.
221. Gaya UI, Abdullah AH: Heterogeneous photocatalytic degradation of organic contaminants over titanium dioxide: A review of fundamentals, progress and problems. *Journal of Photochemistry and Photobiology C-Photochemistry Reviews* 2008, 9(1):1-12.

222. Yu H, Zhang K, Rossi C: Experimental study of the photocatalytic degradation of formaldehyde in indoor air using a nano-particulate titanium dioxide photocatalyst. *Indoor and Built Environment* 2007, 16(6):529-537.
223. Sano T, Negishi N, Takeuchi K, Matsuzawa S: Degradation of toluene and acetaldehyde with Pt-loaded TiO<sub>2</sub> catalyst and parabolic trough concentrator. *Solar Energy* 2004, 77(5):543-552.
224. Chang CP, Chen JN, Lu MC: Heterogeneous photocatalytic oxidation of acetone for air purification by near UV-irradiated titanium dioxide. *Journal of Environmental Science and Health Part a-Toxic/Hazardous Substances & Environmental Engineering* 2003, 38(6).
225. Ao CH, Lee SC, Yu JZ, Xu JH: Photodegradation of formaldehyde by photocatalyst TiO<sub>2</sub>: effects on the presences of NO, SO<sub>2</sub> and VOCs. *Applied Catalysis B-Environmental* 2004, 54(1):41-50.
226. Chen F, Yang X, Mak HKC, Chan DWT: Photocatalytic oxidation for antimicrobial control in built environment: A brief literature overview. *Building and Environment* 2010, 45(8).
227. Bird RB, E.Stewart W, Lightfoot NE: Transport Phenomena. In., Second Edition edn; 2006.
228. Serpone N, Emeline AV: Suggested terms and definitions in photocatalysis and radiocatalysis. *International Journal of Photoenergy* 2002, 4(3).
229. Mo J, Zhang Y, Yang R: Novel insight into VOC removal performance of photocatalytic oxidation reactors. *Indoor Air* 2005, 15(4):291-300.
230. Bouzaza A, Vallet C, Laplanche A: Photocatalytic degradation of some VOCs in the gas phase using an annular flow reactor - Determination of the contribution of mass transfer and chemical reaction steps in the photodegradation process. *Journal of Photochemistry and Photobiology a-Chemistry* 2006, 177(2-3).
231. Krishnan J, Swaminathan T: Kinetic modeling of a photocatalytic reactor designed for removal of gas-phase benzene: a study on limiting resistances using design of experiments. *Latin American Applied Research* 2010, 40(4).
232. Passalia C, Martinez Retamar ME, Alfano OM, Brandi RJ: Photocatalytic Degradation of Formaldehyde in Gas Phase on TiO<sub>2</sub> Films: A Kinetic Study. *International Journal of Chemical Reactor Engineering* 2010, 8.
233. Birnie M, Gillott M, Riffat S: Incorporating mass transfer theory to model continuous flow type photocatalytic reactors for integration into novel low energy ventilation systems. *Journal of the Energy Institute* 2006, 79(3).

234. Chen Q, Meng J-a: Field synergy analysis and optimization of the convective mass transfer in photocatalytic oxidation reactors. *International Journal of Heat and Mass Transfer* 2008, 51(11-12).
235. Perry AE, Schofiel.Wh, Joubert PN: Rough wall turbulent boundary layers. *Journal of Fluid Mechanics* 1969, 37:383
236. Antonia RA, Luxton RE: Response of a turbulent boundary layer to an upstanding step change in surface roughness. *Journal of Basic Engineering* 1971, 93(1):22
237. Hanjalic K, Launder BE: Fully developed asymmetric flow in a plane channel. *Journal of Fluid Mechanics* 1972, 51(JAN25):301
238. Cui J, Patel VC, Lin CL: Large-eddy simulation of turbulent flow in a channel with rib roughness. *International Journal of Heat and Fluid Flow* 2003, 24(3):372-388.
239. Krogstad PA, Andersson HI, Bakken OM, Ashrafiyan A: An experimental and numerical study of channel flow with rough walls. *Journal of Fluid Mechanics* 2005, 530.
240. Bhaganagar K, Kim J, Coleman G: Effect of roughness on wall-bounded turbulence. *Flow Turbulence and Combustion* 2004, 72(2-4).
241. Wang L, Hejcek J, Sunden B: PIV measurement of separated flow in a square channel with streamwise periodic ribs on one wall. *Journal of Fluids Engineering-Transactions of the Asme* 2007, 129(7):834-841.
242. Jimenez J: Turbulent flows over rough walls. *Annual Review of Fluid Mechanics* 2004, 36:173-196.
243. Kestin J, Wood RT: Influence of turbulence on mass transfer from cylinders. *Journal of Heat Transfer* 1971, 93(4):321
244. Kataoka K, Kamiyama Y, Hashimoto S, Komai T: Mass-transfer between a plane surface and an impinging turbulent jet – the influence of surface-pressure fluctuations. *Journal of Fluid Mechanics* 1982, 119(JUN):91-105.
245. Simonich JC, Bradshaw P: Effect of free-stream turbulence on heat-transfer through a turbulent boundary-layer. *Journal of Heat Transfer-Transactions of the Asme* 1978, 100(4):671-677.
246. Varun, Saini RP, Singal SK: A review on roughness geometry used in solar air heaters. *Solar Energy* 2007, 81:1340-1350.

247. Roh J-S, Seo S-K, Kim SH, Chi S-H, Kim E-S, Kim HS: Effects of Surface Roughness on the Thermal Emissivity of IG-11 Graphite for Nuclear Reactor. *Korean Journal of Metals and Materials* 2011, 49(7).
248. Bons JP, Taylor RP, McClain ST, Rivir RB: The many faces of turbine surface roughness. *Journal of Turbomachinery-Transactions of the Asme* 2001, 123(4).
249. Mittal MK, Varun, Saini RP, Singal SK: Effective efficiency of solar air heaters having different types of roughness elements on the absorber plate. *Energy* 2007, 32(5).
250. Zeng Y, Lee TS, Yu P, Low HT: Effect of surface roughness on mass transfer in a flat-plate microchannel bioreactor. *Modern Physics Letters B* 2005, 19(28-29).
251. Mobarak AA, Farag HA, Sedahmed GH: Mass transfer in smooth and rough annular ducts under developing flow conditions. *Journal of Applied Electrochemistry* 1997, 27(2).
252. Sanitjai S, Goldstein RJ: Effect of free stream turbulence on local mass transfer from a circular cylinder. *International Journal of Heat and Mass Transfer* 2001, 44(15).
253. Moraveji MK, Sajjadi B, Jafarkhani M, Davarnejad R: Experimental investigation and CFD simulation of turbulence effect on hydrodynamic and mass transfer in a packed bed airlift internal loop reactor. *International Communications in Heat and Mass Transfer* 2011, 38(4):518-524.
254. Huang Y, Zheng H, Mao WW, Li GH, Ye B: Numerical simulation of air-soil two-phase flow based on turbulence modeling. *Natural Hazards* 2011, 58(1):311-323.
255. Ong MC, Utnes T, Holmedal LE, Myrhaug D, Pettersen B: Numerical simulation of flow around a circular cylinder close to a flat seabed at high Reynolds numbers using a k-epsilon model. *Coastal Engineering* 2010, 57(10):931-947.
256. Feigley CE, Do TH, Khan J, Lee E, Schnauffer ND, Salzberg DC: Deriving Realistic Source Boundary Conditions for a CFD Simulation of Concentrations in Workroom Air. *Annals of Occupational Hygiene* 2011, 55(4):410-420.
257. Kumar S, Saini RP: CFD based performance analysis of a solar air heater duct provided with artificial roughness. *Renewable Energy* 2009, 34(5):1285-1291.
258. Prasad BN, Saini JS: Optimal thermohydraulic performance of artificially roughened solar air heaters. *Solar Energy* 1991, 47(2):91-96.

259. Momin AME, Saini JS, Solanki SC: Heat transfer and friction in solar air heater duct with V-shaped rib roughness on absorber plate. *International Journal of Heat and Mass Transfer* 2002, 45(16):3383-3396.
260. Sun R-B, Xi Z-G, Chao F-H, Zhang W, Zhang H-S, Yang D-F: Decomposition of low-concentration gas-phase toluene using plasma-driven photocatalyst reactor. *Atmospheric Environment* 2007, 41(32):6853-6859.
261. Veatch RW, Guerrero ET, Helander DP: Effect of surface roughness on fluid flow through narrow rectangular passages. *Journal of Petroleum Technology* 1965, 17(9).
262. Hans VS, Saini RP, Saini JS: Performance of artificially roughened solar air heaters-A review. *Renewable & Sustainable Energy Reviews* 2009, 13(8).
263. Kukreja LM, Barik S, Misra P: Variable band gap ZnO nanostructures grown by pulsed laser deposition. *Journal of Crystal Growth* 2004, 268(3-4):531-535.
264. Zhang J, Pan CX, Fang PF, Wei JH, Xiong R: Mo plus C Codoped TiO<sub>2</sub> Using Thermal Oxidation for Enhancing Photocatalytic Activity. *Acs Applied Materials & Interfaces* 2010, 2(4):1173-1176.
265. Serpone N, Maruthamuthu P, Pichat P, Pelizzetti E, Hidaka H: Exploiting the interparticle electron-transfer process in the photocatalyzed oxidation of phenol, 2-chlorophenol and pentachlorophenol – chemical evidence for electron and hole transfer between coupled semiconductors. *Journal of Photochemistry and Photobiology a-Chemistry* 1995, 85(3).
266. Fan ZY, Wang DW, Chang PC, Tseng WY, Lu JG: ZnO nanowire field-effect transistor and oxygen sensing property. *Applied Physics Letters* 2004, 85(24):5923-5925.
267. Lyu SC, Zhang Y, Lee CJ, Ruh H, Lee HJ: Low-temperature growth of ZnO nanowire array by a simple physical vapor-deposition method. *Chemistry of Materials* 2003, 15(17):3294-3299.
268. Hsu YF, Xi YY, Tam KH, Djurisic AB, Luo J, Ling CC, Cheung CK, Ng AMC, Chan WK, Deng X *et al*: Undoped p-type ZnO nanorods synthesized by a hydrothermal method. *Advanced Functional Materials* 2008, 18(7):1020-1030.
269. Mu R, Xu Z, Li L, Shao Y, Wan H, Zheng S: On the photocatalytic properties of elongated TiO<sub>2</sub> nanoparticles for phenol degradation and Cr(VI) reduction. *Journal of Hazardous Materials* 2010, 176(1-3):495-502.

270. Kuo T-J, Lin C-N, Kuo C-L, Huang MH: Growth of ultralong ZnO nanowires on silicon substrates by vapor transport and their use as recyclable photocatalysts. *Chemistry of Materials* 2007, 19(21):5143-5147.
271. Wang Y, Li X, Lu G, Quan X, Chen G: Highly oriented 1-D ZnO nanorod arrays on zinc foil: Direct growth from substrate, optical properties and photocatalytic activities. *Journal of Physical Chemistry C* 2008, 112(19):7332-7336.
272. Lin HF, Ravikrishna R, Valsaraj KT: Reusable adsorbents for dilute solution separation. 6. Batch and continuous reactors for the adsorption and degradation of 1,2-dichlorobenzene from dilute wastewater streams using titania as a photocatalyst. *Separation and Purification Technology* 2002, 28(2):87-102.
273. Andreozzi R, Canterino M, Marotta R: Fe(III) homogeneous photocatalysis for the removal of 1,2-dichlorobenzene in aqueous solution by means UV lamp and solar light. *Water Research* 2006, 40(20):3785-3792.
274. Kawaguchi H, Furuya M: Photodegradation of Monochlorobenzene in titanium-dioxide aqueous suspensions. *Chemosphere* 1990, 21(12):1435-1440.
275. Dai K, Chen H, Peng T, Ke D, Yi H: Photocatalytic degradation of methyl orange in aqueous suspension of mesoporous titania nanoparticles. *Chemosphere* 2007, 69(9):1361-1367.
276. He Y, Grieser F, Ashokkumar M: The mechanism of sonophotocatalytic degradation of methyl orange and its products in aqueous solutions. *Ultrasonics Sonochemistry* 2011, 18(5):974-980.

## **APPENDICES**



## Appendix A: List of Symbols

### A.1 Nomenclature

A	area	cm <sup>2</sup>
C	Concentration	mg/ml
e	Roughness height	cm
e/h	Relative height of roughness	
E <sub>g</sub>	Band gap energy	eV
g	Gap of broken rib	cm
g/e	Relative gap of broken rib	
h	Channel height	cm
I	Turbulence intensity	%
k	Reaction rate constant	min <sup>-1</sup>
l	Length of rib roughness	cm
L	Channel length	cm
l/e	Relative length of roughness	
p	Roughness pitch	cm
p/e	Pitch ratio	
Re	Reynolds number	
t	Time	min
V	volume	ml
w	Roughness width	cm
w/e	Relative width of roughness	

## Appendix A (Continued)

W	weight
x	Channel streamwise direction
y	Channel height direction

### A.2 Greek Symbols

$\alpha$	Flow angle of attack	◦
$\beta$	Zenith angle	◦
$\Phi$	Chamfer angle	◦

## Appendix B: Permissions

### B.1 Permission for Article “Enhanced Photocatalytic Activity of Iron Doped Zinc Oxide Nanowires for Water Decontamination” © 2012 Elsevier

#### ELSEVIER LICENSE TERMS AND CONDITIONS

Feb 06, 2013

---

This is a License Agreement between Yangyang Zhang ("You") and Elsevier ("Elsevier") provided by Copyright Clearance Center ("CCC"). The license consists of your order details, the terms and conditions provided by Elsevier, and the payment terms and conditions.

**All payments must be made in full to CCC. For payment instructions, please see information listed at the bottom of this form.**

Supplier	Elsevier Limited The Boulevard, Langford Lane Kidlington, Oxford, OX5 1GB, UK
Registered Company Number	1982084
Customer name	Yangyang Zhang
Customer address	4202 E. Fowler Avenue Tampa, FL 33620
License number	3082670308480
License date	Feb 05, 2013
Licensed content publisher	Elsevier
Licensed content publication	Surface and Coatings Technology
Licensed content title	Enhanced photocatalytic activity of iron doped zinc oxide nanowires for water decontamination
Licensed content author	Yangyang Zhang, Manoj K. Ram, Elias K. Stefanakos, D. Yogi Goswami
Licensed content date	25 February 2013
Licensed content volume number	217
Licensed content issue number	
Number of pages	5
Start Page	119
End Page	123
Type of Use	reuse in a thesis/dissertation
Intended publisher of new work	other
Portion	full article
Format	both print and electronic
Are you the author of this Elsevier article?	Yes
Will you be translating?	No

## Appendix B (Continued)

Order reference number	
Title of your thesis/dissertation	Modeling and Design of Photocatalytic Reactors for Air Purification
Expected completion date	Mar 2013
Estimated size (number of pages)	200
Elsevier VAT number	GB 494 6272 12
Permissions price	0.00 USD
VAT/Local Sales Tax	0.0 USD / 0.0 GBP
Total	0.00 USD
Terms and Conditions	

### INTRODUCTION

1. The publisher for this copyrighted material is Elsevier. By clicking "accept" in connection with completing this licensing transaction, you agree that the following terms and conditions apply to this transaction (along with the Billing and Payment terms and conditions established by Copyright Clearance Center, Inc. ("CCC"), at the time that you opened your Rightslink account and that are available at any time at <http://myaccount.copyright.com>).

### GENERAL TERMS

2. Elsevier hereby grants you permission to reproduce the aforementioned material subject to the terms and conditions indicated.

3. Acknowledgement: If any part of the material to be used (for example, figures) has appeared in our publication with credit or acknowledgement to another source, permission must also be sought from that source. If such permission is not obtained then that material may not be included in your publication/copies. Suitable acknowledgement to the source must be made, either as a footnote or in a reference list at the end of your publication, as follows:

"Reprinted from Publication title, Vol /edition number, Author(s), Title of article / title of chapter, Pages No., Copyright (Year), with permission from Elsevier [OR APPLICABLE SOCIETY COPYRIGHT OWNER]." Also Lancet special credit - "Reprinted from The Lancet, Vol. number, Author(s), Title of article, Pages No., Copyright (Year), with permission from Elsevier."

4. Reproduction of this material is confined to the purpose and/or media for which permission is hereby given.

5. Altering/Modifying Material: Not Permitted. However figures and illustrations may be altered/adapted minimally to serve your work. Any other abbreviations, additions, deletions and/or any other alterations shall be made only with prior written authorization of Elsevier Ltd (Please contact Elsevier at [permissions@elsevier.com](mailto:permissions@elsevier.com))

6. If the permission fee for the requested use of our material is waived in this instance,

## Appendix B (Continued)

please be advised that your future requests for Elsevier materials may attract a fee.

7. **Reservation of Rights:** Publisher reserves all rights not specifically granted in the combination of (i) the license details provided by you and accepted in the course of this licensing transaction, (ii) these terms and conditions and (iii) CCC's Billing and Payment terms and conditions.

8. **License Contingent Upon Payment:** While you may exercise the rights licensed immediately upon issuance of the license at the end of the licensing process for the transaction, provided that you have disclosed complete and accurate details of your proposed use, no license is finally effective unless and until full payment is received from you (either by publisher or by CCC) as provided in CCC's Billing and Payment terms and conditions. If full payment is not received on a timely basis, then any license preliminarily granted shall be deemed automatically revoked and shall be void as if never granted. Further, in the event that you breach any of these terms and conditions or any of CCC's Billing and Payment terms and conditions, the license is automatically revoked and shall be void as if never granted. Use of materials as described in a revoked license, as well as any use of the materials beyond the scope of an unrevoked license, may constitute copyright infringement and publisher reserves the right to take any and all action to protect its copyright in the materials.

9. **Warranties:** Publisher makes no representations or warranties with respect to the licensed material.

10. **Indemnity:** You hereby indemnify and agree to hold harmless publisher and CCC, and their respective officers, directors, employees and agents, from and against any and all claims arising out of your use of the licensed material other than as specifically authorized pursuant to this license.

11. **No Transfer of License:** This license is personal to you and may not be sublicensed, assigned, or transferred by you to any other person without publisher's written permission.

12. **No Amendment Except in Writing:** This license may not be amended except in a writing signed by both parties (or, in the case of publisher, by CCC on publisher's behalf).

13. **Objection to Contrary Terms:** Publisher hereby objects to any terms contained in any purchase order, acknowledgment, check endorsement or other writing prepared by you, which terms are inconsistent with these terms and conditions or CCC's Billing and Payment terms and conditions. These terms and conditions, together with CCC's Billing and Payment terms and conditions (which are incorporated herein), comprise the entire agreement between you and publisher (and CCC) concerning this licensing transaction. In the event of any conflict between your obligations established by these terms and conditions and those established by CCC's Billing and Payment terms and conditions, these terms and conditions shall control.

14. **Revocation:** Elsevier or Copyright Clearance Center may deny the permissions described in this License at their sole discretion, for any reason or no reason, with a full refund payable to you. Notice of such denial will be made using the contact information provided by you. Failure to receive such notice will not alter or invalidate the denial. In no event will Elsevier or Copyright Clearance Center be responsible or liable for any costs, expenses or damage

## Appendix B (Continued)

incurred by you as a result of a denial of your permission request, other than a refund of the amount(s) paid by you to Elsevier and/or Copyright Clearance Center for denied permissions.

### LIMITED LICENSE

The following terms and conditions apply only to specific license types:

**15. Translation:** This permission is granted for non-exclusive world **English** rights only unless your license was granted for translation rights. If you licensed translation rights you may only translate this content into the languages you requested. A professional translator must perform all translations and reproduce the content word for word preserving the integrity of the article. If this license is to re-use 1 or 2 figures then permission is granted for non-exclusive world rights in all languages.

**16. Website:** The following terms and conditions apply to electronic reserve and author websites:

**Electronic reserve:** If licensed material is to be posted to website, the web site is to be password-protected and made available only to bona fide students registered on a relevant course if:

This license was made in connection with a course,

This permission is granted for 1 year only. You may obtain a license for future website posting,

All content posted to the web site must maintain the copyright information line on the bottom of each image,

A hyper-text must be included to the Homepage of the journal from which you are licensing at <http://www.sciencedirect.com/science/journal/xxxxx> or the Elsevier homepage for books at <http://www.elsevier.com>, and

**Central Storage:** This license does not include permission for a scanned version of the material to be stored in a central repository such as that provided by Heron/XanE du.

**17. Author website** for journals with the following additional clauses:

All content posted to the web site must maintain the copyright information line on the bottom of each image, and the permission granted is limited to the personal version of your paper. You are not allowed to download and post the published electronic version of your article (whether PDF or HTML, proof or final version), nor may you scan the printed edition to create an electronic version. A hyper-text must be included to the Homepage of the journal from which you are licensing at

<http://www.sciencedirect.com/science/journal/xxxxx>. As part of our normal production process, you will receive an e-mail notice when your article appears on Elsevier's online service ScienceDirect ([www.sciencedirect.com](http://www.sciencedirect.com)). That e-mail will include the article's Digital Object Identifier (DOI). This number provides the electronic link to the published article and should be included in the posting of your personal version. We ask that you wait until you receive this e-mail and have the DOI to do any posting.

**Central Storage:** This license does not include permission for a scanned version of the material to be stored in a central repository such as that provided by Heron/XanE du.

**18. Author website** for books with the following additional clauses:

## Appendix B (Continued)

Authors are permitted to place a brief summary of their work online only.

A hyper-text must be included to the Elsevier homepage at <http://www.elsevier.com>. All content posted to the web site must maintain the copyright information line on the bottom of each image. You are not allowed to download and post the published electronic version of your chapter, nor may you scan the printed edition to create an electronic version.

Central Storage: This license does not include permission for a scanned version of the material to be stored in a central repository such as that provided by Heron/XanE du

19. **Website** (regular and for author): A hyper-text must be included to the Homepage of the journal from which you are licensing at <http://www.sciencedirect.com/science/journal/xxxxx>. or for books to the Elsevier homepage at <http://www.elsevier.com>

20. **Thesis/Dissertation**: If your license is for use in a thesis/dissertation your thesis may be submitted to your institution in either print or electronic form. Should your thesis be published commercially, please reapply for permission. These requirements include permission for the Library and Archives of Canada to supply single copies, on demand, of the complete thesis and include permission for UMI to supply single copies, on demand, of the complete thesis. Should your thesis be published commercially, please reapply for permission.

21. **Other Conditions**:

v1.6

If you would like to pay for this license now, please remit this license along with your payment made payable to "COPYRIGHT CLEARANCE CENTER" otherwise you will be invoiced within 48 hours of the license date. Payment should be in the form of a check or money order referencing your account number and this invoice number RLNK500950585.

Once you receive your invoice for this order, you may pay your invoice by credit card. Please follow instructions provided at that time.

**Make Payment To:**  
Copyright Clearance Center  
Dept 001  
P.O. Box 843006  
Boston, MA 02284-3006

For suggestions or comments regarding this order, contact RightsLink Customer Support: [customer care@copyright.com](mailto:customer care@copyright.com) or +1-877-622-5543 (toll free in the US) or +1-978-646-2777.

Gratis licenses (referencing \$0 in the Total field) are free. Please retain this printable license for your reference. No payment is required.

## Appendix B (Continued)

### B.2 Permission for Article “Effect of Photocatalytic Surface Roughness on Reactors Effectiveness for Indoor Air Cleaning” © 2013 Elsevier

#### ELSEVIER LICENSE TERMS AND CONDITIONS

Feb 06, 2013

---

This is a License Agreement between Yangyang Zhang ("You") and Elsevier ("Elsevier") provided by Copyright Clearance Center ("CCC"). The license consists of your order details, the terms and conditions provided by Elsevier, and the payment terms and conditions.

**All payments must be made in full to CCC. For payment instructions, please see information listed at the bottom of this form.**

Supplier	Elsevier Limited The Boulevard, Langford Lane Kidlington, Oxford, OX5 1GB, UK
Registered Company Number	1982084
Customer name	Yangyang Zhang
Customer address	4202 E. Fowler Avenue Tampa, FL 33620
License number	3082220067318
License date	Feb 04, 2013
Licensed content publisher	Elsevier
Licensed content publication	Building and Environment
Licensed content title	Effect of photocatalytic surface roughness on reactors effectiveness for indoor air cleaning
Licensed content author	Yangyang Zhang, Elias K. Stefanakos, D. Yogi Goswami
Licensed content date	March 2013
Licensed content volume number	61
Licensed content issue number	
Number of pages	9
Start Page	188
End Page	196
Type of Use	reuse in a thesis/dissertation
Intended publisher of new work	other
Portion	full article
Format	both print and electronic
Are you the author of this Elsevier article?	Yes
Will you be translating?	No



## Appendix B (Continued)

Order reference number	
Title of your thesis/dissertation	Modeling and Design of Photocatalytic Reactors for Air Purification
Expected completion date	Mar 2013
Estimated size (number of pages)	200
Elsevier VAT number	GB 494 6272 12
Permissions price	0.00 USD
VAT/Local Sales Tax	0.0 USD / 0.0 GBP
Total	0.00 USD
Terms and Conditions	

### INTRODUCTION

1. The publisher for this copyrighted material is Elsevier. By clicking "accept" in connection with completing this licensing transaction, you agree that the following terms and conditions apply to this transaction (along with the Billing and Payment terms and conditions established by Copyright Clearance Center, Inc. ("CCC"), at the time that you opened your Rightslink account and that are available at any time at <http://myaccount.copyright.com>).

### GENERAL TERMS

2. Elsevier hereby grants you permission to reproduce the aforementioned material subject to the terms and conditions indicated.

3. Acknowledgement: If any part of the material to be used (for example, figures) has appeared in our publication with credit or acknowledgement to another source, permission must also be sought from that source. If such permission is not obtained then that material may not be included in your publication/copies. Suitable acknowledgement to the source must be made, either as a footnote or in a reference list at the end of your publication, as follows:

"Reprinted from Publication title, Vol /edition number, Author(s), Title of article / title of chapter, Pages No., Copyright (Year), with permission from Elsevier [OR APPLICABLE SOCIETY COPYRIGHT OWNER]." Also Lancet special credit - "Reprinted from The Lancet, Vol. number, Author(s), Title of article, Pages No., Copyright (Year), with permission from Elsevier."

4. Reproduction of this material is confined to the purpose and/or media for which permission is hereby given.

5. Altering/Modifying Material: Not Permitted. However figures and illustrations may be altered/adapted minimally to serve your work. Any other abbreviations, additions, deletions and/or any other alterations shall be made only with prior written authorization of Elsevier Ltd. (Please contact Elsevier at [permissions@elsevier.com](mailto:permissions@elsevier.com))

6. If the permission fee for the requested use of our material is waived in this instance,

## Appendix B (Continued)

please be advised that your future requests for Elsevier materials may attract a fee.

7. **Reservation of Rights:** Publisher reserves all rights not specifically granted in the combination of (i) the license details provided by you and accepted in the course of this licensing transaction, (ii) these terms and conditions and (iii) CCC's Billing and Payment terms and conditions.

8. **License Contingent Upon Payment:** While you may exercise the rights licensed immediately upon issuance of the license at the end of the licensing process for the transaction, provided that you have disclosed complete and accurate details of your proposed use, no license is finally effective unless and until full payment is received from you (either by publisher or by CCC) as provided in CCC's Billing and Payment terms and conditions. If full payment is not received on a timely basis, then any license preliminarily granted shall be deemed automatically revoked and shall be void as if never granted. Further, in the event that you breach any of these terms and conditions or any of CCC's Billing and Payment terms and conditions, the license is automatically revoked and shall be void as if never granted. Use of materials as described in a revoked license, as well as any use of the materials beyond the scope of an unrevoked license, may constitute copyright infringement and publisher reserves the right to take any and all action to protect its copyright in the materials.

9. **Warranties:** Publisher makes no representations or warranties with respect to the licensed material.

10. **Indemnity:** You hereby indemnify and agree to hold harmless publisher and CCC, and their respective officers, directors, employees and agents, from and against any and all claims arising out of your use of the licensed material other than as specifically authorized pursuant to this license.

11. **No Transfer of License:** This license is personal to you and may not be sublicensed, assigned, or transferred by you to any other person without publisher's written permission.

12. **No Amendment Except in Writing:** This license may not be amended except in a writing signed by both parties (or, in the case of publisher, by CCC on publisher's behalf).

13. **Objection to Contrary Terms:** Publisher hereby objects to any terms contained in any purchase order, acknowledgment, check endorsement or other writing prepared by you, which terms are inconsistent with these terms and conditions or CCC's Billing and Payment terms and conditions. These terms and conditions, together with CCC's Billing and Payment terms and conditions (which are incorporated herein), comprise the entire agreement between you and publisher (and CCC) concerning this licensing transaction. In the event of any conflict between your obligations established by these terms and conditions and those established by CCC's Billing and Payment terms and conditions, these terms and conditions shall control.

14. **Revocation:** Elsevier or Copyright Clearance Center may deny the permissions described in this License at their sole discretion, for any reason or no reason, with a full refund payable to you. Notice of such denial will be made using the contact information provided by you. Failure to receive such notice will not alter or invalidate the denial. In no event will Elsevier or Copyright Clearance Center be responsible or liable for any costs, expenses or damage

## Appendix B (Continued)

incurred by you as a result of a denial of your permission request, other than a refund of the amount(s) paid by you to Elsevier and/or Copyright Clearance Center for denied permissions.

### LIMITED LICENSE

The following terms and conditions apply only to specific license types:

**15. Translation:** This permission is granted for non-exclusive world **English** rights only unless your license was granted for translation rights. If you licensed translation rights you may only translate this content into the languages you requested. A professional translator must perform all translations and reproduce the content word for word preserving the integrity of the article. If this license is to re-use 1 or 2 figures then permission is granted for non-exclusive world rights in all languages.

**16. Website:** The following terms and conditions apply to electronic reserve and author websites:

**Electronic reserve:** If licensed material is to be posted to website, the web site is to be password-protected and made available only to bona fide students registered on a relevant course if:

This license was made in connection with a course,

This permission is granted for 1 year only. You may obtain a license for future website posting,

All content posted to the web site must maintain the copyright information line on the bottom of each image,

A hyper-text must be included to the Homepage of the journal from which you are licensing at <http://www.sciencedirect.com/science/journal/xxxxx> or the Elsevier homepage for books at <http://www.elsevier.com>, and

Central Storage: This license does not include permission for a scanned version of the material to be stored in a central repository such as that provided by Heron/XanE du

**17. Author website** for journals with the following additional clauses:

All content posted to the web site must maintain the copyright information line on the bottom of each image, and the permission granted is limited to the personal version of your paper. You are not allowed to download and post the published electronic version of your article (whether PDF or HTML, proof or final version), nor may you scan the printed edition to create an electronic version. A hyper-text must be included to the Homepage of the journal from which you are licensing at

<http://www.sciencedirect.com/science/journal/xxxxx>. As part of our normal production process, you will receive an e-mail notice when your article appears on Elsevier's online service ScienceDirect ([www.sciencedirect.com](http://www.sciencedirect.com)). That e-mail will include the article's Digital Object Identifier (DOI). This number provides the electronic link to the published article and should be included in the posting of your personal version. We ask that you wait until you receive this e-mail and have the DOI to do any posting.

Central Storage: This license does not include permission for a scanned version of the material to be stored in a central repository such as that provided by Heron/XanE du

**18. Author website** for books with the following additional clauses:

## Appendix B (Continued)

Authors are permitted to place a brief summary of their work online only.

A hyper-text must be included to the Elsevier homepage at <http://www.elsevier.com>. All content posted to the web site must maintain the copyright information line on the bottom of each image. You are not allowed to download and post the published electronic version of your chapter, nor may you scan the printed edition to create an electronic version.

**Central Storage:** This license does not include permission for a scanned version of the material to be stored in a central repository such as that provided by Heron/XanEdu.

**19. Website (regular and for author):** A hyper-text must be included to the Homepage of the journal from which you are licensing at <http://www.sciencedirect.com/science/journal/xxxxx>. or for books to the Elsevier homepage at <http://www.elsevier.com>

**20. Thesis/Dissertation:** If your license is for use in a thesis/dissertation your thesis may be submitted to your institution in either print or electronic form. Should your thesis be published commercially, please reapply for permission. These requirements include permission for the Library and Archives of Canada to supply single copies, on demand, of the complete thesis and include permission for UMI to supply single copies, on demand, of the complete thesis. Should your thesis be published commercially, please reapply for permission.

**21. Other Conditions:**

v1.6

If you would like to pay for this license now, please remit this license along with your payment made payable to "COPYRIGHT CLEARANCE CENTER" otherwise you will be invoiced within 48 hours of the license date. Payment should be in the form of a check or money order referencing your account number and this invoice number RLNK500949780.

Once you receive your invoice for this order, you may pay your invoice by credit card. Please follow instructions provided at that time.

**Make Payment To:**  
Copyright Clearance Center  
Dept 001  
P.O. Box 843006  
Boston, MA 02284-3006

For suggestions or comments regarding this order, contact RightsLink Customer Support: [customercare@copyright.com](mailto:customercare@copyright.com) or +1-877-622-5543 (toll free in the US) or +1-978-646-2777.

Gratis licenses (referencing \$0 in the Total field) are free. Please retain this printable license for your reference. No payment is required.

## Appendix B (Continued)

### B.3 Permission for Article “Synthesis, Characterization, and Applications of ZnO Nanowires” © 2012 Hindawi Publishing Corporation

Journal of Nanomaterials  
Volume 2012 (2012), Article ID 624520, 22 pages  
doi:10.1155/2012/624520

#### Review Article

### Synthesis, Characterization, and Applications of ZnO Nanowires








Yangyang Zhang, Manoj K. Ram, Elias K. Stefanakos, and D. Yogi Goswami

Clean Energy Research Center, College of Engineering, University of South Florida, Tampa, FL 33620, USA

Received 13 January 2012; Accepted 18 April 2012

Academic Editor: Tong Lin

Copyright © 2012 Yangyang Zhang et al. This is an open access article distributed under the Creative Commons Attribution License, which permits unrestricted use, distribution, and reproduction in any medium, provided the original work is properly cited.

-  Abstract
-  Full-Text PDF
-  Full-Text HTML
-  Full-Text ePUB
-  Linked References
-  How to Cite this Article
-  Complete Special Issue

#### Abstract

ZnO nanowires (or nanorods) have been widely studied due to their unique material properties and remarkable performance in electronics, optics, and photonics. Recently, photocatalytic applications of ZnO nanowires are of increased interest in environmental protection applications. This paper presents a review of the current research of ZnO nanowires (or nanorods) with special focus on photocatalysis. We have reviewed the semiconducting photocatalysts and discussed a variety of synthesis methods of ZnO nanowires and their corresponding effectiveness in photocatalysis. We have also presented the characterization of ZnO nanowires from the literature and from our own measurements. Finally, a wide range of uses of ZnO nanowires in various applications is highlighted in this paper.

## **ABOUT THE AUTHOR**

Yangyang Zhang was born in Huian, Fujian province, China P.R. After completing his Bachelor of Applied Chemistry at HuaQiao University in 2001, he worked for the Third Institute of Oceanography, State Oceanic Administration. His work there focused on natural product purification.

In 2006, he came to the United States in search of a better career. In August 2009, he entered the Graduate School of the University of South Florida to conduct his Ph.D. study. During his Ph.D. study, he worked on the development of photocatalysts and photocatalytic reactor design under the guidance of Drs. Yogi Goswami and Elias Stefanakos in the Clean Energy Research Center (CERC). He expects to graduate in 2013 with a Doctor of Philosophy in Chemical Engineering from the University of South Florida, with a dissertation entitled “Modeling and Design of Photocatalytic Reactors for Air Purification”.